Electron-Electron Interactions in Graphene: Current Status and Perspectives

Valeri N. Kotov,[1] Bruno Uchoa,[2] Vitor M. Pereira,[3]
F. Guinea,[4] and A. H. Castro Neto[5,3]

[1]*Department of Physics, University of Vermont, 82 University Place, Burlington, Vermont 05405*
[2]*Department of Physics, University of Illinois at Urbana-Champaign, 1110 West Green Street, Urbana, Illinois 61801*
[3]*Graphene Research Centre and Department of Physics, National University of Singapore, 2 Science Drive 3, Singapore 117542*
[4]*Instituto de Ciencia de Materiales de Madrid, Sor Juana Inés de la Cruz 3, E-28049 Madrid, Spain*
[5]*Department of Physics, Boston University, 590 Commonwealth Avenue, Boston, Massachusetts 02215*

(published 19 July 2012)

The problem of electron-electron interactions in graphene is reviewed. Starting from the screening of long-range interactions in these systems, the existence of an emerging Dirac liquid of Lorentz invariant quasiparticles in the weak-coupling regime is discussed, as well as the formation of strongly correlated electronic states in the strong-coupling regime. The analogy and connections between the many-body problem and the Coulomb impurity problem are also analyzed. The problem of the magnetic instability and Kondo effect of impurities and/or adatoms in graphene is also discussed in analogy with classical models of many-body effects in ordinary metals. Lorentz invariance is shown to play a fundamental role and leads to effects that span the whole spectrum, from the ultraviolet to the infrared. The effect of an emerging Lorentz invariance is also discussed in the context of finite size and edge effects as well as mesoscopic physics. The effects of strong magnetic fields in single layers and some of the main aspects of the many-body problem in graphene bilayers are briefly reviewed. In addition to reviewing the fully understood aspects of the many-body problem in graphene, a plethora of interesting issues are shown to remain open, both theoretically and experimentally, and the field of graphene research is still exciting and vibrant.

DOI: 10.1103/RevModPhys.84.1067 PACS numbers: 81.05.ue, 71.10.−w, 73.22.Pr

CONTENTS

I. INTRODUCTION

One of the most important problems in theoretical physics is the understanding of the properties of quantum systems with an infinitely large number of interacting degrees of freedom, the so-called many-body problem. Interactions are present in almost all areas of physics: soft and hard condensed matter, field theory, atomic physics, quantum chemistry, nuclear physics, astrophysics, etc. Interactions between particles are responsible for a plethora of effects and many-body states, from the band structure of crystals to superconductivity in metals, from the quark-gluon plasma in heavy ion collisions to asymptotic freedom in quantum chromodynamics. It is the competition between the kinetic energy of particles, that is, their inertia, and interactions among them that leads to the richness and complexity of these different phases. For these reasons, many-body interactions are very specific and the hardest to describe theoretically.

One of the greatest theoretical achievements of the last century, the Landau theory of the Fermi liquid (Baym and Pethick, 1991), asserts something simple but, at the same time, deep: that the excitations of a large (indeed, infinite) collection of strongly interacting particles can be described as an equally large collection of weakly interacting quasiparticles that carry the same quantum numbers as the original particles. This statement is far from trivial. Consider, for instance, the behavior of electrons in a metal. The electrons interact among themselves and with ions in the crystal via strong long-range Coulomb interactions. It is not at all clear what the outcome of this complex interacting problem is. Without having any deep theoretical resources to treat this problem, except intuition, visionaries like Paul Drude (Drude, 1900a; Drude, 1900b) and Arnold Sommerfeld (Hoddeson, Baym, and Eckert, 1987) settled the foundations for the understanding of this complex problem by postulating that (1) electrons propagate freely in a nonrelativistic (Galilean invariant) way (Drude's contribution), and (2) electrons obey Fermi-Dirac statistics (Sommerfeld's contribution). *Galilean invariance* dictates that the electrons have a kinetic energy given by

$$K_0 = \frac{\mathbf{p}^2}{2m^*}, \tag{1.1}$$

where $\mathbf{p}$ is the electron momentum and m^* is a free parameter of the theory called the effective mass. Fermi-Dirac statistics implies that electrons carry spin $1/2$ and that, in the ground state, all states with energy below the so-called Fermi energy E_F are occupied, and all the states above it are empty. With these two basic assumptions and simple considerations about electron scattering by defects, the Drude-Sommerfeld model was capable of describing experimental data of several generations of scientists.

The understanding of why these two assumptions are valid for a strongly interacting problem, such as electrons in a metal, had to wait for the development of two major concepts: (i) the *band structure* theory that explains that the interaction of the electrons with a periodic lattice of ions produces states that, as the plane waves described by (1.1), are extended over the entire lattice (Bloch, 1929); and (ii) the theory of *screening*, that is, that metals are dynamically polarizable materials and that electrons act collectively to screen electric fields in their interior (Lindhard, 1954). Hence, long-range Coulomb interactions become effectively short ranged and weak enough to give substance to Drude's assumptions. In this case, the effective mass m^* reflects the change in the inertia of the electron as it moves around in an effective medium. Nevertheless, there are situations when these assumptions fail even in crystalline systems, and that is when interesting things happen, namely, the free electron picture breaks down.

In fact, there are many instances where the Fermi-liquid ground state becomes unstable. Electrons not only interact with static ions but also with their vibrations, the phonons. Electron-phonon interactions, in the presence of strong screening, can lead to an effective attractive interaction between electrons producing a catastrophic Fermi surface instability towards a superconducting ground state (Tinkham, 1996). Fermi surface instabilities also happen in special situations in the presence of Fermi surface nesting, which can lead to charge and spin density wave ground states (Gruner, 1994). Crystals with inner shell electrons, such as transition metals, can also have many-body instabilities due to the strong *local* interactions between the electrons, leading to insulating states with magnetic properties as in the case of Mott insulators (Mott, 1949). Another important case of Fermi-liquid breakdown is when the electron density is very low and the screening disappears.

Notice that in quantum mechanics the momentum of the particle relates to its wavelength λ by $p = \hbar/\lambda$ and hence the kinetic energy (1.1) behaves as $K = \hbar^2/(2m^*\lambda^2)$. If the average distance between electrons is ℓ, we see that the average kinetic energy per electron has to be of the order $E_K \approx \hbar^2 n_d^{2/d}(2m^*)$, where $n_d = 1/\ell^d$ is the average electron density in d spatial dimensions. On the other hand, the Coulomb interaction is given by

$$V(r) = \frac{e^2}{\epsilon_0 r}, \tag{1.2}$$

where e is the electron charge and ϵ_0 the dielectric constant of the medium. Notice that the Coulomb energy per electron is of the order $E_C \approx e^2 n_d^{1/d}/\epsilon_0$. Thus, the ratio of Coulomb to kinetic energy is given by $r_s = E_C/E_K \propto (n_0/n_d)^{1/d}$, where $n_0 = (m^* e^2/\hbar^2\epsilon_0)^d$ depends only on material properties. Therefore, at high electron densities $n_d \gg n_0$ the kinetic energy dominates over the Coulomb energy, which can be disregarded, and the Fermi-liquid description is safe. At low densities $n_d \ll n_0$ the Coulomb energy is dominant and new electronic phases, such as ferromagnetism and Wigner crystallization, can become stable (Ceperley, 1978). Therefore, the relative strength of the kinetic to Coulomb interactions in Galilean invariant systems is completely controlled by the

electron density. Note that in all of the cases discussed above, the Galilean invariance was kept intact and the driving force for the many-body instabilities was the enhancement of the Coulomb relative to the kinetic energy.

With the advent of graphene (Novoselov *et al.*, 2004), a two-dimensional crystal of pure carbon, this picture has changed and a new example of Fermi-liquid breakdown has emerged in a big way. In graphene, due to its peculiar lattice structure, the electrons at the Fermi energy are described in terms of an effective *Lorentz* invariant theory where the kinetic energy is given by the Dirac dispersion (Castro Neto *et al.*, 2009a)

$$K_G = \pm v_F |\mathbf{p}|, \tag{1.3}$$

where v_F is the Fermi-Dirac velocity, and the $\pm$ signs refer to two linearly dispersing bands. If we take Eq. (1.3) at face value and reconsider the argument given above on the relevance of the Coulomb interactions, we reach very different conclusions. First, the form of the Coulomb interaction remains the same as in Eq. (1.2), since v_F is a material's property and hence much smaller than the speed of light c. This means that the photons which mediate the Coulomb interaction are still much faster than the electrons and, thus, the electron-electron interaction can be considered as instantaneous. Therefore, the Coulomb interaction (1.2) actually breaks the Lorentz invariance of Eq. (1.3). Second, because of the linear scaling of the kinetic energy with momentum, we see that the average kinetic energy per electron has to scale as $E_G \approx \hbar v_F n^{1/2}$ and consequently the ratio of Coulomb to kinetic energy is given by

$$\alpha = \frac{E_C}{E_G} = \frac{e^2}{\epsilon_0 \hbar v_F}, \tag{1.4}$$

and is *independent* of the electronic density n, depending only on material properties and environmental conditions, such as ϵ_0. Here, and from now on, we refer to graphene's electron density as n. As the electronic properties of graphene are sensitive to environmental conditions, they will be modified by the presence of other layers. In fact, as we are going to show, bilayer graphene has properties which are rather different than its monolayer counterpart. Furthermore, due to the same peculiar dispersion relation, the electronic density of states $\rho(E)$ vanishes at the Dirac point $\rho(E) \propto |E|/v_F^2$, and hence graphene is a hybrid between an insulator and a metal: neutral graphene is not a metal because it has vanishing density of states at the Fermi energy, and it is not an insulator because it does not have a gap in the spectrum. This means that pristine (or lightly doped) graphene cannot screen the long-range Coulomb interaction in the usual (metallic) way, although it is possible to produce electronic excitations at vanishingly small energy. This state of affairs makes graphene a unique system from the point of view of electron-electron interactions. The long-range interactions lead to nontrivial renormalization of the Dirac quasiparticle characteristics near the charge neutrality point, and the resulting electronic state can be called *Dirac liquid*, to be distinguished from the Fermi-liquid behavior at finite chemical potential (away from the Dirac point, where conventional screening takes place.)

The unusual relation between kinetic and Coulomb energies not only affects the electron-electron interactions, but also the interactions of electrons with charged impurities, the so-called Coulomb impurity problem. In a metal described by a Galilean invariant theory of the form (1.1), screening also makes the interaction with the impurity short ranged, and hence the scattering problem effectively reduces to the one of a short-range impurity. In graphene, because of the lack of screening, the situation is rather different, and one has to face the problem effecting the long-range part of the potential. Scattering by long-range interactions has a long history in physics and it leads to the issue of logarithmic phase shifts (Baym, 1969). In graphene, because of its emergent Lorentz invariance, this issue is magnified. Since Coulomb interactions between electrons and electron scattering by Coulomb impurities are closely related issues, one expects that many of the anomalies of one problem are also reflected in the other.

Another interesting consequence of the scaling of the kinetic energy with momentum is related to the issue of electron confinement. If electrons are confined to a region of size L, the energy of the states is quantized, no matter whether the electrons obey Galilean or Lorentz invariance. However, the quantization of energy is rather different in these two cases. In a Galilean invariant system, such as the one described by Eq. (1.1), the energy levels are spaced as $\Delta E_0 \propto 1/L^2$ while in graphene Lorentz invariance, Eq. (1.3), implies $\Delta E_G \propto 1/L$. Hence, the size dependence of the energy levels in sufficiently small samples of graphene is rather different than one would find in normal metals. Moreover, since the Coulomb energy scales as $1/L$, we expect Coulomb effects to be stronger in nanoscopic and mesoscopic graphene samples.

Furthermore, the fact that graphene is a two-dimensional (2D) system has strong consequences for electronic motion in the presence of perpendicular magnetic fields. Since a perpendicular magnetic field B leads to a quantization of the energy in terms of Landau levels, and the electrons cannot propagate along the direction of the field, its effect is singular, in the sense that the problem has a massive degeneracy. So, strong magnetic fields can completely quench the kinetic energy of the electrons that become dispersionless. The electronic orbits are localized in a region of the size of the magnetic length: $\ell_B = \sqrt{\hbar c/eB}$. For a Galilean invariant system, such as the one described by Eq. (1.1), for $p \approx \hbar/\ell_B$ the kinetic energy per electron is of order $K \approx \hbar\omega_C \propto B$, where $\omega_C = \hbar/m^*\ell_B^2$ is the cyclotron frequency. On the other hand, for graphene, using Eq. (1.3), one has $E_G \approx \hbar\omega_G \propto \sqrt{B}$, where $\omega_G = \sqrt{2}v_F/\ell_B$, which is a consequence of the Lorentz invariance. Note that in both cases the Coulomb energy per electron scales as $E_C \propto e^2/\epsilon_0\ell_B \propto \sqrt{B}$. Hence, in a Galilean invariant system the Coulomb energy is smaller than the kinetic energy at high fields while for Lorentz invariant systems they are always comparable. Thus, one expects Coulomb interactions to be largely enhanced in the presence of these magnetic fields. In the 2D electron gas (2DEG) this unusual state of affairs is what leads to the fractional quantum Hall effect (FQHE) (Laughlin, 1983).

Given all of these unusual circumstances, many questions come to mind: How does screening of the long-range

Coulomb interaction work in graphene? Can graphene be described in terms a Lorentz invariant theory of quasiparticles? Is the Coulomb impurity problem in graphene the same as in a normal metal? In what circumstances is graphene unstable towards many-body ground states? Are there quantum phase transitions (Sachdev, 1999) in the phase diagram of graphene? Do magnetic moments form in graphene in the same way as they do in normal metals? What is the ground state of graphene in high magnetic fields?

The objective of this review is not to cover the basic aspects of graphene physics, since this was already covered in a recent review (Castro Neto *et al.*, 2009a), but to try to address some of these questions while keeping others open. The field of many-body physics will always be an open field because a seemingly simple question always leads to another question even more profound and harder to answer in a definitive way. In many ways, what we have done here is to only scratch the surface of this rich and important field, and leave open a large number of interesting and unexplored problems.

II. CHARGE POLARIZATION AND LINEAR SCREENING

A. Tight-binding spectrum

In isolated form, carbon has six electrons in the orbital configuration $1s^2 2s^2 2p^2$. When arranged in the honeycomb crystal shown in Fig. 1(a), two electrons remain in the core $1s$ orbital, while the other orbitals hybridize, forming three sp^2 bonds and one p_z orbital. The sp^2 orbitals form the σ band, which contains three localized electrons. The bonding configuration among the p_z orbitals of different lattice sites generates a valence band, or π band, containing one electron,

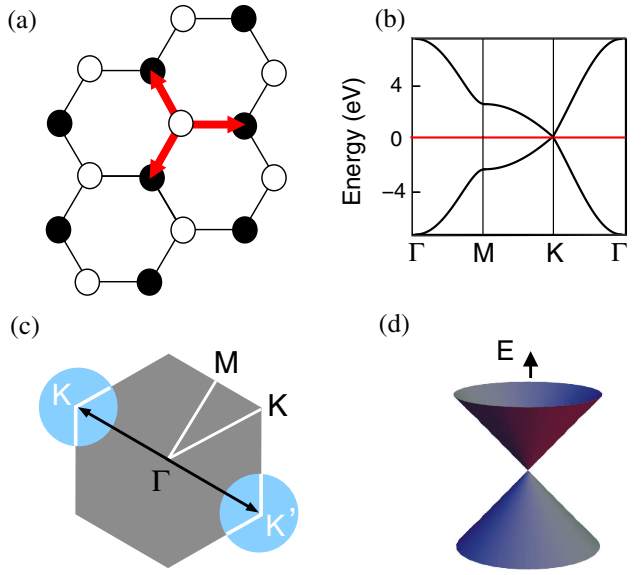

FIG. 1 (color online). (a) Honeycomb lattice with the two sublattices in graphene. The arrows are nearest neighbor vectors. (b) Tight-binding spectrum for the $\pi - \pi^*$ bands. The horizontal line intersecting the K point corresponds to the Fermi level at half-filling. (c) Brillouin zone centered around the Γ point. (d) Dirac cone resulting from the linearization of the tight-binding spectrum around the K points (circles).

whereas the antibonding configuration generates the conduction band (π^*), which is empty.

From a kinetic energy point of view, the electronic single-particle dispersion in graphene is essentially defined by the hopping of the electrons between nearest neighbor carbon sites in the honeycomb lattice. Unlike square or triangular lattices, the honeycomb lattice is spanned by two different sets of Bravais lattice generators, forming a two component basis with one set for each triangular sublattice. Defining a label for electrons sitting in each of the two sublattices, say A and B, the free hopping Hamiltonian of graphene is

$$\mathcal{H}_0 = -t \sum_{\sigma,\langle ij\rangle} [a^\dagger_\sigma(\mathbf{R}_i) b_\sigma(\mathbf{R}_j)] + \text{H.c.} - \mu \sum_{\sigma,i} \hat{n}_\sigma(\mathbf{R}_i), \tag{2.1}$$

where $a_\sigma(\mathbf{R}_i)$ and $b_\sigma(\mathbf{R}_i)$ are fermionic operators for sublattices A and B, respectively, $\hat{n}_\sigma(\mathbf{R}_i)$ is the number operator, $\sigma = \uparrow, \downarrow$ labels the spin, and $\langle ij\rangle$ means summation over nearest neighbors. The two energy scales in the Hamiltonian are $t \approx 2.8$ eV, which is the hopping energy between nearest carbon atoms, and μ, the chemical potential away from half-filling [see Fig. 1(b)]. In a homogeneous system, deviations from half-filling ($\mu = 0$) are routinely induced by charge transfer from a substrate (Giovannetti *et al.*, 2008), by application of a back gate voltage (Novoselov *et al.*, 2004; Novoselov, Jiang *et al.*, 2005; Novoselov, Geim *et al.*, 2005), or else by chemical doping (Calandra and Mauri, 2007; Uchoa, Lin, and Castro Neto, 2008; Grüneis *et al.*, 2009; McChesney *et al.*, 2010).

In momentum space the free Hamiltonian of graphene is

$$\mathcal{H}_0 = \sum_{\mathbf{p},\sigma} \Psi^\dagger_{\mathbf{p},\sigma} \begin{pmatrix} -\mu & -t\phi_{\mathbf{p}} \\ -t\phi^*_{\mathbf{p}} & -\mu \end{pmatrix} \Psi_{\mathbf{p},\sigma}, \tag{2.2}$$

where $\Psi_{\mathbf{p},\sigma} = (a_{\mathbf{p},\sigma}, b_{\mathbf{p},\sigma})$ is a two component spinor and

$$\phi_{\mathbf{p}} = \sum_{i=1}^{3} e^{i\mathbf{p}\cdot\mathbf{a}_i} \tag{2.3}$$

is a tight-binding function summed over the nearest neighbor vectors

$$\mathbf{a}_1 = a\hat{\mathbf{x}}, \qquad \mathbf{a}_2 = -\frac{a}{2}\hat{\mathbf{x}} + a\frac{\sqrt{3}}{2}\hat{\mathbf{y}}, \qquad \mathbf{a}_3 = -\frac{a}{2}\hat{\mathbf{x}} - a\frac{\sqrt{3}}{2}\hat{\mathbf{y}}, \tag{2.4}$$

where $a \approx 1.42$ Å is the carbon-carbon spacing. The diagonalization of Hamiltonian (2.2) yields the spectrum of the two π bands of graphene in tight-binding approximation (Wallace, 1947),

$$E_\pm(\mathbf{p}) = \pm t|\phi_{\mathbf{p}}| - \mu. \tag{2.5}$$

The + (−) sign in the spectrum corresponds to the conduction (valence) band.

The hexagonal Brillouin zone (BZ) of graphene shown in Fig. 1(c) has three high symmetry points: the Γ point, located at the center of the BZ, the M point, which indicates the position of the Van Hove singularities of the π–π^* bands, where the density of states (DOS) is logarithmically divergent, and the K points, where the π bands touch and the

DOS vanishes linearly. An extensive description of the band structure of graphene and its electronic properties is reviewed in detail by Castro Neto *et al.* (2009a).

B. Dirac fermion Hamiltonian

The topology of the Fermi surface in undoped graphene is defined by the six K points where the conduction and valence bands touch, $E_{\pm}(\mathbf{K}) = \pm|\phi_{\mathbf{K}}| = 0$. These special points form two sets of nonequivalent points K and K', with $\mathbf{K} = -\mathbf{K}'$ and $|\mathbf{K}| = 4\pi/3\sqrt{3}a$, which cannot be connected by the generators of the reciprocal lattice. The linearization of the spectrum around the valleys centered at $\pm\mathbf{K}$ gives rise to an effective low-energy description of the electrons that mimics the spectrum of massless Dirac particles. In this effective theory, the elementary excitations around the Fermi surface are described by a Dirac Hamiltonian (Semenoff, 1984),

$$\mathcal{H}_0 = \sum_{\sigma\mathbf{k}} \Psi^{\dagger}_{\mathbf{k}\sigma}[v\mathbf{k}\cdot\boldsymbol{\gamma} - \mu\tau_0\otimes\sigma_0]\Psi_{\mathbf{k}\sigma}, \tag{2.6}$$

where

$$\Psi_{\mathbf{k}\sigma} = (a_{\mathbf{K}+\mathbf{k},\sigma}, b_{\mathbf{K}+\mathbf{k},\sigma}, b_{-\mathbf{K}+\mathbf{k},\sigma}, a_{-\mathbf{K}+\mathbf{k},\sigma}) \tag{2.7}$$

is a four component spinor for sublattice and valley degrees of freedom. In this representation, $\gamma_i = \tau_3\otimes\sigma_i$, where $\boldsymbol{\tau}$ and $\boldsymbol{\sigma}$ are the usual Pauli matrices, which operate in the valley and sublattice spaces, respectively, ($i = 1, 2, 3$ correspond to x, y, and z directions, and $\tau_0 = 1$ and $\sigma_0 = 1$ are identity matrices). The form of the spectrum mimics the relativistic cone for massless fermions (Wallace, 1947),

$$E_{\pm}(\mathbf{k}) = \pm v|\mathbf{k}| - \mu, \tag{2.8}$$

where the Fermi velocity $v = (3/2)ta \approx 6$ eV Å is nearly 300 times smaller than the speed of light, i.e., $v \approx 1\times10^6$ m/s. From now on, we set $\hbar = k_B = 1$ everywhere, except where it is needed. For simplicity, we call the Fermi velocity v (i.e., $v_F \equiv v$) throughout this review.

The Hamiltonian (2.6) is invariant under a pseudo-time-reversal symmetry operation $\mathcal{S} = i(\tau_0\otimes\sigma_2)\mathcal{C}$, $\mathcal{S}H\mathcal{S}^{-1} = H$ ($\mathcal{C}$ is the complex conjugation operator), which is equivalent to a time-reversal operation for each valley separately. It is also invariant under a true time-reversal symmetry (TRS) operation, which involves an additional exchange between the valleys, $\mathcal{T} = (\tau_1\otimes\sigma_1)\mathcal{C}$.

In the absence of backscattering connecting the two valleys, the Hamiltonian can be decomposed in two independent valley species of Dirac fermions with opposite chiralities:

$$\mathcal{H}_{0,+} = \sum_{\sigma,\mathbf{k}} \Psi^{\dagger}_{+,\mathbf{k}\sigma}[v\mathbf{k}\cdot\boldsymbol{\sigma} - \mu]\Psi_{+,\mathbf{k}\sigma}, \tag{2.9}$$

$$\mathcal{H}_{0,-} = \sum_{\sigma,\mathbf{k}} \Psi^{\dagger}_{-,\mathbf{k}\sigma}[-v\mathbf{k}\cdot\boldsymbol{\sigma}^{*} - \mu]\Psi_{-,\mathbf{k}\sigma}, \tag{2.10}$$

where $\Psi_{\pm,\mathbf{k}\sigma} = (a_{\pm\mathbf{K}+\mathbf{k},\sigma}, b_{\pm\mathbf{K}+\mathbf{k},\sigma})$ are two component spinors. In this review, unless otherwise specified, we arbitrarily choose one of the two cones and assume an additional valley degeneracy in the Hamiltonian. So valley indexes will be generically omitted unless explicitly mentioned. A more detailed description of the symmetry properties of the graphene Hamiltonian can be found in Gusynin, Sharapov, and Carbotte (2007).

C. Polarization function

The Green's function of graphene is a 2×2 matrix represented in the sublattice basis by

$$\hat{G}(\mathbf{k},\tau) = \begin{pmatrix} G_{aa} & G_{ab} \\ G_{ba} & G_{bb} \end{pmatrix},$$

where $G_{aa} = -\langle T[a_{\mathbf{k}}(\tau)a^{\dagger}_{\mathbf{k}}(0)]\rangle$ and so on, with τ as the imaginary time. In the low-energy sector of the spectrum, close to the Dirac points, the noninteracting Green's function is $\hat{G}^{(0)}(\mathbf{k}, i\omega) = [i\omega + \mu - v\mathbf{k}\cdot\boldsymbol{\sigma}]^{-1}$, or, equivalently, in a chiral representation,

$$\hat{G}^{(0)}(\mathbf{k}, i\omega) = \frac{1}{2}\sum_{s=\pm}\frac{1 + s\hat{\sigma}_{\mathbf{k}}}{i\omega + \mu - sv|\mathbf{k}|}, \tag{2.11}$$

where $\hat{\sigma}_{\mathbf{k}} = \boldsymbol{\sigma}\cdot\mathbf{k}/|\mathbf{k}|$ is twice the quantum mechanical helicity operator for a Dirac fermion with momentum $\mathbf{k}$, and $s = \pm$ labels the two branches with positive and negative energy in one cone. It is clear that the positive and negative branches within the same cone also have opposite helicities.

The polarization function in one loop is calculated directly from the bubble diagram shown in Fig. 2,

$$\Pi^{(1)}(\mathbf{q}, i\omega) = N\sum_{\mathbf{p}}\sum_{s,s'}\mathcal{F}_{s,s'}(\mathbf{p},\mathbf{q}) \times \frac{f[E_{s'}(\mathbf{p}+\mathbf{q})] - f[E_s(\mathbf{p})]}{E_{s'}(\mathbf{p}+\mathbf{q}) - E_s(\mathbf{p}) - i\omega}, \tag{2.12}$$

where $f(E) = (e^{E/T} + 1)^{-1}$ is the Dirac-Fermi distribution, with T as temperature, $N = 4$ is the degeneracy for two spins and two valleys, and

$$\mathcal{F}_{s,s'}(\mathbf{p},\mathbf{q}) = \tfrac{1}{4}\mathrm{tr}(1 + ss'\hat{\sigma}_{\mathbf{p}}\hat{\sigma}_{\mathbf{p}+\mathbf{q}}) \tag{2.13}$$

are the matrix elements due to the overlap of wave functions for intraband ($s = s'$) and interband ($s = -s'$) transitions. "tr" means trace over the sublattice indexes. In a more explicit form, $\mathcal{F}_{s,s'}(\mathbf{p},\mathbf{q}) = [1 + ss'\cos\theta_{\mathbf{p},\mathbf{p}+\mathbf{q}}]/2$, where θ is the angle between $\mathbf{p}$ and $\mathbf{p}+\mathbf{q}$. The full momentum, frequency, and chemical potential dependence of Eq. (2.12) is shown in Figs. 3(a)–3(d).

In metals, screening is a many-body property directly related to the polarizability of the electrons around the Fermi surface. In graphene, because the DOS vanishes linearly around the Dirac points $\rho(E) \propto |E-\mu|/v^2$, exactly at the neutrality point ($\mu = 0$) the screening of charge is completely suppressed, and the polarization function describes the susceptibility of the vacuum to particle-hole pair production, exactly as in the diagonal time component of the

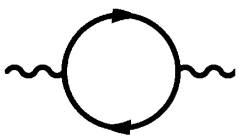

FIG. 2. Diagram for the polarization bubble corresponding to Eq. (2.12).

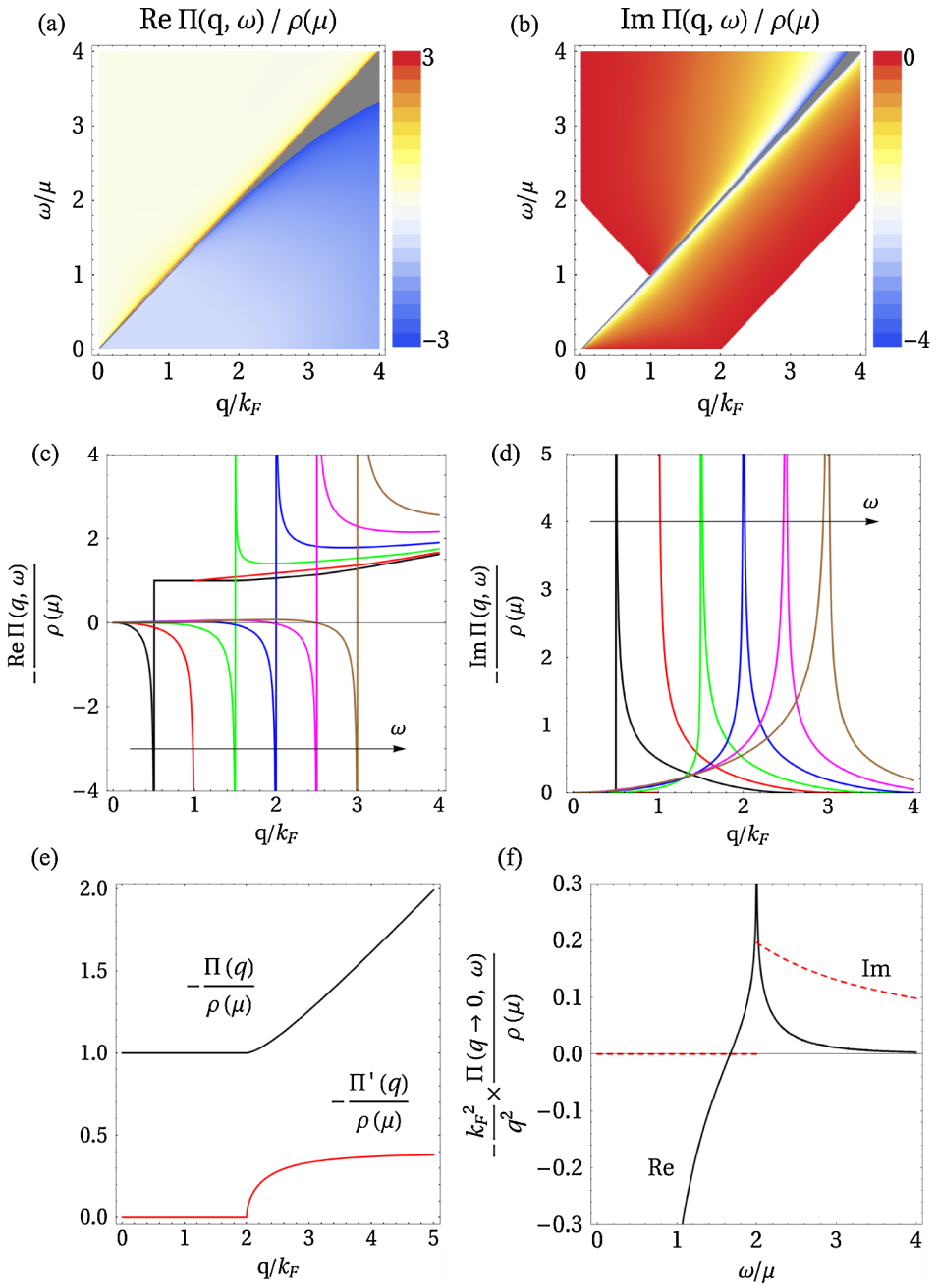

FIG. 3 (color online). Polarization bubble $\Pi^{(1)}(q, \omega)$ for graphene, within the Dirac approximation. (a), (b) A density plot of the real and imaginary parts of the polarization bubble $\Pi^{(1)}(q, \omega)$ defined in Eq. (2.12), and normalized to the DOS at the Fermi level $\rho(\mu)$. (c), (d) Present constant frequency cuts at $\omega/\mu = 0.5, 1.0, 1.5, 2.0, 2.5, 3.0$. (e) The static limit $\Pi^{(1)}(q, 0)$, whose closed form expression is written in Eq. (2.16). Notice the transition from a constant value ($q < 2k_F$) to the linear in q dependence at large momenta. The derivative of the polarization is shown in the same panel, and can be seen to vary continuously. (f) The real (solid) and imaginary (dashed) parts of the uniform limit (2.17).

polarization tensor in massless quantum electrodynamics (QED), QED_{2+1} (Pisarski, 1984; Appelquist *et al.*, 1988; González, Guinea, and Vozmediano, 1994),

$$\Pi^{(1)}(q, \omega) = -\frac{1}{4}\frac{q^2}{\sqrt{v^2q^2 - \omega^2}}. \tag{2.14}$$

Here we have performed a Wick rotation to real frequencies $i\omega \to \omega + 0^+$. Since the Fermi surface in this case is just a point, there is no phase space for intraband excitations at zero temperature due to the Pauli principle. The process of creation of particle-hole pairs involves incoherent excitations of electrons from the lower to the upper band. The continuum of particle-hole excitations is well defined for all virtual transitions with $\omega > vq$.

For finite μ there is a crossover in the behavior of the polarization function. The DOS around the Fermi level is finite and the intraband excitations dominate the infrared behavior of the polarization. For $vq \ll |\mu|$ and $\omega \ll |\mu|$, the leading term in the polarization function is (Shung, 1986a)

$$\Pi^{(1)}(q,\omega) \approx -\frac{2|\mu|}{\pi v^2}\left(1-\frac{\omega}{\sqrt{\omega^2-v^2q^2}}\right). \tag{2.15}$$

As in a Fermi liquid, there is a particle-hole continuum for $\omega < vq$, which is due only to intraband transitions. The polarization function in graphene is a regular function everywhere except at $|\omega| = vq$, where it has an on-shell singularity delimiting the border of the particle-hole continuum.

The polarization was derived originally by Shung (1986a) and later rederived by many (Ando, 2006; Barlas *et al.*, 2007; Hwang and Das Sarma, 2007; Wunsch *et al.*, 2006). These results rely on the cone approximation, which ignores contributions coming from the nonlinear part of the spectrum. In addition, the band width is assumed to be infinite. Although the charge polarization for Dirac fermions in 2D is well behaved and does not require cutoff regularization in the ultraviolet, the physical cutoff of the band D generates small corrections that vanish only in the $D \to \infty$ limit. In this sense, the "exact" expression for the static polarization function ($\omega = 0$) for arbitrary momentum is

$$\Pi^{(1)}(q,0) = -\frac{2k_F}{\pi v} + \theta(q-2k_F)\frac{q}{2\pi v}\left[\frac{2k_F}{q}\sqrt{1-\left(\frac{2k_F}{q}\right)^2} + \sin^{-1}\left(\frac{2k_F}{q}\right) - \frac{\pi}{2}\right], \tag{2.16}$$

where $k_F = |\mu|/v$ is the Fermi momentum and $\theta(x)$ is a step function. The static polarization is plotted in Fig. 3(e).

At $q \approx 2k_F$, the static polarization exhibits a crossover from a 2DEG to Dirac fermion behavior. For details of the polarization function in the 2DEG, see Fig. 4. As in the 2DEG, the polarization of graphene is constant for $q < 2k_F$. For $q > 2k_F$, it eventually becomes linear in q for large momenta. At the crossover, the static polarization and its first derivative are continuous at $q = 2k_F$. The discontinuity only appears in the second derivative. This is distinct from the 2DEG case, where the first derivative is discontinuous. The difference will affect the spacial dependence of the Friedel oscillations in the two systems.

In the opposite limit, for arbitrary ω and $q \to 0$, the polarization function becomes

$$\Pi^{(1)}(q \to 0, \omega) = \frac{q^2}{2\pi\omega}\left[\frac{2|\mu|}{\omega} + \frac{1}{2}\ln\left(\frac{2|\mu|-\omega}{2|\mu|+\omega}\right)\right], \tag{2.17}$$

which is shown in Fig. 3(f). The presence of a pocket of electrons (holes) around the Dirac points opens a gap in the particle-hole continuum for interband excitations ($\omega > vq$). From Eq. (2.17), it is clear that the imaginary part of the polarization function at small momentum is zero unless $\omega > 2|\mu|$ [Fig. 3(b)]. This occurs because the phase space for vertical interband excitations is Pauli blocked for $\omega < 2|\mu|$, generating a gap for optical absorption in the infrared. At finite q, the threshold for interband transitions is $\omega > 2|\mu| - vq$ for $q < 2k_F$, as shown schematically in Fig. 5.

D. Collective modes and screening

The Coulomb interaction among the electrons in graphene gives rise to collective modes and metallic screening when the Fermi level is shifted away from the Dirac points. In a 2D system, the bare Coulomb interaction is given by

$$V(q) = \frac{2\pi e^2}{\epsilon_0 q}, \tag{2.18}$$

where e is the charge of the electron and ϵ_0 is the effective dielectric constant of the medium. For graphene in contact with air and a substrate with dielectric constant κ, $\epsilon_0 = (1+\kappa)/2$. In most of the experiments, graphene lies on top of some substrate such as SiO_2 or SiC, where dielectric effects are moderate (for instance, the dielectric constant of SiO_2 is $\kappa \approx 4$). The background dielectric constant can be significantly enhanced in the presence of substrates in contact with strong dielectric liquids such as ethanol ($\kappa \approx 25$) or water ($\kappa \approx 80$) (Jang *et al.*, 2008; Ponomarenko *et al.*, 2009).

As usual, the collective modes follow from the zeros of the dielectric function

$$\epsilon(q,\omega) = \epsilon_0[1 - V(q)\Pi^{(1)}(q,\omega)], \tag{2.19}$$

calculated here in the random phase approximation (RPA). Since graphene is a 2D system, the collective plasmon mode is gapless. The leading term in the polarization for small frequency and momenta (compared to k_F) is shown in Eq. (2.15). From it one can easily extract the infrared dependence of the plasmon,

$$\omega_p(q) = \sqrt{(2\mu e^2/\epsilon_0)q}, \tag{2.20}$$

which follows the same dispersion as the plasmon encountered in the 2DEG. The $\sqrt{q}$ dependence of the plasmon was recently confirmed by a high resolution energy loss spectroscopy measurement in graphene (Liu *et al.*, 2008). Additional corrections due to the interband excitations (which are absent in the 2DEG) can be absorbed into the definition of the background dielectric constant (Shung, 1986a),

$$\epsilon_0(q) \approx \epsilon_0 - \frac{qe^2}{2\omega_p(q)}\ln\left(\frac{2|\mu|-\omega_p(q)}{2|\mu|+\omega_p(q)}\right). \tag{2.21}$$

As in the 2DEG, the screened Coulomb interaction for $q < 2k_F$ is

$$\frac{V(q)}{\epsilon(q,0)} = \frac{1}{\epsilon_0}\frac{2\pi e^2}{q+q_{\mathrm{TF}}}, \tag{2.22}$$

where $q_{\mathrm{TF}} = 4\pi e^2 k_F/v\epsilon_0$ is the Thomas-Fermi (TF) momentum ($k_F = |\mu|/v$), which sets the size of the screening cloud. In the presence of an external charged impurity Ze, the induced charge δZ has a nonoscillatory component coming from the $q \to 0$ limit of the polarization that decays as $(k_F r^3)^{-1}$ (as in a 2DEG), and an oscillatory part which corresponds to the Friedel oscillations at $q = 2k_F$. The Friedel oscillations in graphene decay as $\cos(2k_F r)/k_F r^3$, different from the 2DEG case, where the decay is of the form $\cos(2k_F r)/r^2$. The difference is caused by the fact that the static polarization function in the 2DEG has a cusp at $q = 2k_F$, whereas in graphene the first derivative is continuous [cf. Figs 3(e) and 4(e)].

For undoped graphene, $V(q)\Pi^{(1)} = -(\pi/2)e^2/v\epsilon_0$ [see Eq. (2.14)], and the static dielectric function is a constant. The effective Coulomb interaction in this case is

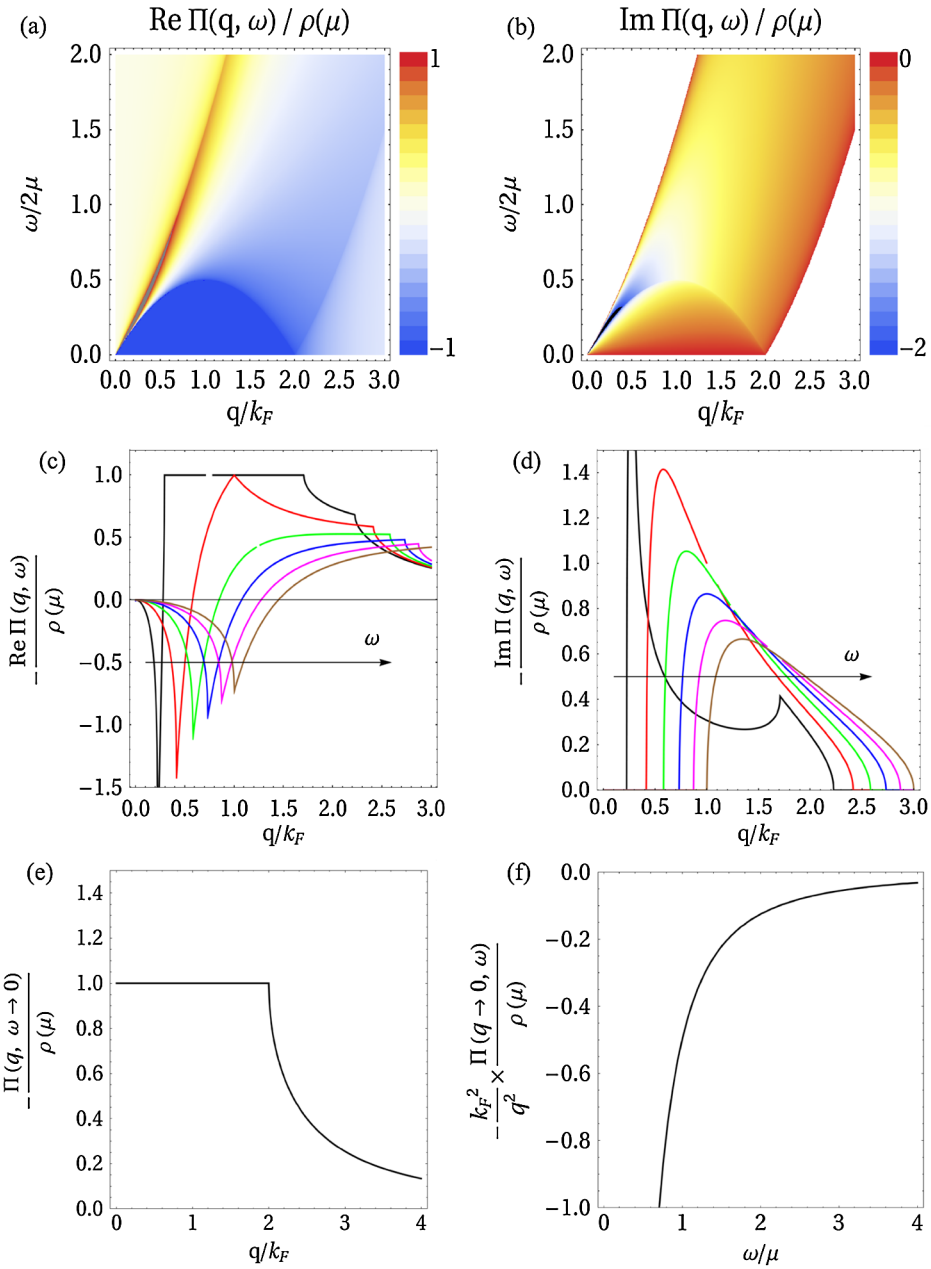

FIG. 4 (color online). Polarization bubble $\Pi^{(1)}(q, \omega)$ for the conventional 2DEG. (a), (b) A density plot of the real and imaginary parts of the polarization bubble $\Pi^{(1)}(q, \omega)$ normalized to the DOS at the Fermi level. (c), (d) Constant frequency cuts at $\omega/\mu = 0.5, 1.0, 1.5, 2.0, 2.5, 3.0$. (e) The static limit $\Pi^{(1)}(q, 0)$ and (f) the uniform limit $\Pi^{(1)}(0, \omega)$.

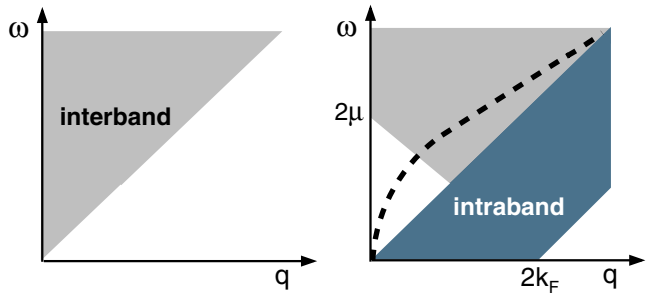

FIG. 5 (color online). Colored regions represent the particle-hole continuum of graphene due to interband and intraband transitions. Left: half-filled case; right: finite μ case, away from half-filling. Dashed line: acoustic plasmon for the single layer ($\omega_p \propto \sqrt{\mu q}$).

$$\frac{V(q)}{\epsilon(q,0)} = \frac{1}{\epsilon_{\rm RPA}} \frac{2\pi e^2}{q}, \tag{2.23}$$

where $\epsilon_{\rm RPA} = \epsilon_0 + (\pi/2)e^2/v$ is the effective background dielectric constant, renormalized by the interband transitions. Additional many-body effects resulting from self-energy insertions in the bubbles logarithmically renormalize this correction to zero in the $q \to 0$ limit, as will be clear in Sec. III. On the dynamical side, inserting Eq. (2.14) into Eq. (2.19), one can easily see that no collective modes are allowed in undoped graphene, at zero temperature, within the RPA framework. At half-filling, RPA is justified in the limit of a large number of fermionic species N which favors diagrams with a maximal number of bubbles at each order

of perturbation theory. In graphene, the physical number of species is $N = 4$, and additional corrections beyond RPA coming from the exciton channel near the on-shell singularity of the bubble $|\omega| \sim vq$ were shown to generate a new acoustic plasmon mode (Gangadharaiah, Farid, and Mishchenko, 2008). In the static limit ($\omega \to 0$), vertex corrections in the bubble are perturbatively small and RPA can be justified in the calculation of the dielectric function even at half-filling (Kotov, Uchoa, and Castro Neto, 2008). The structure of perturbation theory in graphene will be discussed in detail in Sec. III.

In addition to the low-energy acoustic mode due to intraband transitions, graphene has also two high energy optical plasmons generated by interband excitations around the Van Hove singularities of the $\pi - \pi^*$ bands, and also by optical transitions between the $\sigma - \pi^*$ and $\pi - \sigma^*$ bands (Eberlein *et al.*, 2008; Kramberger *et al.*, 2008). The measured optical gaps of the π and $\pi - \sigma$ band plasmons in graphene are 4.5 and 15 eV, respectively. Similar modes were also observed in graphite, where they appear blue shifted to 7 and 24 eV, respectively, according to optical data (Taft and Philipp, 1965), x-ray measurements (Shulke *et al.*, 1988), and *ab initio* calculations (Marinopoulus *et al.*, 2004).

E. Infinite stack of layers

In the case of an infinite stack of graphene layers, the Hamiltonian term for the Coulomb interaction among all electrons can be written in real space as

$$\mathcal{H}_C = \frac{e^2}{\epsilon_0} \int d^3\mathbf{r} d^3\mathbf{r}' \hat{n}(\mathbf{r}) \frac{1}{|\mathbf{r} - \mathbf{r}'|} \hat{n}(\mathbf{r}'), \tag{2.24}$$

where $\hat{n}(\mathbf{r})$ is the 3D particle density operator. In the absence of interlayer hopping, as in the case, for example, of several graphite intercalated compounds, the electrons remain confined in each layer, but the unscreened Coulomb lines fill the entire space in between the layers, coupling all electrons in the system. In that case, we may constrain the local density operator $\hat{n}$ to be in the form (Visscher and Falikov, 1971)

$$\hat{n}(\mathbf{r}) \to d \sum_{l=-\infty}^{\infty} \hat{n}(\mathbf{r}) \delta(z - ld), \tag{2.25}$$

where l is an integer labeling the layers and d is the distance between layers. In momentum space, making a discrete sum over the layers, the Coulomb interaction between all electrons is

$$\mathcal{H}_C = \frac{e^2}{\epsilon_0} \int d^3\mathbf{k} \hat{n}(-\mathbf{k}) V(\mathbf{k}) \hat{n}(\mathbf{k}), \tag{2.26}$$

where

$$V(\mathbf{k}) = 2\pi d \frac{e^2}{\epsilon_0 q} S(q, k_z) \tag{2.27}$$

with $\mathbf{k} = (\mathbf{q}, k_z)$, $\mathbf{q}$ is an in-plane momentum, and (Fetter, 1974)

$$S(q, k_z) = \frac{\sinh(qd)}{\cosh(qd) - \cos(k_z d)} \tag{2.28}$$

is the structure factor for a stack with an infinite number of layers. In the limit when the distance between the layers d is small, Eq. (2.27) recovers the isotropic case $V(k) = 4\pi(e^2/\epsilon_0)/(q^2 + k_z^2)$, whereas in the opposite limit ($d \to \infty$) one gets the 2D case, $V(k) = 2\pi d(e^2/\epsilon_0)/q$. In any case, the polarization function must be integrated over a cylindrical Fermi surface of height $2\pi/d$, and as such $\Pi^{(1)}(q, \omega)$ acquires an additional factor of $1/d$ compared to the single layer case. The extension of this problem to include the interlayer hopping dispersion in the polarization was considered by Guinea (2007).

Away from the neutrality point ($\mu \neq 0$), instead of a single acoustic mode as in the monolayer, the zeros in the dielectric function of the multilayer generate a plasmon band, where the modes are labeled by $k_z \in [-\pi/d, \pi/d]$. For $q \ll 1/d$, the plasmon dispersion is (Shung, 1986a)

$$\omega_p^2(q, k_z) = \frac{2\mu e^2}{\epsilon_0} q S(q, k_z). \tag{2.29}$$

In the $k_z = 0$ mode, the charge fluctuations between different layers are in phase, and the resulting plasmon mode is optical, $\omega_p^2(q, 0) \approx (4\mu e^2/\epsilon_0 d) + \frac{3}{4}(vq)^2$. For $\omega_p(q) > 2\mu$, this mode is damped by the particle-hole continuum due to interband transitions (see Fig. 6), in agreement with energy loss spectroscopy data (Laitenberger and Palmer, 1996). The out-of-phase modes (for $k_z \neq 0$) are acoustic. At the edge of the plasmon band, the mode $k_z = \pm\pi/d$ disperses linearly with the in-plane momentum $\omega_p(q, \pm\pi/d) = \sqrt{\mu e^2 d/\epsilon_0} q$, in contrast with the 2DEG dispersion ($\omega_p \propto \sqrt{q}$) present in the single layer. Except for the lack of an interband particle-hole continuum and the associated damping, similar plasmon band features are also expected in the 2D layered electron gas, for fermions with quadratic dispersion (Hawrylak, 1987).

F. *f*-sum rule

The f-sum rule is a generic statement about conservation of the number of particles and results from the analytical properties of the retarded charge susceptibility. It can be generically defined as (Nozières, 1964)

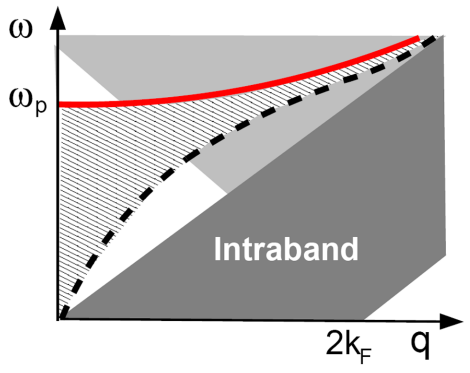

FIG. 6 (color online). Plasmon band (hatched region) for an infinite stack of graphene layers. Solid line: optical mode $k_z = 0$. Dashed line: acoustic mode $k_z = \pi/d$, $\omega_p \propto \sqrt{\mu} q$, with linear dispersion, at the edge of the band. All the other modes in between are acoustic. Adapted from Shung, 1986a.

$$\int_{-\infty}^{\infty} d\omega\, \omega\, \mathrm{Im}\chi^R(k,\omega) = \pi\langle[[\mathcal{H}, \hat{n}(-\mathbf{k})], \hat{n}(\mathbf{k})]\rangle, \tag{2.30}$$

where $\mathcal{H}$ is the Hamiltonian, $\hat{n}$ is the particle density operator, χ^R is a retarded charge susceptibility, $\chi(\mathbf{k},\tau) = \langle T[\hat{n}(\mathbf{k},\tau)\hat{n}(-\mathbf{k},0)]\rangle$, and $\langle\cdots\rangle$ is an expectation value calculated in some basis.

As in any solid, the exact electronic Hamiltonian of graphene can be decomposed into a Hamiltonian of *free* electrons, plus a periodic potential due to the lattice, and interactions. If the interactions depend only on densities, the commutators in Eq. (2.30) can be calculated exactly, and the only term that survives is the kinetic energy due to the free electrons,

$$\langle[[\mathcal{H}, \hat{n}(-k)], \hat{n}(k)]\rangle = N_e \frac{k^2}{m}, \tag{2.31}$$

where m is the bare electron mass and N_e is the number of fermions in the band. Choosing, for example, a basis of noninteracting fermions, the sum rule in graphene is

$$\int_{-\infty}^{\infty} d\omega\, \omega \mathrm{Im}\Pi^{(1)}(k,\omega) = \pi\frac{N_e k^2}{m} \tag{2.32}$$

as in metals, where $\Pi^{(1)}(k,\omega)$ is the bare polarization bubble, calculated using the full noninteracting spectrum (dictated by the lattice symmetry). The validity of the f-sum rule does not require Galilean invariance of the quasiparticles, but of free electrons, which are not relativistic and hence obey the Schrodinger equation.

For low-energy effective Hamiltonians, such as the Dirac Hamiltonian in graphene (which do not include the periodicity of the spectrum in the Brillouin zone), the f-sum rule above is still formally satisfied when applied for the electrons (holes) in the conduction (valence) band only, as can be explicitly checked by direct substitution of the polarization due to intraband transitions, Eq. (2.15), into Eq. (2.32). The number of electrons (holes) in this band $N_e = k_F^2 A/\pi$, where $A = 3\sqrt{3}a^2/2$ is the unit cell area, is set by the size of the Fermi surface, and the verification of the sum rule follows as in a Fermi liquid.

The Dirac Hamiltonian, however, violates the f-sum rule (2.32) when interband transitions are taken into account. In that case, the left-hand side of Eq. (2.32) becomes independent of the chemical potential, consistent with the fact that (Sabio, Nilsson, and Castro Neto, 2008)

$$\langle[[\mathcal{H}, \hat{n}(-\mathbf{k})], \hat{n}(\mathbf{k})]\rangle = k^2\frac{D}{4} \tag{2.33}$$

for a Dirac Hamiltonian, where D is the ultraviolet cutoff. A similar dependence with the cutoff also occurs in the true 3D relativistic problem, where the sum rule reflects the number of particles contained in the vacuum of the theory, which is formally divergent (Goldman and Drake, 1982; Ceni, 2001). In graphene, as in any two-band semimetal or semiconductor, the validity of the f-sum rule is physically recovered when the periodicity of the electronic spectrum is restored back into the Hamiltonian.

III. QUASIPARTICLES IN GRAPHENE

The quasiparticle properties of graphene are modified by the presence of long-range Coulomb interactions. Their effects are especially pronounced when the Fermi energy is close to the Dirac point ($\mu \approx 0$), and can result in strong renormalization of the Dirac band structure (the Fermi velocity v), and the quasiparticle residue (Z). Consequently, many physical characteristics, such as the compressibility, spin susceptibility, and the specific heat can be strongly affected by interactions. Even when the Fermi surface is large and the system is a Fermi liquid, there are strong modifications of the physics near the Dirac point due to the presence of additional peaks in the quasiparticle decay rate, related to plasmon-mediated decay channels. Even reconstruction of the Dirac cone structure near the charge neutrality point appears possible, as indicated by recent angle-resolved photoemission spectroscopy (ARPES) measurements. All of these effects are sensitive to the value of the Coulomb interaction constant in graphene α.

A. Low-energy behavior near the Dirac point

1. Weak-coupling analysis

The interaction parameter which characterizes the strength of the Coulomb interaction in graphene is [Eq. (1.4)]

$$\alpha = \frac{e^2}{\epsilon_0 v}. \tag{3.1}$$

At $k_F = 0$, screening is absent, and the interaction potential in momentum space

$$V(\boldsymbol{p}) = \frac{2\pi e^2}{\epsilon_0 p}. \tag{3.2}$$

The value of $\alpha = 2.2/\epsilon_0$ depends on the dielectric environment since, as previously discussed, $\epsilon_0 = (1+\kappa)/2$ for graphene in contact with air and a substrate with dielectric constant κ. In vacuum, $\alpha = 2.2$.

In the case of small coupling $\alpha \ll 1$, we can employ standard perturbation theory, involving the perturbative computation of the self-energy $\Sigma(\boldsymbol{k},\omega)$, which enters in a standard way the Dirac fermion Green's function (GF), for a given valley

$$G(\boldsymbol{k},\omega) = \frac{1}{\omega\sigma_0 - v\boldsymbol{\sigma}\cdot\boldsymbol{k} - \Sigma(\boldsymbol{k},\omega) + i\sigma_0 0^+\mathrm{sgn}(\omega)}. \tag{3.3}$$

It is convenient to decompose the self-energy into two pieces with different pseudospin structure

$$\Sigma(\boldsymbol{k},\omega) = \Sigma_0(\boldsymbol{k},\omega) + \Sigma_v(\boldsymbol{k},\omega), \qquad \Sigma_0 \propto \sigma_0, \quad \Sigma_v \propto \boldsymbol{\sigma}\cdot\mathbf{k}, \tag{3.4}$$

where $\sigma_0 = 1$ is the unit matrix, which from now on will not be written explicitly. Then we have

$$G(\boldsymbol{k},\omega) = \frac{Z}{\omega - Z(v\boldsymbol{\sigma}\cdot\boldsymbol{k} + \Sigma_v)}, \tag{3.5}$$

where Z is the quasiparticle residue

$$Z^{-1} = 1 - \partial\Sigma_0/\partial\omega, \tag{3.6}$$

and Σ_v is responsible solely for the velocity renormalization.

The first order diagram shown in Fig. 7(a) is the Hartree-Fock exchange contribution, and can be readily evaluated (we denote by $G^{(0)}$ the noninteracting GF)

$$\Sigma^{(1)}(\boldsymbol{k}, \omega) = i \int \frac{d^2 p d\varepsilon}{(2\pi)^3} G^{(0)}(\boldsymbol{k} + \boldsymbol{p}, \omega + \varepsilon) V(\boldsymbol{p}), \tag{3.7}$$

which at low external momenta exhibits a logarithmic singularity

$$\Sigma^{(1)}(\boldsymbol{k}, \omega) = \Sigma_v^{(1)}(\boldsymbol{k}) = \frac{\alpha}{4} v \boldsymbol{\sigma} \cdot \boldsymbol{k} \ln(\Lambda/k), \quad \Lambda/k \gg 1. \tag{3.8}$$

At this order, we have $\Sigma_0 = 0$, i.e., $Z = 1$ due to the frequency independence of the interaction potential, and the quasiparticle velocity increases

$$v(k) = v\left(1 + \frac{\alpha}{4} \ln(\Lambda/k)\right), \qquad \Lambda/k \gg 1. \tag{3.9}$$

The ultraviolet cutoff $\Lambda \sim 1/a$ represents the momentum scale up to which the spectrum is Dirac-like.

While the linearity of the spectrum in graphene was realized a long time ago (Wallace, 1947), in the context of studying graphite formed by layers of graphene, the self-energy correction (3.8) due to interactions was first investigated perturbatively much later by González, Guinea, and Vozmediano (1994). The nontrivial velocity renormalization is due to the unscreened, long-range Coulomb interactions. Similar logarithmic divergencies were also found in gapless 3D semiconductors, where the Dirac spectrum originated from special symmetries (Abrikosov and Beneslavskii, 1971).

The above calculation forms the basis of the renormalization group (RG) analysis. In the RG spirit one integrates out the high momentum degrees of freedom, i.e., regions of momenta $\Lambda > |\boldsymbol{p}| > \Lambda_1$, and the results vary with the quantity $\ln(\Lambda/\Lambda_1) \equiv l$. Here we denote by l the RG parameter, so that the infrared limit corresponds to $l \to \infty$ [i.e., one integrates down to the infrared scale $k \to 0$, $l = \ln(\Lambda/k)$]. From Eq. (3.9) we obtain

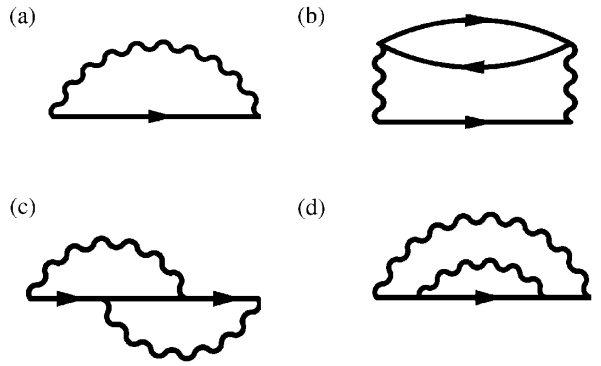

FIG. 7. Self-energy diagrams: (a) first order Hartree-Fock, (b) second order loop diagram (first diagram in the RPA series), (c) second order exchange (vertex correction) diagram, and (d) rainbow diagram.

$$\frac{dv}{dl} = \frac{\alpha}{4} v = \frac{e^2}{4\epsilon_0}. \tag{3.10}$$

This equation has to be supplemented with an additional equation reflecting the absence of charge (e^2) renormalization

$$\frac{de^2}{dl} = 0. \tag{3.11}$$

There are several ways to understand this. It was argued early on that the vertex function does not acquire any divergent contributions, which is related to the expected regular behavior of the polarization operator to all orders in graphene (González, Guinea, and Vozmediano, 1994). More recently, explicit calculations up to two-loop order were performed (Kotov, Uchoa, and Castro Neto, 2008; de Juan, Grushin, and Vozmediano, 2010); it was confirmed that the vertex function is finite in the low-energy limit. In addition, direct examination of the polarization function at two-loop level (Kotov, Uchoa, and Castro Neto, 2008) found that the self-energy correction, Fig. 8(a), acquires a logarithmic divergence which can be absorbed into the renormalized velocity $v(k)$ [Eq. (3.9)], while the vertex correction of Fig. 8(b) is finite

$$\frac{2\pi e^2}{\epsilon_0 q} \Pi^{(2b)}(q, 0) = \text{finite} = -0.53\alpha^2. \tag{3.12}$$

Incidentally, this contribution leads to enhancement of the dielectric static screening [i.e., the dielectric constant beyond linear (RPA) order becomes $\epsilon = 1 + \frac{\pi}{2}\alpha + 0.53\alpha^2$].

Alternatively, one can argue that in two-dimensional field theories with Coulomb interactions the charge e^2 does not flow because it appears as a coefficient in a nonanalytic term in the action (Ye and Sachdev, 1998; Herbut, 2006). The conclusion then is that only the quasiparticle velocity and residue (see below) are renormalized. In particular, at first order we can combine Eqs. (3.10) and (3.11) into a single one reflecting the renormalization (running) of the coupling α

$$\frac{d\alpha}{dl} = -\frac{\alpha^2}{4}. \tag{3.13}$$

Therefore, we have an infrared stable fixed point at $\alpha = 0$, and the flow towards it is logarithmic

$$\alpha(k) \sim \frac{4}{\ln(\Lambda/k)}, \qquad k \to 0. \tag{3.14}$$

Thus, the Coulomb interactions are marginally irrelevant. This is equivalent to a logarithmically divergent velocity $v(k) \sim (e^2/4)\ln(\Lambda/k)$, $k \to 0$.

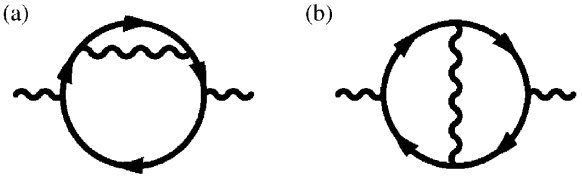

FIG. 8. (a) Self-energy and (b) vertex corrections to the polarization bubble.

a. Two-loop results

It is instructive to examine corrections beyond first order (Mishchenko, 2007; Vafek and Case, 2008), since additional effects appear, such as renormalization of Z. For example, the first diagram in the RPA series shown in Fig. 7(b) is

$$\Sigma^{(2b)}(\boldsymbol{k},\omega) = i\int \frac{d^2p\,d\varepsilon}{(2\pi)^3} G^{(0)}(\boldsymbol{k}+\boldsymbol{p},\omega+\varepsilon) \times [V(\boldsymbol{p})]^2 \Pi^{(1)}(\boldsymbol{p},\varepsilon). \tag{3.15}$$

An explicit evaluation at low energies and momenta gives a single logarithmic divergence

$$\Sigma^{(2b)}(\boldsymbol{k},\omega) = -\frac{N\alpha^2}{24}(\omega + v\boldsymbol{\sigma}\cdot\boldsymbol{k})\ln(\Lambda/k), \quad k/\Lambda \to 0, \tag{3.16}$$

i.e., $\Sigma_0^{(2b)} = -(N\alpha^2/24)(\omega)\ln(\Lambda/k)$ and $\Sigma_v^{(2b)} = -(N\alpha^2/24)v\boldsymbol{\sigma}\cdot\boldsymbol{k}\ln(\Lambda/k)$. Because the polarization bubble is proportional to the number of fermion flavors $N=4$ (valley + spin), we have explicitly written the N dependence. By comparing with Eq. (3.5), we find that the velocity is changed by an amount $(-N/24 - N/24)\alpha^2 v\ln(\Lambda/k)$.

In addition, other diagrams at second order have to be added, such as the vertex correction of Fig. 7(c). Most importantly, this diagram is also proportional to $\ln\Lambda$. Collecting all contributions, one finds the RG equation for the velocity flow (Vafek and Case, 2008)

$$\frac{dv}{dl} = \frac{\alpha}{4}v - \left(\frac{N}{12} - \delta\right)\alpha^2 v, \tag{3.17}$$

with $\delta \approx 0.03$. One observes that the contribution of the "RPA" diagram is numerically dominant at second order (it is larger than the rest by a factor of 10 for $N=4$). In addition, the second order tendency is a decrease of the velocity. Consequently, a finite coupling fixed point is possible at $\alpha_c \approx 0.8$. This fixed point is infrared unstable since near α_c, $dv/dl = -C(\alpha-\alpha_c)v$, $C>0$, i.e., for $\alpha>\alpha_c$, v flows towards zero (α flows to ∞) while for $\alpha<\alpha_c$, v flows towards ∞ (α flows to zero.) Of course, it is not clear that this estimate is reliable since the fixed point value α_c is not small, and we used perturbation theory ($\alpha \ll 1$) to derive this result. On the other hand, a flow towards strong coupling for $\alpha>\alpha_c$ is consistent with the formation of an excitonic insulator (mass generation), for which strong evidence has accumulated by now, as discussed in Sec. III.B. Recent numerical simulations give the value $\alpha_c \sim 1$ (see Sec. III.B).

Finally, we also find that Z is renormalized at second order, since the self-energy is frequency dependent. From Eq. (3.6), we can expand to second order of bare perturbation theory $Z \approx 1 - (N\alpha^2/24)\ln(\Lambda/k)$, which would lead us to an RG equation for Z: $dZ/dl = -(N\alpha^2/24)Z$, to be solved together with Eq. (3.13) or Eq. (3.17), depending on the desired level of approximation. Alternatively, Eq. (3.6) is already written in a "nonperturbative" way. Ignoring for the moment the running of α, we have at low energies

$$Z = \frac{1}{1+(N\alpha^2/24)\ln(\Lambda/k)} \to \frac{24}{N\alpha^2\ln(\Lambda/k)}, \quad k/\Lambda \to 0. \tag{3.18}$$

This result, along with the previous one for $\Sigma_0^{(2b)}$, brings us to the infrared behavior (we use ω and k interchangeably in the infrared limit)

$$Z \sim \frac{1}{\alpha^2|\ln(\omega)|}, \qquad \Sigma_0 \sim \alpha^2\omega|\ln(\omega)|, \qquad \omega \to 0. \tag{3.19}$$

This is characteristic of a marginal Fermi liquid (González, Guinea, and Vozmediano, 1994; Das Sarma, Hwang, and Tse, 2007). However, this regime is never achieved if the running of α is taken into account, as is intuitively clear from the above equations. As we will see later from the solution of the RG equations for Z and α, in fact Z tends to level off in the infrared, and the system has well-defined quasiparticles.

It is interesting to note that trigonal distortions, which change the band structure away from the Dirac equation, are modified by the electron-electron interaction, and their irrelevance at low energies is enhanced (Foster and Aleiner, 2008). As a result, the linear dispersion becomes an even more robust feature of graphene (Roldán, López-Sancho, and Guinea, 2008).

b. Influence of disorder

Before proceeding, we briefly address the effect of disorder. Two major sources of disorder are scalar potential random fluctuations (e.g., formation of electron-hole puddles) and vector gauge field randomness, related to the formation of ripples. Starting with the latter, i.e., a gauge field coupled to the Dirac fermion pseudospin $\boldsymbol{\sigma}\cdot\mathbf{A}$, and characterized by variance Δ, $\langle A_\mu(\mathbf{r_1})A_\nu(\mathbf{r_2})\rangle = \Delta\delta_{\mu\nu}\delta(\mathbf{r_1}-\mathbf{r_2})$, one can readily derive the corresponding RG equations in the weak disorder and interactions limit (Stauber, Guinea, and Vozmediano, 2005; Herbut, Juricic, and Vafek, 2008)

$$\frac{d\Delta}{dl} = 0, \qquad \frac{d\alpha}{dl} = -\frac{\alpha^2}{4} + \frac{\Delta}{\pi}\alpha. \tag{3.20}$$

Gauge field disorder itself is not renormalized, while the interplay of disorder and interactions leads to a line of attractive fixed points located at $\alpha^* = 4\Delta/\pi$, as shown in Fig. 9. Physically the variance is related to the characteristic

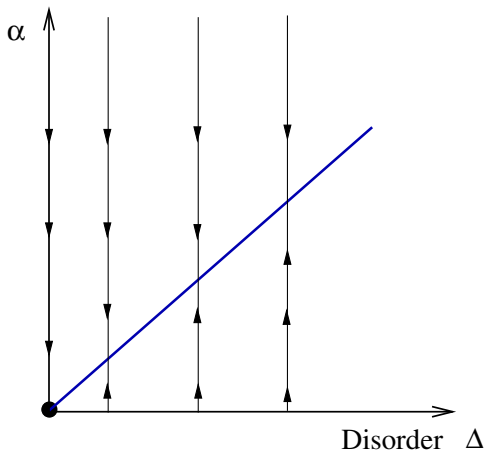

FIG. 9 (color online). An attractive line of fixed pints for interactions and gauge field disorder.

height h and length L of the corrugations of the surface, $\Delta \sim h^4/L^2a^2$. Thus, weak disorder generically shifts the fixed point away from $\alpha = 0$, while strong disorder can have an even more profound effect (Sec. VI.C).

In addition, for weak interactions, the inclusion of scalar (density fluctuations) disorder turns out to be a relevant perturbation which grows under renormalization, and thus away from the perturbative regime (Aleiner and Efetov, 2006). Moreover, gauge field disorder, when combined with strong-enough interactions, can cause the interactions to grow (Vafek and Case, 2008). It has been argued that the strong-coupling regime for disorder and interactions generically occurs when all types of disorder consistent with graphene's symmetries are included (Foster and Aleiner, 2008).

A detailed analysis of this complex situation is beyond the scope of this work, and from now on we continue our discussion of clean graphene.

2. Strong-coupling and RPA analysis

The full RPA treatment was performed by many (González, Guinea, and Vozmediano, 1999; Das Sarma, Hwang, and Tse, 2007; Polini *et al.*, 2007; Son, 2007; Foster and Aleiner, 2008; Kotov, Uchoa, and Castro Neto, 2009). Here we mostly follow Son (2007). The RPA self-energy is shown diagrammatically in Fig. 10, and corresponds to

$$\Sigma^{(\mathrm{RPA})}(\boldsymbol{k},\omega) = i\int \frac{d^2p\,d\varepsilon}{(2\pi)^3} G^{(0)}(\boldsymbol{k}+\boldsymbol{p},\omega+\varepsilon) V^{\mathrm{RPA}}(\boldsymbol{p},\varepsilon). \tag{3.21}$$

The RPA potential is given by

$$V^{\mathrm{RPA}}(\boldsymbol{p},\varepsilon) = \frac{2\pi e^2}{\epsilon_0 p - 2\pi e^2 \Pi^{(1)}(p,\varepsilon)}. \tag{3.22}$$

Quite remarkably, at low momenta one can evaluate the singular contribution to the self-energy analytically

$$\Sigma^{(\mathrm{RPA})}(\boldsymbol{k},\omega) = \frac{8}{N\pi^2}[-F_0(\lambda)\omega + F_1(\lambda) v \boldsymbol{\sigma}\cdot\boldsymbol{k}]\ln(\Lambda/k), \tag{3.23}$$

where we have defined

$$\lambda = \frac{\pi}{8} N\alpha. \tag{3.24}$$

This parameter measures the importance of polarization loop contributions relative to the bare Coulomb term [i.e., the ratio of the second term to the first in the denominator of Eq. (3.22)]. The RPA is generally expected to be valid when the loops dominate over other diagrams, i.e., $N \gg 1$. Provided this condition is satisfied, we can also analyze the strong-coupling regime $\lambda \gg 1$, and the crossover toward the weak-coupling one ($\lambda \ll 1$), i.e., we can hope to cover a wide range of α values.

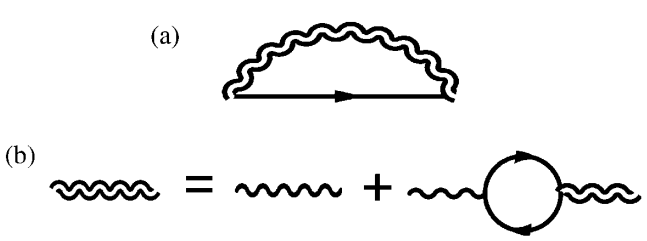

FIG. 10. RPA self-energy, which includes an infinite resummation of polarization bubbles.

The calculated functions F_0 and F_1 in Eq. (3.23) are

$$F_1(\lambda) = \begin{cases} -\frac{\sqrt{1-\lambda^2}}{\lambda}\arccos\lambda - 1 + \frac{\pi}{2\lambda}, & \lambda < 1, \\ \frac{\sqrt{\lambda^2-1}}{\lambda}\ln(\lambda+\sqrt{\lambda^2-1}) - 1 + \frac{\pi}{2\lambda}, & \lambda > 1, \end{cases} \tag{3.25}$$

$$F_0(\lambda) = \begin{cases} -\frac{2-\lambda^2}{\lambda\sqrt{1-\lambda^2}}\arccos\lambda - 2 + \frac{\pi}{\lambda}, & \lambda < 1, \\ \frac{\lambda^2-2}{\lambda\sqrt{\lambda^2-1}}\ln(\lambda+\sqrt{\lambda^2-1}) - 2 + \frac{\pi}{\lambda}, & \lambda > 1 \end{cases}. \tag{3.26}$$

This leads to the system of RG equations for v and Z, to leading order in $1/N$

$$\frac{dv}{dl} = \frac{8}{N\pi^2}[F_1(\lambda) - F_0(\lambda)]v, \tag{3.27}$$

$$\frac{dZ}{dl} = -\frac{8}{N\pi^2}F_0(\lambda)Z. \tag{3.28}$$

At strong coupling $\lambda \gg 1$ one finds

$$\frac{dv}{dl} = \frac{8}{N\pi^2}v, \tag{3.29}$$

$$\frac{dZ}{dl} = -\frac{8}{N\pi^2}\ln(2\lambda)Z. \tag{3.30}$$

The first equation, after integration, leads to the low-energy result ($k \to 0$)

$$v(k)/v = \left(\frac{\Lambda}{k}\right)^{\eta}, \qquad \eta = \frac{8}{N\pi^2}, \tag{3.31}$$

which implies that the quasiparticle dispersion is of the form

$$\omega(k) \sim k^z, \qquad z = 1 - \frac{8}{N\pi^2}. \tag{3.32}$$

The existence of the anomalous velocity dimension η, and consequently $z \neq 1$, is characteristic of the strong-coupling regime $N\alpha \to \infty$ (Son, 2007). However this strongly coupled fixed point is infrared unstable, since, due to the velocity increase, the RG for α flows towards weak coupling. (One also expects that for certain $N < N_c$ and $\alpha \gg 1$ an excitonic gap can appear, which will be discussed in Sec. III.B.) In this regime Z can be approximated perturbatively (in $1/N$) as

$$Z \approx 1 - \frac{8}{\pi^2}\frac{1}{N}\ln(N\alpha\pi/4)\ln(\Lambda/k), \qquad N\alpha \gg 1, \tag{3.33}$$

which can be obtained from Eq. (3.30) by ignoring the scale dependence of λ.

In the weak-coupling limit $\lambda \ll 1$, it is easy to verify that we recover the previous result (3.10) for the velocity v (leading to a flow for α towards zero), and the previously encountered perturbative equation for Z

$$\frac{dZ}{dl} = -\frac{8}{N\pi^2}\frac{\lambda^2}{3}Z, \quad \text{i.e.,} \quad Z \approx 1 - \frac{N}{24}\alpha^2 \ln(\Lambda/k). \tag{3.34}$$

The last formula is written to first order in $N\alpha$.

Equations (3.33) and (3.34) allow us to have a qualitative understanding of the behavior of Z as a function of the RG scale l. If the initial value of α is large, at the initial RG steps Z decreases logarithmically fairly fast [due to the weak $\ln(\alpha)$ dependence in Eq. (3.33), even though α itself decreases]. Eventually, when α has decreased substantially $\{\alpha \sim [\ln(\Lambda/k)]^{-1}\}$, Z is governed by Eq. (3.34), meaning that Z will stop decreasing, and will level off for $l = \ln(\Lambda/k) \to \infty$.

A numerical evaluation of the system of Eqs. (3.27) and (3.28) confirms the anticipated behavior and is shown in Fig. 11 (González, Guinea, and Vozmediano, 1999). [The equation for the coupling $\lambda = (\pi/8)Ne^2/\epsilon_0 v$ is obtained by observing that $d\lambda/dl = (-1/v^2)(\pi/8)N(e^2/\epsilon_0)dv/dl$, due to the lack of charge renormalization.] We conclude that the flow of λ is towards weak coupling, no matter how large its initial value is. Z does not renormalize to zero at low energy due to the RG decrease of λ. Thus, near the weak-coupling infrared fixed point, the marginal Fermi liquid

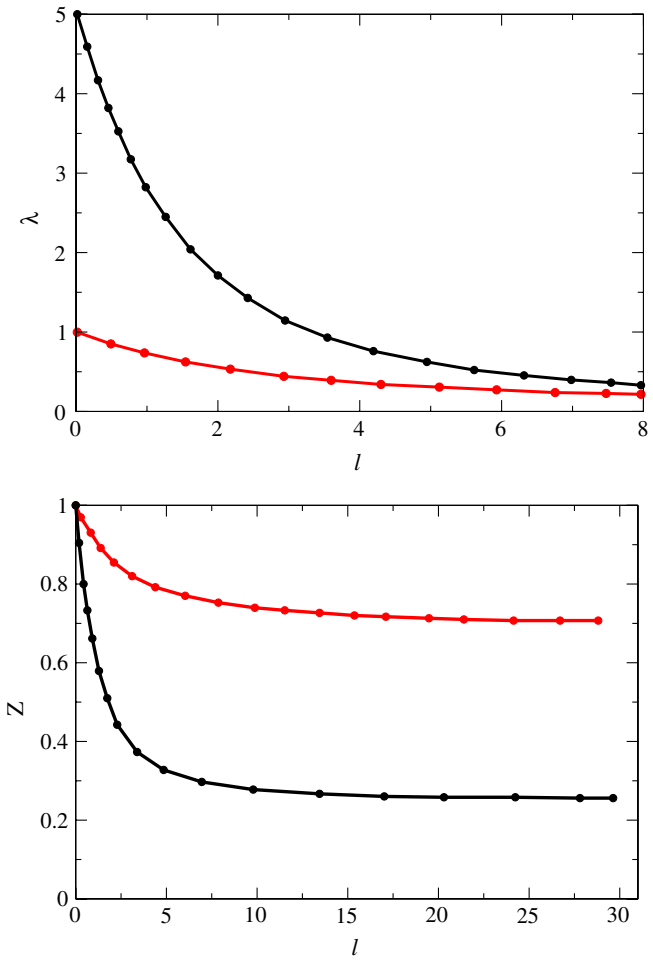

FIG. 11 (color online). RG flow of the coupling λ and the quasiparticle residue Z as a function of the RG scale l; the infrared limit is at $l \to \infty$. From González, Guinea, and Vozmediano, 1999.

[Eq. (3.19)] is ultimately not reached, and the system behaves as a Fermi liquid (although the quasiparticle decay rate is non-Fermi-liquid-like). At higher energies, however (away from the fixed point but still much lower than the bandwidth $v\Lambda$), the system exhibits marginal Fermi-liquid behavior.

At finite (but still small) density away from the Dirac point, i.e., $k \neq 0$, the logarithmic behavior in the infrared is cut off by the Fermi momentum, i.e., $\ln(\Lambda/k_F)$, $k_F/\Lambda \to 0$, and the RG stops away from the fixed point. For comparison with experiments, the flow toward this stable fixed point should be stopped at a scale set by the (small) density, temperature, or frequency, whichever is higher.

One can also perform a numerical evaluation of the main RPA equation (3.21) (Polini *et al.*, 2007). For small density, and with logarithmic accuracy [$\ln(\Lambda/k_F)$], this is equivalent to evaluating, by using the notation of Eq. (3.23), and taking into account Eqs. (3.4), (3.5), and (3.6)

$$Z = (1 - \partial\Sigma^{(\mathrm{RPA})}/\partial\omega)^{-1} = \frac{1}{1 + (8/N\pi^2)F_0(\lambda)\ln(\Lambda/k_F)}, \tag{3.35}$$

$$v^*/v = Z\left(1 + \frac{8}{N\pi^2}F_1(\lambda)\ln(\Lambda/k_F)\right). \tag{3.36}$$

Here v^* is the renormalized velocity. At any finite density the numerical evaluation of $\Sigma^{(\mathrm{RPA})}$ also picks up finite (subleading) contributions, while it can be shown (Polini *et al.*, 2007) that the leading perturbative results such as Eqs. (3.33) and (3.34) are readily reproduced. The RPA results are shown in Fig. 12, and exhibit the natural density dependence tendency, i.e., the strongest renormalization occurs at the lowest densities. Similar RPA results have been obtained by Das Sarma, Hwang, and Tse (2007).

A significant velocity enhancement was observed in the infrared conductivity (Li *et al.*, 2008), which reported around a 15% increase of the Fermi velocity, having value as high as $v^* \approx 1.25 \times 10^6$ m/s at the lowest densities (compared to $v \approx 1.1 \times 10^6$ m/s at higher density). The system is at a finite Fermi energy $\mu \approx 0.2$ eV. However, the velocity renormalization is not logarithmic, and it is not clear what is the origin of this effect.

A recent study of suspended graphene which measures the cyclotron mass (Elias *et al.*, 2011) has detected significant logarithmic renormalization of the Fermi velocity, having the high value $v^* \approx 3 \times 10^6$ m/s at the lowest densities $n < 10^{10}$ cm^{-2}, almost 3 times the value at high density ($n > 4 \times 10^{11}$ cm^{-2}), see Fig. 13(a). The logarithmic renormalization of the velocity predicted by theory fits the data fairly well, and thus offers a direct proof that the Dirac cones can be reshaped by long-range electron-electron interactions near the Dirac point, as schematically shown in Fig. 13(b). Finally, ARPES measurements of quasifreestanding graphene grown on the carbon face of SiC have also detected logarithmic velocity renormalization (Siegel *et al.*, 2011).

3. Quasiparticle lifetime

The inverse quasiparticle lifetime (decay rate) due to electron-electron interactions $1/\tau_{ee}$ is an important quantity which is relevant to many properties of graphene (and Fermi

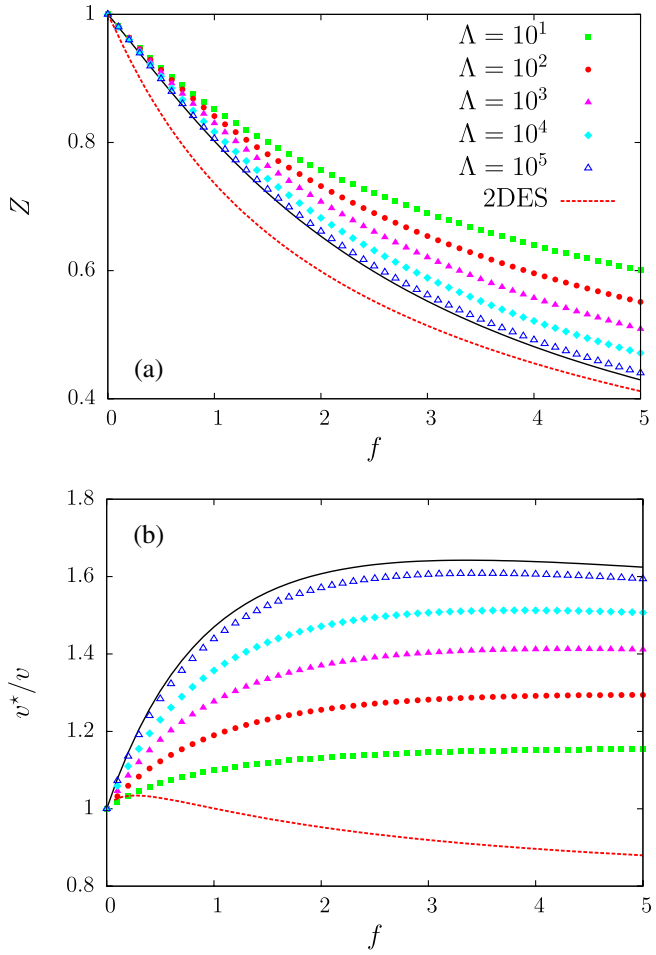

FIG. 12 (color online). Exact evaluation of the RPA equations for (a) the quasiparticle residue and (b) the Fermi velocity. On the horizontal axis f is defined as $f \equiv N\alpha$. Λ is in units of k_F. Values of Λ from $\sim 10^2$ to 10^1 correspond to density n from $n \sim 10^{11}$ to $\sim 10^{13}$ cm^{-2} (while $\Lambda \sim 10^3$ is ultralow density $n \sim 10^9$ cm^{-2}). The values of Λ (in units of k_F) can be converted into density n via $\Lambda/k_F \approx 220/\sqrt{\tilde{n}}$, $\tilde{n} = n/(10^{10}\ \text{cm}^{-2})$. The curves labeled 2DES refer to the case of 2DEG with parabolic bands, where $f = \sqrt{2}r_s$ and $r_s \sim 1/\sqrt{n}$. From Polini *et al.*, 2007.

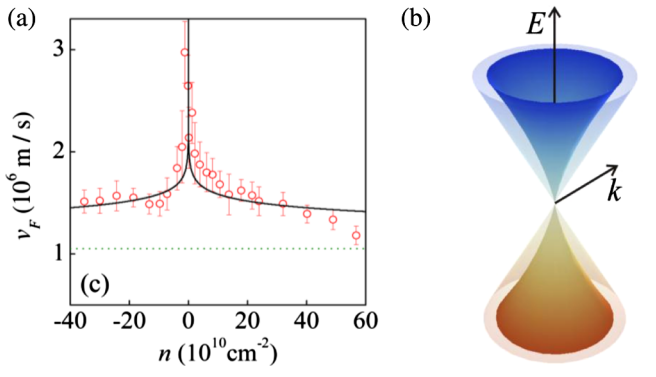

FIG. 13 (color online). (a) Density dependence of the velocity for suspended graphene. The solid line is the result of RG treatment within RPA [Eq. (3.27)]. (b) Reshaping of the Dirac cone due to the interaction-driven renormalization (increase) of the Fermi velocity at low momenta. The outer cone represents the linear Dirac spectrum without many-body effects. From Elias *et al.*, 2011.

systems in general). In particular, the dependence of $1/\tau_{ee}$ on energy (or temperature) determines the importance of the electron-electron interaction contribution, relative to other processes, to transport, and interpretation of spectroscopic features, such as ARPES.

The decay rate is determined by the imaginary part of the self-energy $\mathrm{Im}\,\Sigma(\boldsymbol{k}, \omega)$. The first diagram, which has energy dependence, and thus a nonzero imaginary part, is the one bubble diagram of Fig. 7(b), whose real part is given by Eq. (3.16), i.e., behaves as in Eq. (3.19) at low energies. We can therefore deduce, for energies and momenta close to the mass shell (González, Guinea, and Vozmediano, 1996),

$$\mathrm{Im}\,\Sigma^{(2b)}(\boldsymbol{k}, \omega) \sim \alpha^2 \theta(\omega - vk)\omega, \qquad \omega \approx vk, \tag{3.37}$$

i.e., the decay rate is linear in energy. In addition, there is an on-shell ("light cone," $\omega = vk$) discontinuity, where the rate experiences a jump. This on-shell behavior is due to the fact that, for $\omega < vk$, there is no phase space available for virtual interband particle-hole excitations (see Fig. 5), whereas such excitations are possible for $\omega > vk$.

The above behavior is valid at the Dirac point and $T = \mu = 0$, while for small T, μ, it is valid for energies of order $\max(T, \mu)$. Note also that the linear energy behavior of Eq. (3.37) is very different from the conventional Fermi-liquid result $\mathrm{Im}\,\Sigma \sim \omega^2$ (Das Sarma, Hwang, and Tse, 2007), which would occur for a finite Fermi surface ($\mu \neq 0$) and is due to intraband particle-hole excitations.

The on-shell discontinuity present at the one-loop level, Eq. (3.37), disappears when the full RPA self-energy is evaluated (Fig. 10). In this case, one obtains (Khveshchenko, 2006)

$$\mathrm{Im}\,\Sigma^{(\mathrm{RPA})}(\boldsymbol{k}, \omega) \sim \ln(\pi\alpha)\theta(\omega - vk)(\omega - vk), \qquad \omega \approx vk. \tag{3.38}$$

Away from the mass shell, the energy dependence is naturally linear

$$\mathrm{Im}\,\Sigma^{(\mathrm{RPA})}(\boldsymbol{k}, \omega) \sim \ln(\pi\alpha)\omega, \qquad \omega \gg vk. \tag{3.39}$$

The full dependence $\mathrm{Im}\,\Sigma^{(\mathrm{RPA})}(\boldsymbol{k}, \omega)$ has to be evaluated numerically (Das Sarma, Hwang, and Tse, 2007), and the results confirm the smooth rise of $\mathrm{Im}\,\Sigma^{(\mathrm{RPA})}$ from the point $\omega = vk$.

In the limit of zero doping $\mu \to 0$, when the system approaches the fixed point $\alpha = 0$, we argued previously that the residue Z does not approach zero (i.e., the marginal Fermi-liquid behavior ultimately does not manifest itself.) On the other hand, the marginal Fermi-liquid behavior is expected to be much more robust as far as the inverse lifetime, $\mathrm{Im}\,\Sigma \sim \omega$, is concerned, because the running of the coupling $\alpha(\omega)$ only introduces logarithmic variation on top of a much stronger linear energy dependence.

The linear decay rate discussed above is consistent with ARPES experiments (Bostwick *et al.*, 2006; Zhou *et al.*, 2008), and STM measurements of graphene on graphite (Li, Luican, and Andrei, 2009) [see also the discussion in Grushin, Valenzuela, and Vozmediano (2009)].

B. Spontaneous mass generation

It is an intriguing possibility that graphene can undergo a metal-insulator transition for strong enough Coulomb interaction α, due to an excitonic pairing mechanism. We restrict ourselves to the charge neutrality point $\mu = 0$ since the excitonic pairing tendency decreases quickly beyond that.

1. Finite explicit mass

Before outlining the main results, we mention that an explicit gap can also open in graphene under certain conditions that depend on graphene's environment. For example, there are suggestions of a detectable gap in situations when graphene is on a substrate with specific symmetry, creating sublattice asymmetry in the graphene plane, and thus making the graphene electrons massive (gapped) (Zhou *et al.*, 2007). Gaps can also be produced by confining the electrons into finite-size configurations, such as quantum dots (Ponomarenko *et al.*, 2008). In these cases, the gap generation mechanism is not intrinsic to graphene, and the value of the gap depends strongly on the external conditions. However, even in such situations, interactions can play an important role by increasing the gap.

Consider a gap arising from an external potential that alternates between the two sublattices

$$\mathcal{H}_{\text{mass}} = \Delta_0 \sum_{\sigma, i\in A} n_\sigma(\mathbf{R}_i) - \Delta_0 \sum_{\sigma, i\in B} n_\sigma(\mathbf{R}_i). \tag{3.40}$$

Consequently, an additional pseudospinor structure related to σ_3 is generated, and the new Green's function has the form

$$G(\boldsymbol{k}, \omega) = \frac{1}{\omega - \upsilon \boldsymbol{\sigma}\cdot\boldsymbol{k} - \Delta_0\sigma_3 - \Sigma(\boldsymbol{k}, \omega)}. \tag{3.41}$$

Here Δ_0 is the explicit "mass" of the graphene electrons [while $\Sigma(\boldsymbol{k}, \omega)$ contains the information about interactions, assumed to perturbatively renormalize all the other terms]. The new spectrum is then $E(k) = \pm\sqrt{\upsilon^2k^2 + \Delta_0^2}$, with a gap of $2\Delta_0$. Computing the Hartree-Fock interaction correction to Δ_0 leads to a renormalized mass $\tilde{\Delta}_0$ (Kane and Mele, 2005; Kotov, Pereira, and Uchoa, 2008a):

$$\tilde{\Delta}_0/\Delta_0 \approx 1 + \frac{\alpha}{2}\ln(D/\Delta_0). \tag{3.42}$$

The above enhancement can be substantial. For example, for a bare gap due to spin-orbit coupling $\Delta_0 \sim 10^{-3}$ meV (Min *et al.*, 2006; Yao *et al.*, 2007) and taking into account the bandwidth $D = \upsilon\Lambda \approx 7$ eV, the logarithmic factor is around 15. In fact, one should integrate the RG equation for the renormalized mass $\tilde{\Delta}_0$ as a function of $\ln(\Lambda)$ simultaneously with the equation for the running coupling $\alpha[\ln(\Lambda)]$, Eq. (3.13), down to the lowest infrared scale $\sim\Delta_0$ (bare gap). This leads to the stronger dependence $\tilde{\Delta}_0/\Delta_0 = [1 + (\alpha/4)\ln(D/\Delta_0)]^2$ (Kane and Mele, 2005), and the perturbative expansion of this result is Eq. (3.42). It is interesting to note that the logarithmic mass renormalization formula in graphene, Eq. (3.42), is similar to the well-known expression for the electromagnetic mass of the electron (accounting for radiative corrections) in 3D relativistic QED (Weisskopf, 1939).

2. Excitonic mass generation

We now turn to the possibility of spontaneous gap generation due to long-range Coulomb interactions [we set the explicit gap $\Delta_0 = 0$ in Eq. (3.41)]. In relativistic QED in two space (plus one time) dimensions, QED_{2+1}, the study of this phenomenon, called chiral symmetry breaking, started quite a while ago (Pisarski, 1984; Appelquist *et al.*, 1986), and is still going strong today. Graphene is actually different from QED_{2+1} because only the fermions are confined to a 2D plane, while the field lines extend through the whole 3D space. In addition, the Coulomb interaction in graphene can be considered instantaneous since the speed of light c is much larger than the Fermi velocity ($\upsilon \approx c/300$). Hence, Lorenz invariance is not respected, which reflects the nonrelativistic, purely band origin of the Dirac quasiparticles. The analysis in relativistic QED reveals that dynamical mass can be generated below a critical number of fermion flavors N_c, with the mass scale set by the coupling itself, which has dimension of energy in pure QED_{2+1}. A transition is also found in nonrelativistic graphene, where the generated mass scale is related to the ultraviolet energy cutoff (bandwidth $D = \upsilon\Lambda$) since the coupling α is dimensionless in this case.

The gap equation can be obtained as a self-consistent solution for the self-energy within RPA (i.e., vertex corrections are neglected), and is referred to as the Schwinger-Dyson equation. It has the form

$$\Delta(\boldsymbol{p}, \varepsilon) = i\int \frac{d^2k d\omega}{(2\pi)^3} \frac{V^{\text{RPA}}(\boldsymbol{p}-\boldsymbol{k}, \varepsilon-\omega)\Delta(\boldsymbol{k}, \omega)}{\omega^2 - \upsilon^2k^2 - \Delta^2(k) + i0^+}. \tag{3.43}$$

The structure of the solution has been analyzed extensively (Gorbar *et al.*, 2002; Khveshchenko and Leal, 2004; Khveshchenko, 2009; Liu, Li, and Cheng, 2009; Gamayun, Gorbar, and Gusynin, 2010) at different levels of approximation. The equation is simplified significantly if the static RPA potential is used $V^{\text{RPA}}(\mathbf{p}, 0)$ (Khveshchenko and Leal, 2004), while the dynamical equation has also been studied on shell $[\Delta(\mathbf{p}, \varepsilon = \upsilon p)]$ (Khveshchenko, 2009), as well as numerically (Liu, Li, and Cheng, 2009).

The mass gap $\Delta(p)$ has strong momentum dependence, due to the long-range nature of the Coulomb interaction. $\Delta(p)$ decreases at large momenta and reaches maximum value at small momenta where it levels off. For a fixed physical value of $N = 4$, a transition to a gapped state is found above a critical coupling α_c. Some of the calculated values are $\alpha_c = 0.92$ (Gamayun, Gorbar, and Gusynin, 2010), and $\alpha_c = 1.13$ (Khveshchenko, 2009). At strong coupling $\alpha \to \infty$ the gap is nonzero only below a critical number of fermion flavors (since the effective interaction scales as $1/N$ in this limit); for example, $N_c \approx 7.2$ (Khveshchenko, 2009) and $N_c \approx 7$ (Liu, Li, and Cheng, 2009).

Near the critical coupling the low-momentum gap scales as

$$\Delta(0) \propto D\exp\left(-\frac{C}{\sqrt{\alpha_{\text{eff}} - \alpha_{\text{eff},c}}}\right), \tag{3.44}$$

where C is a constant, the critical $\alpha_{\text{eff},c} = 1/2$, and the form of the effective coupling α_{eff} depends on the level of approximation used, for example, an improvement over the static RPA potential leads to $\alpha_{\text{eff}} = \alpha/(1 + N\pi\alpha/8\sqrt{2})$

(which gives $N_c \approx 7.2$, $\alpha \gg 1$, and $\alpha_c = 1.13$, $N = 4$) (Khveshchenko, 2009). The form of Eq. (3.44) suggests that the transition is of infinite order (Berezinskii-Kosterlitz-Thouless type). Even though Eq. (3.44) is only valid near the critical coupling, numerical results find that the gap in units of the bandwidth $\Delta(0)/D$ is exponentially small in a wide range of couplings (Khveshchenko and Leal, 2004). Since $D \approx 7$ eV, this implies $\Delta(0) \sim$ meV, i.e., a rather small gap value. Finally, recent work that takes into account the renormalization of the coupling constant and the quasiparticle residue suggests that α_c could be much larger than previously found (González, 2010; Sabio, Sols, and Guinea, 2010a).

The above results are based on various approximation schemes and it is therefore important to compare them with direct numerical simulations of the lattice field theory model. Recent Monte Carlo calculations (Hands and Strouthos, 2008; Drut and Lähde, 2009a; Drut and Lähde, 2009b; Drut and Lähde, 2009c) provide strong evidence that spontaneous mass generation does occur, and give comparable values for the critical couplings: $N_c \approx 9.6$, $\alpha \gg 1$ (Hands and Strouthos, 2008) and $\alpha_c = 1.1$, $N = 4$ (Drut and Lähde, 2009b). Unfortunately the Monte Carlo simulations do not allow for an exact determination of the gap size, and for that we can only rely on the previously described Schwinger-Dyson equation (leading to small gaps). For graphene deposited on SiO the value of $\alpha_{SiO_2} \approx 0.79$ and is therefore not enough to generate a gap; only experiments on ultrahigh mobility suspended samples can potentially reveal the insulating state.

The overall phase diagram of graphene in the $\alpha - N$ plane is expected to look as shown in Fig. 14, with $\alpha_c \approx 1$ and $N_c \approx 7$–9. At finite temperature one expects the existence of a critical temperature $T_c \sim \Delta(0)$, while finite doping μ very quickly destroys the gap (Liu, Li, and Cheng, 2009). Application of magnetic field perpendicular to the graphene layer leads to enhancement of the excitonic instability due to the formation of Landau levels (Khveshchenko, 2001a; Gorbar *et al.*, 2002; Gusynin *et al.*, 2006). In addition, it has been suggested that an in-plane magnetic field favors a gapped excitonic state (Aleiner, Kharzeev, and Tsvelik, 2007), due to the instability of a system of electrons and holes polarized in opposite directions.

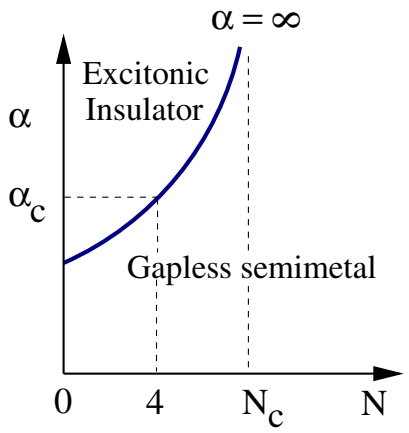

FIG. 14 (color online). Schematic phase diagram in the $\alpha - N$ plane.

The physical structure of the gapped state depends on the nature of pairing between the valleys, for example, one can have charge density wave states (Khveshchenko, 2001b) with modulation of the electronic density around the two sublattices (which corresponds to intravalley paring), or Kekule dimerization (Hou, Chamon, and Mudry, 2007), which corresponds to tripling of the unit cell (intervalley pairing). One generally expects that interactions beyond the long-range Coulomb potential, such as short-range repulsion, would favor particular states, including time-reversal symmetry broken (spin) states. Further discussion appears in Sec. V.A.

C. Finite density Fermi-liquid regime

As the density increases above half-filling, i.e., graphene is at a finite, not necessarily small, chemical potential μ, with a finite Fermi surface, a crossover towards a Fermi-liquid regime takes place. In this case, the lower (hole) band becomes irrelevant and the physics near the Fermi surface is dominated by intraband transitions in the conduction (upper) band (assuming $\mu > 0$). However, the physics near the Dirac point can still be very strongly affected due to the presence of plasmon and "plasmaron" features in the quasiparticle spectral function.

The quasiparticle width near k_F is quite similar to the case of an ordinary 2D electron gas (Das Sarma, Hwang, and Tse, 2007; Hwang and Das Sarma, 2008b; Polini *et al.*, 2008) and is proportional to the second power of energy (or temperature), as in a Fermi liquid, while the quasiparticle residue is finite at the Fermi surface.

The existence of a plasmon-related peak in the quasiparticle decay rate, which originates from intraband transitions in which an electron can decay into a plasmon, was pointed out in the context of intercalated graphite, where the physics is dominated by graphene layers (Shung, 1986b; Lin and Shung, 1996). For n-doped graphene ($\mu > 0$), which is relevant to ARPES experiments, a double feature is found in the decay rate $\mathrm{Im}\,\Sigma$: a peak at positive energies, signaling an onset of plasmon emission, and a sharp spectral feature at negative energies, below the Dirac point, and separated from it by an amount proportional to the plasmon frequency (Hwang and Das Sarma, 2008b; Polini *et al.*, 2008). This is the so-called plasmaron, a resonance which consists of a quasiparticle strongly coupled to plasmons (Lundqvist, 1967). Plasmaron features have been previously detected, for example, in optical measurements of bismuth (Tediosi *et al.*, 2007).

The above calculations were done within RPA theory. Line widths have also been analyzed via *ab initio* many-body methods (Trevisanutto *et al.*, 2008; Park *et al.*, 2009). Experiments generally show a well-pronounced linear quasiparticle spectrum (Bostwick *et al.*, 2006; Zhou *et al.*, 2007, 2008; Sprinkle *et al.*, 2009), with additional features near the Dirac point which seem to depend on the way graphene is prepared, and its purity. For example, gaplike features have been observed near the Dirac point (Zhou *et al.*, 2007) and attributed to external, substrate-related factors. Bending of the Dirac spectrum (kinklike feature) was attributed to

plasmons (Bostwick *et al.*, 2006). Most recently, manifestations of the sharp plasmaron spectral intensities have been observed in quasi-freestanding graphene (Bostwick *et al.*, 2010), where a reconstruction of the Dirac point crossing seems to take place, as shown in Fig. 15. A diamondlike shape appears due to crossing of charge and plasmaron bands. Comparison of the RPA calculation for the energy splitting with experiment leads to the value of $\alpha \approx 0.5$ (Fig. 15.) Bostwick *et al.* (2010) also suggest that the plasmaron features were obscured in earlier measurements on non-free-standing graphene (Bostwick *et al.*, 2007), due to the several times stronger screening (and consequently smaller α). Perhaps most importantly, all of the current activity in ARPES on different graphene samples reveals that the electron-electron interactions can affect strongly the physics around the Dirac point, even for relatively large density (Fermi energy).

Tunneling spectroscopy measurements, combined with *ab initio* calculations, have also found evidence for density-dependent interaction effects in the tunneling current (Brar *et al.*, 2010) which arise from the sharp spectral features in the quasiparticle decay rate below the Dirac point.

D. Physical observables

The interaction-driven singular logarithmic structure near the Dirac point (for $\mu \approx 0$) encountered in the fermion self-energy, and, in particular, the renormalization of the Fermi velocity, can manifest itself in numerous physical observables, such as the charge compressibility and the spin susceptibility, which exhibit non-Fermi-liquid behavior. Interactions can also affect the conductivity near the Dirac point, leading to deviations from the celebrated quantized value $\sigma_0 = e^2/4\hbar$ expected for free Dirac fermions (Castro Neto *et al.*, 2009a).

1. Charge and spin response

a. Compressibility

First we discuss the compressibility κ, which was recently measured (Martin *et al.*, 2007), Fig. 16, and it was concluded that no interaction effects were clearly visible in those samples. Theory predicts significant (α dependent) deviations from the free electron behavior (Barlas *et al.*, 2007; Hwang, Hu, and Das Sarma, 2007; Sheehy and Schmalian, 2007; Polini, Tomadin, Asgari, and MacDonald, 2008).

The computation of the compressibility requires knowledge of the ground state energy, which contains the first order Hartree-Fock exchange contribution $E_{\rm ex}$ and the correlation energy $E_{\rm Corr}$, describing all higher order effects. Keeping in mind applications of the theory for fairly strong coupling ($\alpha \sim 1$), the contribution of $E_{\rm Corr}$ can be substantial. The correlation energy can be readily calculated within the RPA approximation, i.e., we take $E_{\rm Corr} = E_{\rm RPA}$. The total ground

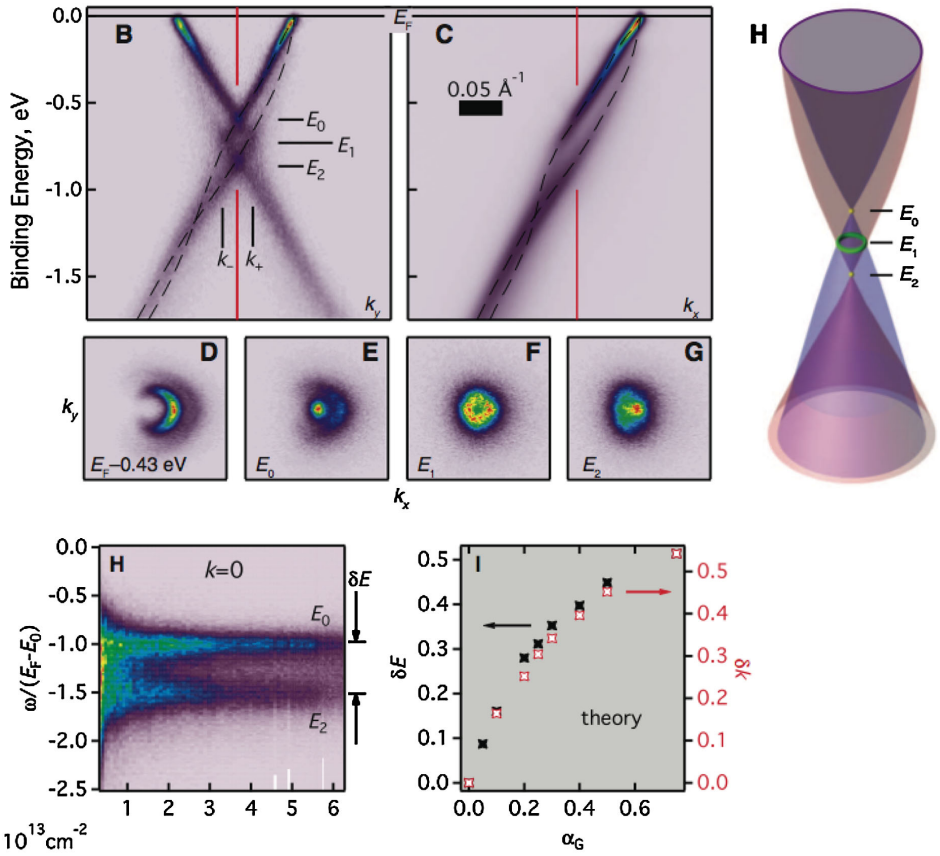

FIG. 15 (color online). ARPES data showing strong features at the Dirac point, which is below the Fermi energy (at 0). The splitting shown in (H) is attributed to the presence of "plasmarons" (quasiparticles strongly bound to plasmons) and depends on the value of α ($\alpha \approx 0.5$ fits the data). From Bostwick *et al.*, 2010.

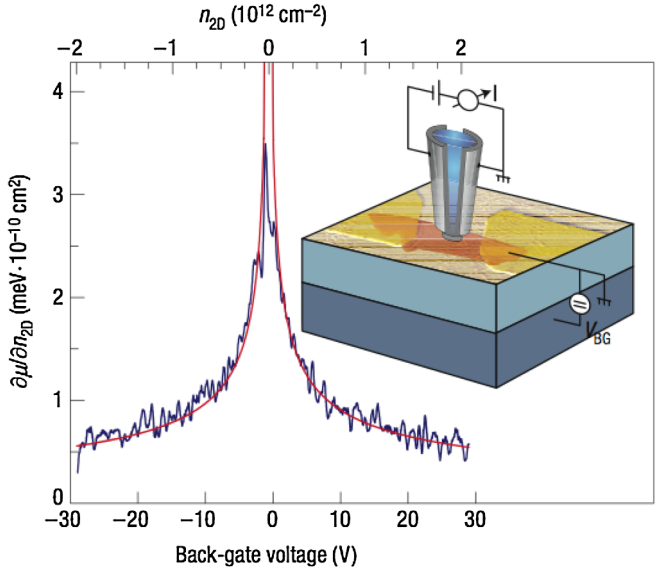

FIG. 16 (color online). Inverse compressibility, measured by Martin *et al.* (2007). The solid line is the compressibility of noninteracting Dirac fermions.

state energy E, per unit area, is the sum $E = E_{\rm kin} + E_{\rm ex} + E_{\rm RPA}$. The kinetic energy $E_{\rm kin} = (2/3)\upsilon k_F n$, and $n = (k_F)^2/\pi$ is the particle density. The inverse compressibility is then calculated as $1/\kappa = \partial^2 E/\partial n^2$, which is equivalent to the usual definition involving the variation of the chemical potential with density $1/\kappa = \partial\mu/\partial n$. For free Dirac particles this gives $1/\kappa_0 = \upsilon\sqrt{\pi/4n}$, behavior which can be clearly seen in experiment (Fig. 16).

The interaction effects in the ground state energy acquire divergent contributions in the limit of small density $k_F/\Lambda \approx 0$, similarly to the previously discussed self-energy (velocity) renormalization. Ignoring any finite (nondiverging) terms, one finds (Barlas *et al.*, 2007)

$$E_{\rm ex}/n = \frac{\alpha}{6}(\upsilon k_F)\ln(\Lambda/k_F), \qquad (k_F/\Lambda) \to 0, \tag{3.45}$$

$$E_{\rm RPA}/n = -\frac{N\alpha^2}{6}G(\alpha)(\upsilon k_F)\ln(\Lambda/k_F), \tag{3.46}$$

where the function $G(\alpha)$ is defined as $G(\alpha) = (1/2)\times \int_0^\infty dx(1+x^2)^{-2}(\sqrt{x^2+1} + N\pi\alpha/8)^{-1}$, and, in particular, at zero coupling $G(0) = 1/3$. The above results exactly follow the velocity renormalization, i.e., are equivalent to the substitution $\upsilon \to \upsilon(k_F)$ in the free compressibility $1/\kappa_0 = \upsilon\sqrt{\pi/4n}$, where $\upsilon(k_F)$ is the running velocity calculated within RPA at the infrared scale k_F. The result is particularly simple at the Hartree-Fock (exchange) level [when the velocity follows Eq. (3.9)]

$$\frac{1}{\kappa} = \upsilon\sqrt{\frac{\pi}{4n}}\left(1 + \frac{\alpha}{4}\ln(\Lambda/k_F) + O(\alpha^2)\right), \tag{3.47}$$

and was obtained by many (Barlas *et al.*, 2007; Hwang, Hu, and Das Sarma, 2007; Sheehy and Schmalian, 2007).

The above results are valid at zero temperature. We also point out that exactly at zero density $k_F = 0$, but $T \neq 0$, the compressibility behaves as $\kappa^{-1} \sim (\upsilon^2/T)[1 + (\alpha/4)\ln(T_0/T)]^2$, where T_0 is the temperature related to the ultraviolet cutoff; since $\Lambda\upsilon \approx 7$ eV, then $T_0 \approx 8\times 10^4$ K. This is easily understood since in the infrared limit near the "critical point" $n = T = 0$ it is the larger scale, either υk_F or the temperature T, which enters the physical observables (Sheehy and Schmalian, 2007).

Of course Eqs. (3.45) and (3.46) are valid only asymptotically ($k_F \to 0$), and at any finite density the compressibility should be calculated numerically. This was achieved by expressing the ground state energy via the charge response function (Barlas *et al.*, 2007).

Figure 17, upper panel, illustrates the variation of $1/\kappa$ with density for fixed interaction. Most notably, $1/\kappa$ is larger than the free value $1/\kappa_0$. Also, the full RPA implementation weakens the first order Hartree-Fock (exchange) result, due to the different signs in Eqs. (3.45) and (3.46). For example, at $\alpha = 0.8$ the RPA term is approximately $1/2$ of the exchange, and thus has to be taken into account (although the RPA effects become weaker for $\alpha \to 0$). Asymptotically,

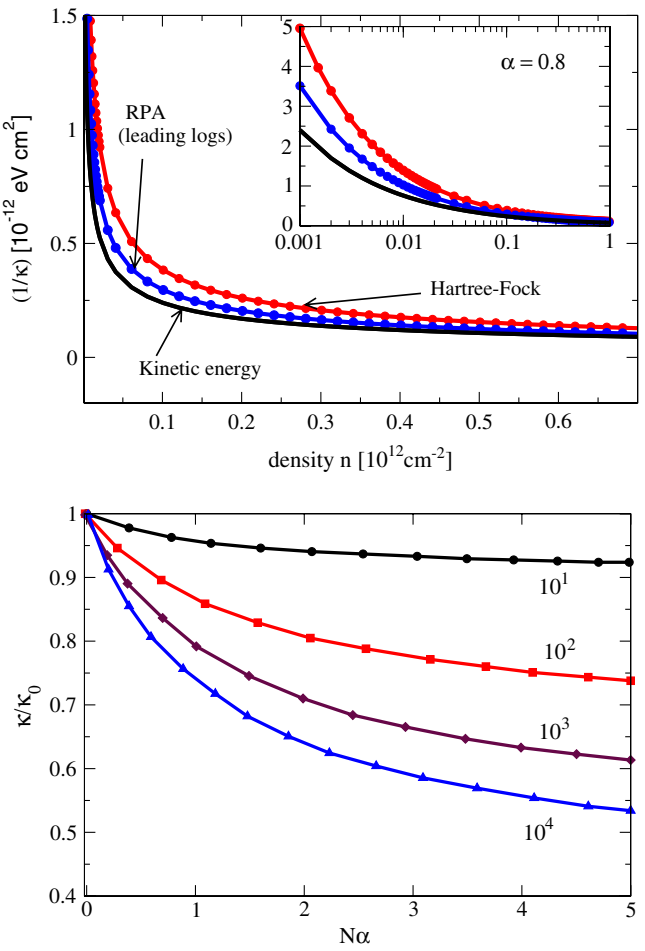

FIG. 17 (color online). Upper panel: Inverse compressibility calculated at different levels of approximation as a function of density. The inset enlarges the low-density region. Lower panel : Compressibility calculated within RPA, relative to the free level for different couplings and densities. Here $N = 4$ is the Dirac fermion degeneracy. The numbers refer to the values of Λ/k_F, which can be converted into density n via $\Lambda/k_F \approx 220/\sqrt{\tilde{n}}$, $\tilde{n} = n/(10^{10}\ {\rm cm}^{-2})$. This implies $\Lambda/k_F \sim 10^2$ for $n \sim 10^{11}\ {\rm cm}^{-2}$, and $\Lambda/k_F \sim 10$ for $n \sim 10^{13}\ {\rm cm}^{-2}$. Adapted from Barlas *et al.*, 2007.

$\kappa^{-1}/\kappa_0^{-1} \sim \ln(\Lambda/k_F)$, as $k_F/\Lambda \to 0$. The lower panel gives the variation κ/κ_0 as a function of the interaction for different densities; naturally the deviation from the free limit increases with increasing interaction and decreasing density.

The increase of the inverse compressibility κ_0/κ as a function of the interaction α (at fixed density), and with decreasing density (for fixed interaction), represents non-Fermi-liquid behavior, and reflects the lack of screening. By contrast, in a 3D (and 2D) Fermi liquid with a screened potential κ_0/κ decreases; for example, within Hartree-Fock theory, $\kappa_0/\kappa \approx 1 - r_s/6 < 1$, and eventually goes through zero, signaling an instability (Mahan, 2000) (although the critical value of r_s depends strongly on the level of approximation). Such an instability does not occur in graphene, which is related to the impossibility of Wigner crystallization (Dahal *et al.*, 2006). It should be noted that for larger densities (larger than the density range shown in Fig. 17) the logarithmic corrections become unimportant and the system recovers the Fermi-liquid behavior, i.e., eventually κ/κ_0 becomes larger than 1.

Fits of the experimental data for κ with adjusted (slightly larger) velocity $v = 1.1 \times 10^6$ m/s show that $\alpha \approx 0$ (Fig. 16), while the use of $v = 10^6$ m/s by Sheehy and Schmalian (2007) at the Hartree-Fock level produced $\alpha \approx 0.4$. On the other hand, the application of the full RPA analysis led us to conclude that $\alpha < 0.1$. It has also been argued that exchange and correlation effects vanish and do not manifest themselves at all in the compressibility (Abergel, Pietiläinen, and Chakraborty, 2009). These discrepancies indicate that the issue is still unsettled, while it is also possible (indeed, quite probable) that interaction effects are obscured by charge inhomogeneities (electron-hole puddles) in these samples. Nevertheless, theory predicts strong systemic (albeit logarithmic) deviations from Fermi-liquid theory, and it would be important to test these predictions in cleaner, more uniform, high-mobility, low-density samples.

b. Spin susceptibility

The paramagnetic spin susceptibility χ_s shows behavior very similar to the charge compressibility, i.e., $\chi_s/\chi_{s,0}$ decreases as the interaction increases (Barlas *et al.*, 2007). This is again related to the fact that χ_s^{-1} is calculated via the ground state energy, and is proportional to the Fermi velocity v. It was also pointed out that the same effect, i.e., the logarithmic growth of the exchange energy, Eq. (3.45), can lead to suppression of ferromagnetism in graphene at low densities (Peres, Guinea, and Castro Neto, 2005). The full calculation of χ_s within RPA was carried out by Barlas *et al.* (2007).

On the other hand, the orbital diamagnetic susceptibility $\chi_{\rm dia}$ is proportional to v^2, because the quasiparticle current that couples to the vector potential contains v (the magnetic field is perpendicular to the graphene plane). Therefore, interaction corrections lead to an increase of $\chi_{\rm dia}$ (Sheehy and Schmalian, 2007) and, consequently, orbital effects are expected to dominate in the susceptibility. At the Dirac point, $k_F = 0$, one finds at finite temperature

$$\chi_{\rm dia}/\chi_{\rm dia,0} = \left(1 + \frac{\alpha}{4}\ln(T_0/T)\right)^2, \tag{3.48}$$

where the noninteracting $\chi_{\rm dia,0} = -e^2v^2/6\pi c^2 T$ (Ghosal, Goswami, and Chakravarty, 2007). Here c is the speed of light. At $T = 0$, $n \neq 0$, we have $\chi_{\rm dia,0} \sim -e^2 v/c^2\sqrt{n}$, and interaction corrections readily follow from the v dependence. This result is, strictly speaking, valid for $T \ll B \ll \mu = v\sqrt{\pi n}$, whereas for $B = 0$ the orbital susceptibility is zero for $\mu \neq 0$ as $T \to 0$, and is finite only when the Fermi energy is at the Dirac point. It has been suggested that an interaction-driven positive (paramagnetic) contribution to the orbital susceptibility can therefore become dominant in doped graphene, $\chi_{\rm orb} \sim (e^2v^2/\mu c^2)\alpha|\ln\alpha|$, $\alpha \ll 1$ (Principi *et al.*, 2010).

c. Specific heat

The specific heat is logarithmically suppressed due to the suppression of the DOS $\sim v^{-2}$. Consequently, $C_V \sim C_{V,0}/[\ln(T_0/T)]^2$, $T/T_0 \ll 1$, where $C_{V,0} \sim T^2/v^2$ is the free Dirac fermion specific heat. The full RPA calculation, valid also for large coupling, was carried out by Vafek (2007).

d. Graphene as a quantum critical system

A unified view of the above behavior is presented in Sheehy and Schmalian (2007), where it was stressed that the logarithmic corrections are manifestations of scaling behavior around the quantum critical point at $n = 0$, $T = 0$. As discussed previously, at finite chemical potential, $T = 0$, $n \neq 0$, graphene behaves as a Fermi liquid, whereas, at $T \neq 0$ a quantum critical region fans out of the point $n = 0$, $T = 0$. In the critical region, it is natural to call graphene a Dirac liquid, where the proximity to the Dirac point is important for physical phenomena at finite T. This puts graphene's behavior into the general framework of quantum critical phenomena (Sachdev, 1999). In practical terms, it implies that the logarithmically divergent velocity contributions are cut off by the largest scale: temperature T, $k_F \sim \sqrt{n}$, or magnetic field. Computing physical quantities in perturbation theory (Hartree-Fock or RPA) naturally involves these infrared scales. The separation between the Dirac liquid and Fermi-liquid regimes in the n-T plane is defined by the crossover temperature $T^*(n) = vk_F[1 + (\alpha/4)\ln(\Lambda/k_F)]$, $k_F = \sqrt{\pi n}$, and thus the temperature dependencies quoted previously, are valid for $T_0 > T > T^*(n)$. The ultraviolet temperature scale $T_0 \approx 8 \times 10^4$ K, while for typical graphene densities $n \lesssim 10^{12}$ cm^{-2}, $T^*(n) \sim 10^2$ K.

2. Conductivity

The behavior of the electrical conductivity in graphene has been extensively reviewed (Peres, 2010; Das Sarma *et al.*, 2011). It is believed that charged impurities and resonant scatterers are the main sources of scattering away from the Dirac point, and to an extent the long- or short-range part of the Coulomb potential contributes to scattering is a matter of ongoing debate (Chen *et al.*, 2008; Ponomarenko *et al.*, 2009; Monteverde *et al.*, 2010; Ni *et al.*, 2010; Reed *et al.*, 2010).

Here we only mention effects related to long-range electron-electron interactions near the Dirac point. Interaction corrections to the minimum metallic conductivity of free Dirac fermions $\sigma_0 = e^2/4\hbar = (\pi/2)e^2/h$ (Fradkin,

1986; Lee, 1993) are more involved, because this expression does not contain the quasiparticle velocity, while the electric charge is not renormalized. The debate was fueled in part by electrical measurements of the minimum conductivity (at the Dirac point) which turned out to be somewhat larger than σ_0 (Geim and Novoselov, 2007; Tan *et al.*, 2007). Theoretically, at $T = 0$ (or $T \ll \omega$ where ω is the external frequency), it is expected that any interaction effect should have subleading character, and the frequency can enter only through the running of the coupling $\alpha(\omega)$. Even though some debate still exists (Herbut, Juricic, and Vafek, 2008; Mishchenko, 2008; Sheehy and Schmalian, 2009; Juricic, Vafek, and Herbut, 2010) as to the implementation of the cutoff regularization procedure, the conductivity should have the form

$$\sigma(\omega)/\sigma_0 = 1 + \frac{\tilde{C}\alpha}{1 + (\alpha/4)\ln(\Lambda v/\omega)}, \tag{3.49}$$

where the constant $\tilde{C} \approx 0.01$, as argued by Mishchenko (2008) and Sheehy and Schmalian (2009). The smallness of $\tilde{C}$ reflects the near cancellation of self-energy and vertex corrections, and thus the effect of interactions is small. This value is also consistent with optical measurements on suspended samples (Nair *et al.*, 2008), as well as graphene on a substrate (Li *et al.*, 2008), which find $\sigma(\omega)$ to be very close to σ_0 and frequency independent in a wide range of energies.

In the static limit $\omega = 0$, the presence of disorder, in combination with interactions, can alter the conductivity. For example, for weak gauge field disorder (Δ) where an attractive line of fixed points exists (Fig. 9) with $\alpha^* = (4/\pi)\Delta$, calculations show that the conductivity (on the fixed line) increases relatively to the free limit (Herbut, Juricic, and Vafek, 2008): $\sigma = [\pi/2 + (4 - \pi)\Delta]e^2/h$. For stronger scalar and vector disorder and/or interactions where the couplings run away to infinity the problem is nonperturbative, and a complex variety of behavior is expected (Foster and Aleiner, 2008).

For clean graphene at $\mu = vk_F = 0$ it was pointed out (Fritz *et al.*, 2008; Kashuba, 2008; Müller, Fritz, and Sachdev, 2008) that at high temperature (compared to the frequency) the conductivity is expected to have the form

$$\sigma = \frac{0.76}{\alpha^2}\frac{e^2}{h}, \qquad T\alpha^2 \gg \omega, \tag{3.50}$$

where $\alpha(T) = 4/\ln(\Lambda v/T)$ is the running Coulomb coupling. This form reflects electron-electron inelastic collisions with scattering rate $1/\tau_{ee} \sim \alpha^2 T$. The linear temperature dependence is characteristic for Dirac particles. The above formula is valid as long as $1/\tau_{ee}$ is the dominant scattering mechanism (collision-dominated transport), and implies that clean graphene at the neutrality point should exhibit a universal, interaction-limited conductivity, reflecting essentially the quantum critical behavior of graphene in this regime ($T \gg \mu$). With increased doping (μ/T), a crossover takes place to a Fermi-liquid regime with screened interactions, where $\tau_{ee}^{-1} \sim \alpha^2 T^2/\mu$ (Müller, Fritz, and Sachdev, 2008) and the conductivity is dominated by charged impurity scattering.

It has also been pointed out that for $\mu = 0$ graphene behaves as an almost "perfect" fluid, in a sense that its shear viscosity η relative to the entropy density s is anomalously small: $\eta/s = [0.13/\alpha^2(T)]\hbar/k_B$ (Müller, Schmalian, and Fritz, 2009). This ratio measures how strongly the excitations in a fluid interact. At room temperature η/s of graphene is smaller than η/s of any known correlated quantum fluid, and is close to the lower bound of $(1/4\pi)\hbar/k_B$ proposed to exist for a large class of strongly interacting quantum field theories (Kovtun, Son, and Starinets, 2005). Therefore, due to its quantum critical nature near the Dirac point, graphene is suggested to behave as a strongly correlated quantum liquid and should exhibit signatures of electronic turbulence (Müller, Schmalian, and Fritz, 2009).

E. Overview of main results

Before we proceed with further topics related to interactions in graphene, we broadly summarize the main findings and questions raised so far:

(1) For clean graphene at the neutrality point $\mu = 0$, interactions are not screened and are marginally irrelevant; the fixed point $\alpha^* = 0$ is approached logarithmically (or, equivalently, the quasiparticle velocity increases logarithmically). From a theory standpoint, the approach towards this fixed point is well understood from both weak- and strong-coupling (RPA) perspectives. Since in graphene one can have $\alpha \sim 1$ under rather conventional experimental conditions, our understanding of RPA calculations is important. RPA is justified only in the limit of a large number of fermion species ($N \gg 1$), while for $N = 4$ it should work for weak to moderate coupling; however, there are indications, coming mostly from two-loop calculations, that vertex corrections are numerically small, and thus RPA should work well. Disorder generally drives the system away from the clean fixed point, towards finite or even strong coupling, depending on disorder type.

(2) The resulting behavior near the Dirac point is that of a non-Fermi liquid with a quasiparticle decay rate which is linear in energy, and decreasing quasiparticle residue. All physical characteristics related to the quasiparticle velocity (which increases logarithmically) are affected, and predicted to exhibit systemic, interaction dependent, deviations from their noninteracting values as the Dirac point is approached, as a function of either density or temperature.

(3) Can graphene be driven into an excitonic insulating state? At the Dirac point the long-range Coulomb interactions can lead to bound electron-hole pairs, creating a gap. There has been intense debate whether this can happen under realistic conditions, since the critical interaction strength appears to be $\alpha_c \sim 1$, it seems possible to occur in suspended samples ($\alpha = 2.2$). So far no experimental indications have been observed.

(4) What is the value of the interaction α? Clearly, since $\alpha = 2.2/\epsilon_0$ is dielectric constant dependent, working with different substrates could lead to changes in interaction-dependent effects (Jang *et al.*, 2008). There are also suggestions that graphene has an "intrinsic" value of α (Reed *et al.*, 2010), arising from dynamical dielectric screening. The polarizability

of the Dirac fermions was found to be amplified by excitonic effects, improving screening of interactions between quasiparticles. This analysis leads to values of α ranging from $\alpha \approx 1/7$ in the static limit to $\alpha \approx 2$ at high frequencies. Recent measurements of the cyclotron mass in suspended graphene (Elias *et al.*, 2011) found logarithmic velocity renormalization and extract, within the RPA scheme, an effective value of graphene's dielectric constant $\epsilon_G \approx 3.5$. One can also expect that near the Dirac point, where interactions lead to singular effects, additional factors can be important such as disorder, inhomogeneities, rippling, etc., and thus obscure the clean behavior.

(5) In the Fermi-liquid regime, where interactions are screened, the physics near the Dirac point can still be strongly affected: this is due to resonant features in the quasiparticle self-energy, reflecting interactions of quasiparticles with plasmons.

IV. THE COULOMB PROBLEM AND CHARGED IMPURITIES

The consideration of noninteracting Dirac electrons in 2D under a Coulomb field is of paramount relevance for graphene, and for several reasons. The Coulomb problem for relativistic fermions has many features that are unfamiliar in condensed matter systems, and which resemble long standing predictions made in the context of QED in strong fields. As such, and given that having $\alpha \sim 1$ makes graphene intrinsically strongly coupled, it can provide the first experimental ground for testing many elusive predictions from strong-coupling QED.

On the other hand, the single-particle Coulomb problem constitutes the first step in addressing nontrivial features of the full, many-body interacting problem. Characteristics such as nonlinear screening, or the supercritical instabilities, provide valuable insight in grasping some proposed many-body effects, such as exciton condensation, or spontaneous mass generation in graphene.

Historically, however, the motivation for studying the Coulomb problem comes from the seminal experimental observations (Novoselov *et al.*, 2004) that the field effect in graphene prepared on SiO_2 is characterized by carrier mobilities that do not depend on the Fermi energy or carrier density (the DC conductivity, $\sigma = me|n|$, with $m \simeq$ const), and that carriers are chiral Dirac fermions in 2D (Novoselov, Geim *et al.*, 2005; Zhang *et al.*, 2005). Early semiclassical investigations (Ando, 2006; Nomura and MacDonald, 2006; Adam *et al.*, 2007; Nomura and MacDonald, 2007) showed that such linear-in-density conductivity could be explained by scattering of unscreened Coulomb impurities, which are typically seen in silica in concentrations of $\sim 10^{10}$ cm^{-2} (Ando, Fowler, and Stern, 1982). As a result, transport in the presence of charged impurities rapidly became one of the most studied topics in the quest for the ultimate mobility in graphene. Since, as we saw before, Coulomb's law is exactly preserved in undoped graphene, and approximately preserved for small and moderate doping, the scattering processes are essentially governed by the bare Coulomb problem, unlike conventional metals, where screening is perfect. A thorough understanding of this problem is therefore important not only for its theoretical relevance and its import on electron-electron interactions, but also for its experimental implications, and our understanding of transport in graphene.

Finally, it is highly significant that this is an exactly solvable problem. This means that most quantities can be obtained exactly, allowing us to unveil many interacting and noninteracting effects that are not within reach of the perturbative approaches already discussed. We proceed to show several such features. On account of the long-range nature of the Coulomb field, intervalley processes are not relevant, and hence we solve the problem within each (independent) valley in the Dirac description of fermions in graphene.

A. Exact solution of the Coulomb problem

1. Wave equations and spectrum

A Coulomb center of charge $Z|e|$ generates the potential $U(r) = Ze^2/\epsilon_0 r$ for the electrons. Without any loss of generality, we consider $Z > 0$. The electronic dynamics is governed by the wave equation

$$v\left(-i\boldsymbol{\sigma}\cdot\boldsymbol{\nabla} - \frac{g}{r} + \sigma_3 Mv\right)\Psi(\boldsymbol{r}) = E\Psi(\boldsymbol{r}). \tag{4.1}$$

Here we use $g = Z\alpha = Ze^2/\epsilon_0 v$, with ϵ_0 reflecting the effective dielectric constant of the embedding medium, and the mass M accounts for the more general possibility of a symmetry breaking gap. Throughout this section, we use the scaled energy and mass $\varepsilon = E/v$, $m = Mv$, and $k = \sqrt{\varepsilon^2 - m^2}$. Even though $m = 0$ for ideal graphene without interactions, nonzero m can be induced in many ways. One of them is through interaction with suitable substrates, of which some experimental hints have been reported (Zhou *et al.*, 2007; Grüneis and Vyalikh, 2008; Li, Luican, and Andrei, 2009; Martinazzo, Casolo, and Tantardini, 2010). In terms of the original tight-binding Hamiltonian, the mass M arising from a sublattice symmetry is related to the parameter Δ_0 introduced in Eq. (3.40) via $Mv^2 = \Delta_0$. The axial symmetry of the potential allows us to use the eigenstates of the total pseudo angular momentum, $J_z = L_z + \sigma_z/2$, which is conserved (DiVincenzo and Mele, 1984). We write $\Psi_j^\dagger = r^{-1/2}[F_j(r)\Phi_{j-1/2}(\phi),\ iG_j(r)\Phi_{j+1/2}(\phi)]$, where $j = \pm 1/2, \pm 3/2, \ldots$ are the eigenvalues of J_z, and the cylindrical harmonics read $\Phi_p(\phi) = e^{ip\phi}/\sqrt{2\pi}$. A detailed derivation of the 2D Dirac equation for general radial potentials is given by Novikov (2007a). In our case, Eq. (4.1) reduces to the following radial equations (Khalilov and Ho, 1998; Novikov, D., 2007):

$$[m - \varepsilon - g/r]F_j(r) + [\partial_r + j/r]G_j(r) = 0, \tag{4.2a}$$

$$[\partial_r - j/r]F_j(r) + [m + \varepsilon + g/r]G_j(r) = 0. \tag{4.2b}$$

This coupled pair of first order equations can be straightforwardly reduced to two decoupled second order equations. Free solutions ($g = 0$) of Eq. (4.1) exist when $|\varepsilon| > |m|$, and are simple spherical waves whose k-normalized version reads

$$\Psi_j = \sqrt{\frac{k}{2|\varepsilon|}}\begin{bmatrix} \sqrt{|\varepsilon + m|}J_{j-1/2}(kr)\Phi_{j-1/2} \\ is_\varepsilon\sqrt{|\varepsilon - m|}J_{j+1/2}(kr)\Phi_{j+1/2} \end{bmatrix} \tag{4.3}$$

$[s_x \equiv \mathrm{sgn}(x)]$. For nonzero g, one readily sees from Eq. (4.2) that the solutions at $r \sim 0$ behave as

$$F(r), \qquad G(r) \sim r^{\pm\gamma}, \qquad \gamma = \sqrt{j^2 - g^2}. \tag{4.4}$$

The general exact solution is given in terms of confluent hypergeometric, or Whittaker's functions, in both the massive (Khalilov and Ho, 1998; Novikov, D., 2007; Gupta and Sen, 2008; Pereira, Kotov, and Castro Neto, 2008; Gamayun, Gorbar, and Gusynin, 2009; Gupta, Samsarov, and Sen, 2010) and massless cases (Pereira, Nilsson, and Castro Neto, 2007; Shytov, Katsnelson, and Levitov, 2007b; Gupta and Sen, 2009). In the massless case, one can map Eq. (4.2) into the familiar Coulomb radial Schrödinger equation in 3D (Pereira, Nilsson, and Castro Neto, 2007)

$$\partial_r^2 f_\pm + [\varepsilon^2 + 2g\varepsilon/r - \gamma(\gamma \mp 1)/r^2] f_\pm(r) = 0, \tag{4.5}$$

where $f_\pm$ are linear combinations of F and G, ε^2 takes the place of the Schrodinger energy, and γ plays the role of angular momentum. Since the solution is formally the same, the appearance of ε^2 instead of ε means that the massless case admits no bound solutions, as we expect on account of the absence of a spectral (mass) gap. The massive case, however, has a well-defined infinite spectrum of bound solutions when $|\varepsilon| < |m|$, given by (Khalilov and Ho, 1998)

$$\varepsilon_{n,j} = s_g m \frac{n + \sqrt{j^2 - g^2}}{\sqrt{g^2 + [n + \sqrt{j^2 - g^2}]^2}}, \tag{4.6}$$

lowest level is given by $\varepsilon_G \equiv \varepsilon_{0,1/2} = s_g m\sqrt{1 - (2g)^2}$.

2. Supercritical instabilities

Consideration of Eq. (4.4) immediately reveals a complication if $g > g_c = 1/2$, because γ becomes imaginary for the lowest angular momentum channels ($j = \pm 1/2$). The solution (4.4) is neither regular nor divergent, but rather oscillates endlessly towards $r = 0$. This is pathological because the space of solutions is of dimension 2, and we can no longer discard an irregular contribution since both linearly independent solutions are square integrable. In other words, there is no boundary condition at the origin to univocally select the solution. In the massive case the level ε_G becomes imaginary, signaling a loss of self-adjointness of the Dirac Hamiltonian for $g > 1/2$.

Physically, both effects are a symptom that the potential has such a strong divergence that particles are inexorably attracted and "fall" into the origin, leading to a collapse of the system (for example, the endless oscillations can be read as an infinite phase shift). This "fall to the center" is a general characteristic of diverging potentials in any dimension of space. For power law potentials, one particular power signals the threshold of criticality. The Coulomb potential is the marginal case for the Dirac equation (in both 2D and 3D), just as the potential $1/r^2$ is the marginal case of the 3D Schrodinger equation (Landau and Lifshitz, 1981). This, of course, begs the question of regularization. Regularizing the potential introduces an additional boundary condition at some short distance R, which allows a formal solution, and cures the total collapse of the system (Case, 1950; Perelomov and Popov, 1970). In graphene, the lattice is the natural regulator and there are no ultraviolet issues. But the physics in the supercritical regime depends explicitly on the short-range details.

This supercritical collapse has a long history in the context of QED, where the Dirac equation stands as the basis for understanding the stability of matter. In QED, the collapse would occur for $Z\alpha_{\mathrm{QED}} > 1$, which leads to extensive investigations regarding the stability of heavy nuclei having $Z > Z_c = 137$ (Case, 1950; Popov, 1971a; Popov, 1971b; Zeldovich and Popov, 1972; Greiner *et al.*, 1985). After regularization $Z_c \to 170$, which makes the problem highly academic, and QED's predictions untestable. In graphene, on the contrary, $Z_c \sim 1$, which opens the real possibility of testing the supercritical instability in a condensed matter setting.

a. Massive electrons

To understand the physics in the supercritical regime, we can follow the level ε_G as the coupling increases (see Fig. 18) (Zeldovich and Popov, 1972; Greiner *et al.*, 1985; Pereira, Kotov, and Castro Neto, 2008). For the pure Coulomb case, $\varepsilon_G(g)$ decreases towards zero in a singular way at $g = g_c$. In a regularized potential, ε_G depends also on the cut-off radius R, and is allowed to monotonically penetrate the negative energy region, until eventually touching the lower continuum at $\varepsilon = -m$. If g is further increased, ε_G dives into the hole (positron) continuum and becomes a resonance. Other levels will sequentially follow at higher g. The diving point for $\varepsilon_G(g)$ defines a renormalized critical coupling $\tilde{g}_c > g_c$ that is characterized by a logarithmic singularity at $mR \sim 0$: $\tilde{g}_c \simeq g_c + \pi^2/\log^2(mR)$ (Khalilov and Ho, 1998; Pereira, Kotov, and Castro Neto, 2008; Gamayun, Gorbar, and Gusynin, 2009; Zhu *et al.*, 2009), strongly depending on the regularization.

This diving of bound levels entails a complete restructuring of the vacuum. If the level was empty, an electron-hole pair will be immediately created: the electron remains tightly bound and shielding the center, while the hole is ejected to infinity (Zeldovich and Popov, 1972; Greiner *et al.*, 1985). The supercritical regime is thus characterized by spontaneous pair creation, or a spontaneous Schwinger mechanism (Schwinger, 1951). One expected consequence is a strong

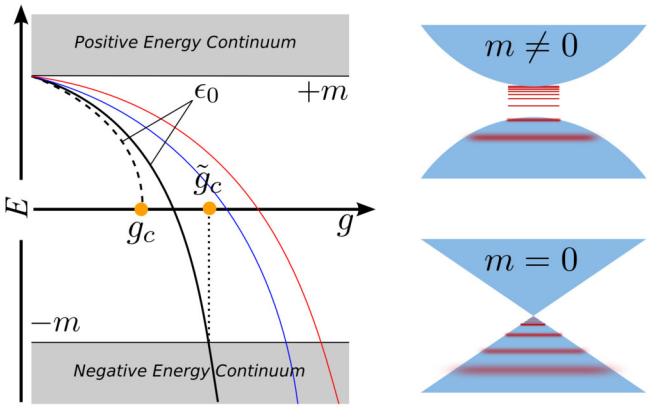

FIG. 18 (color online). Schematic drawing of the level diving process in the supercritical regime and of the resulting quasispectrum of levels for massive and massless fermions.

signature of these resonances in the hole sector of the scattering and transport cross sections.

An essential detail is that these resonances are not usual bound levels diluted inside a continuum, where their lifetime essentially disappears. One consequence of the chiral nature of Dirac fermions, combined with the long-range tail of the Coulomb potential, is that the supercritical levels in the relativistic Coulomb remain sharply defined, with diverging lifetime. For example, for S states ($j = 1/2$), one shows that these resonances follow (Gamayun, Gorbar, and Gusynin, 2009)

$$\varepsilon_n \approx -m\left(1 + \xi + i\frac{3\pi}{8}e^{-\pi/\sqrt{2\xi}}\right), \qquad \xi = \frac{3\pi(\beta - \beta_c)}{8\beta\beta_c}, \tag{4.7}$$

when $g \gtrsim \tilde{g}_c$, and where $\beta = i\gamma$, $\beta_c = \sqrt{\tilde{g}_c^2 - 1/4}$. In real space the localization of the supercritical levels is controlled by the reduced Compton wavelength: $\lambda_C = 1/mv$. The modulus squared of their wave function decays as $\Psi^\dagger\Psi \propto \exp(-\sqrt{8gr/\lambda_C})$ and, consequently, even inside the continuum such levels retain a highly localized nature, which is why they are so relevant, in particular, in their potential for screening (Pereira, Kotov, and Castro Neto, 2008).

b. Massless electrons

The spectrum in this case is continuous everywhere, and thus there is no sequential diving and restructuring of the hole continuum as described above. But the pathology associated with Eq. (4.4) still exists. Physically, the massless situation is rather more catastrophic since the solution in a regularized potential reveals an infinite number of quasilocalized resonances in the hole sector (Pereira, Nilsson, and Castro Neto, 2007; Shytov, Katsnelson, and Levitov, 2007b; Gamayun, Gorbar, and Gusynin, 2009). This is a highly nontrivial effect for several reasons: (i) in the massless case there is no natural length scale in the problem to characterize such localized states; (ii) the system abruptly develops an infinite quasibound spectrum at $g > g_c$, when its spectral fingerprint is rather featureless for $g < g_c$; and (iii) the infinite spectrum has the potential to over screen the Coulomb center. In addition, unlike the massive case, here the critical coupling remains unchanged at $g_c = 1/2$, and no qualitative features (such as how many, if any, states have dived) depend on the magnitude of the regularization distance. The spectrum of supercritical resonances behaves as (Shytov, Katsnelson, and Levitov, 2007b; Gamayun, Gorbar, and Gusynin, 2009; Gupta and Sen, 2009)

$$\varepsilon_n \approx -\frac{a + ib}{R}e^{-\pi n/\sqrt{g^2 - g_c^2}}, \qquad (a, b) \sim \mathcal{O}(g), \tag{4.8}$$

which has an essential singularity at g_c, an energy scale and/or lower bound set explicitly by the regularization distance R and diverging lifetimes close to the critical point. Since the width of these states vanishes linearly, they are practically bound states (hence the designation quasibound states). In real space, the localization scale is determined by the regularization distance R itself.

Since mesoscopic and nanoscopic devices are of high interest, it is pertinent pointing out that *massless* Dirac fermions in a finite-sized system mimic in all aspects the physics of *massive* electrons, as a result of the linearly vanishing DOS and the effective gap coming from finite-size quantization (Pereira, Kotov, and Castro Neto, 2008).

3. DOS, scattering, and transport cross sections

Here and in the following sections, we are concerned mostly with massless Dirac fermions, except when explicitly stated otherwise. The local density of states (LDOS) and cross sections are useful quantities insofar as they are directly accessible in local probe and transport experiments. The LDOS per unit area and spin is isotropic, and can be written in closed form in terms of partial waves as $N(\varepsilon, r) = \sum_j n_j(\varepsilon, r)$, (Pereira, Nilsson, and Castro Neto, 2007) with

$$n_j(\varepsilon, r) = \frac{j^2}{2\pi^2\gamma^2 r}\left[F_{\gamma-1}^2 + F_\gamma^2 + \frac{2gs_\varepsilon}{|j|}F_\gamma F_{\gamma-1}\right] \tag{4.9}$$

for $g < g_c$, and F_l represents the Coulomb function $F_l(-gs_\varepsilon, |\varepsilon|r)$ (Abramowitz and Stegun, 1964). The function $N(\varepsilon, r)$ is plotted in Fig. 19(a) for different couplings and distances. Apart from the evident particle-hole asymmetry, the LDOS remains rather featureless, even at the shortest distances. If $g > g_c$, the corresponding analytical expression obtained in the regularized potential is more complex, but still has a closed form (Pereira, Nilsson, and Castro Neto, 2007). In this case, supercritical channels ($|j| < 1/2$) need to be isolated from undercritical ones ($|j| > 1/2$), yielding two contributions to the LDOS:

$$N(\varepsilon, r) = \sum_{|j|<|g|}\bar{n}_j(\varepsilon, r) + \sum_{|j|>|g|}n_j(\varepsilon, r). \tag{4.10}$$

The total LDOS for this case is shown in Fig. 19(c) for $g = 1.0$, and at different distances to the impurity. It is now clear that strong resonances, decaying rapidly with distance, appear in the vicinity of the Dirac point, signaling the presence of the quasibound levels (Pereira, Nilsson, and Castro Neto, 2007; Shytov, Katsnelson, and Levitov, 2007b). Their exponential accumulation at $\varepsilon = 0$ is confirmed in Fig. 19(d) where we show the supercritical contribution $\bar{n}_j(\varepsilon, r)$ as a function of $\log(|\varepsilon|)$. At positive energies, the LDOS exhibits periodically decaying oscillations in εr [inset of Fig. 19(c)], with extrema separated by $\approx n\pi$, within logarithmic accuracy (Shytov, Katsnelson, and Levitov, 2007a). When directly measured in STM, such oscillations can be used to extract the electronic dispersion, as done by Ouyang, Huang, and Lieber (2002).

We point out that, since the solution of the supercritical problem involves a nontrivial *ad hoc* regularization, these results have been checked numerically against exact solution of the full tight-binding problem in the honeycomb lattice, being found that the analytical Dirac results reproduce the full lattice problem down to distances as small as the lattice scale (Pereira, Nilsson, and Castro Neto, 2007).

The striking differences between the two regimes and the violent modification of the ground state at strong coupling are likewise evident in the behavior of the scattering phase shifts

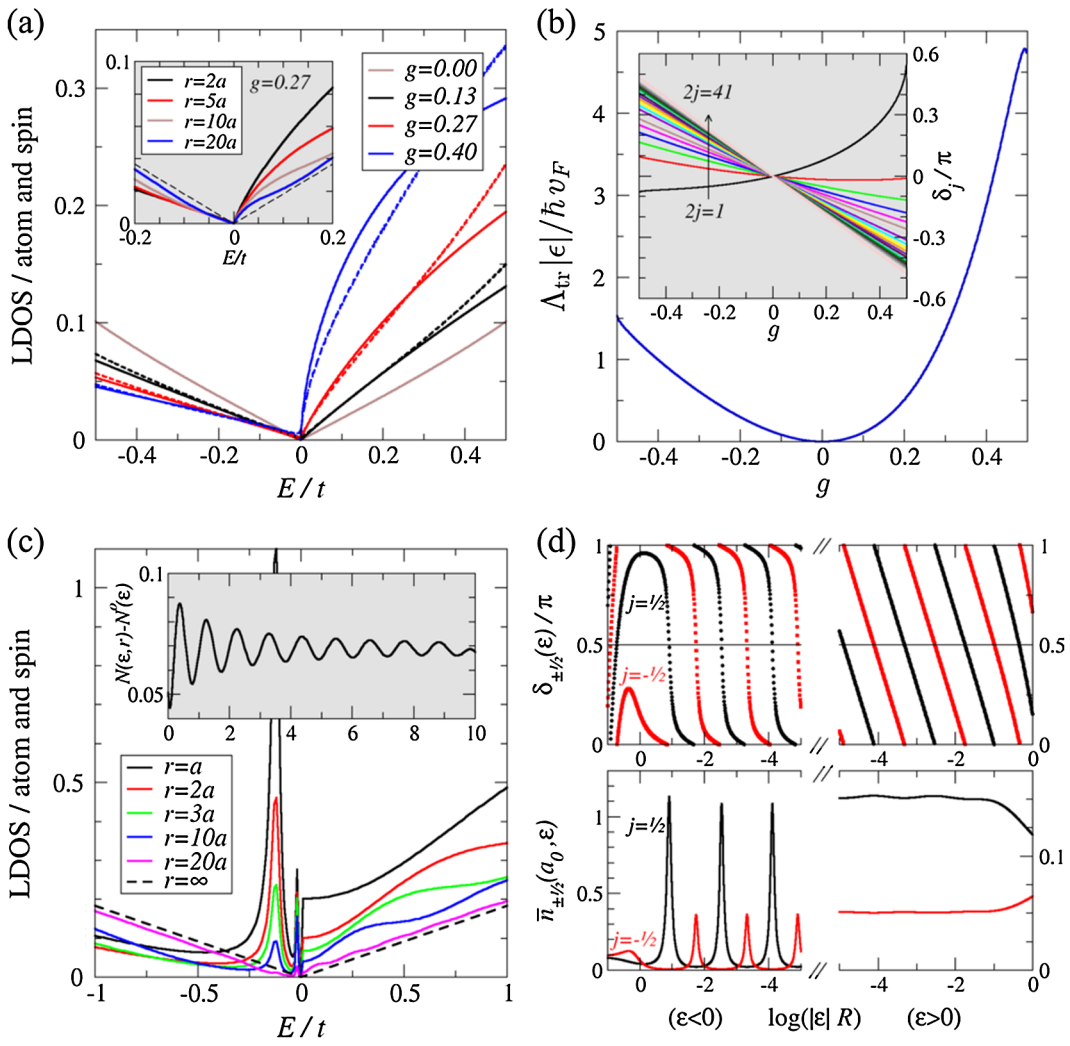

FIG. 19 (color online). (a) LDOS, $N(\varepsilon, r)$ at $r = a$ for several couplings $g < g_c$. The inset shows $N(\varepsilon, r)$ for $g = 0.27$ and different r. For comparison, the exact LDOS calculated in the full tight-binding lattice for the same parameters is shown as dashed lines. In the horizontal axis the energy is in units of the hopping t. (b) The weak-coupling transport cross section as a function of g. The inset shows the phase shifts for different j. (c) LDOS, $N(\varepsilon, r)$ at several distances r, for $g = 1 > g_c$. The inset shows the oscillating LDOS correction for $\varepsilon > 0$. (d) Energy dependence of the phase shifts (top) and the supercritical contribution $\bar{n}_j(\varepsilon, r)$ to the LDOS (bottom) for $g = 1.0$.

$\delta_j(\varepsilon)$. They admit closed formed expressions at both $g < g_c$ (Novikov, 2007a; Pereira, Nilsson, and Castro Neto, 2007; Shytov, Katsnelson, and Levitov, 2007a) and $g > g_c$ (Shytov, Katsnelson, and Levitov, 2007b; Castro Neto *et al.*, 2009b). For example, the undercritical S matrix reads (Novikov, D., 2007)

$$S_j(\varepsilon) = e^{2i\delta_j(\varepsilon)} = \frac{je^{i\pi(j-\gamma)}}{\gamma - igs_\varepsilon} \frac{\Gamma(1+\gamma-igs_\varepsilon)}{\Gamma(1+\gamma+igs_\varepsilon)}, \qquad (4.11)$$

which is energy independent, but considerably asymmetric with respect to the sign of g. The corresponding δ_j are shown in Fig. 19(b) (inset) as a function of coupling strength. Note how $\delta_{1/2}$ (the most important partial wave) behaves rather differently from the others: only $\delta_{1/2}$ shows the expected sign for the attractive and/or repulsive situations. On the other hand, in the supercritical regime there is a strong ε dependence of δ_j. In the top row of Fig. 19(d), we present $\delta_j \bmod \pi$ as a function of $\log(\varepsilon)$. In the attractive sector ($\varepsilon < 0$ if $g > 0$) the abrupt steps centered around $\pi/2$ mark the position of the infinite quasibound spectrum [which, as per Eq. (4.8), accumulates exponentially at $\varepsilon = 0$], whereas in the attractive sector $\delta_j(\varepsilon)$ is smooth.

Knowledge of the phase shifts allows direct calculation of the full transport cross sections for our 2D Dirac fermions,

$$\Lambda_{\rm tr}(\varepsilon) = \frac{2}{\varepsilon}\sum_j \sin^2[\delta_{j+1/2}(\varepsilon) - \delta_{j-1/2}(\varepsilon)] \qquad (4.12)$$

(Katsnelson, 2006; Novikov, D., 2007). The profile of $\Lambda_{\rm tr} \times \varepsilon$ at weak coupling is shown in Fig. 19(b). When scattering is due only to unscreened charges, the marked asymmetry between $g > 0$ and $g < 0$ can be used to extract the density of positively and negatively charged impurities ($n_i^{\pm}$) from a single measurement of the electrical conductivity σ as a function of carrier density (Novikov, D. S., 2007). This technique has been used in some experiments (Chen *et al.*, 2008; 2009; Chen, Xia, and Tao, 2009), but the asymmetry effect can be easily masked by other spurious influences (Huard *et al.*, 2008; Barraza-Lopez *et al.*, 2010; Nouchi

and Tanigaki, 2010). Moreover, on account of the ε independence of δ_j in Eq. (4.11), the corresponding Drude conductivity $\sigma = 4\pi e^2\mu/\upsilon n_i \Lambda_{\rm tr} h^2$ is immediately seen to scale linearly with density: $\sigma \propto \mu^2 \propto n$. Therefore, the linear-in-density conductivity, which appears already in the first Born approximation, remains when the cross section is calculated exactly.

For supercritical potentials, and similarly to the LDOS, there will be undercritical and supercritical partial waves contributing to $\Lambda_{\rm tr}(\varepsilon)$ [cf. Eq. (4.10)]. The latter give rise to strong peaks in the transport cross section at densities for which the Fermi energy matches the levels ε_n (Shytov, Katsnelson, and Levitov, 2007b), tallying with the behavior of the DOS.

B. Induced charge and screening

First attempts at understanding screening in graphene date back to DiVincenzo and Mele (1984), where it was recognized that conventional procedures of the theory of metals, such as self-consistent screening, linear response, or Friedel sum rules, are not straightforward in this system. For example, within the Dirac (effective mass) approximation, the ultraviolet cutoff scale enters explicitly in Friedel's sum rule, and Levinson's theorem is modified (Lin, 2006). [Levinson's theorem is one of the fundamental results in quantum scattering theory, asserting that in Schrödinger's equation with a nonsingular spherically symmetric potential the zero energy scattering phase shift exactly counts the number of bound states: $\delta_l(0) = N_l\pi$.] One consequence is that a naive application of Friedel's sum rule can yield divergent displaced charges (DiVincenzo and Mele, 1984). Even though these divergences are artificial in the target lattice problem, they point, already at a single-particle level, to the anomalous screening properties of graphene.

1. Weak Coupling ($g < g_c$)

a. Noninteracting induced charge

Knowledge of the exact LDOS within the Dirac approximation (Sec. IV.A.3) allows the straightforward calculation of the perturbation to the electronic density induced by the Coulomb center. The induced density is defined as $\delta n(\boldsymbol{r}) = n(\boldsymbol{r}) - n^0(\boldsymbol{r})$, and is related to the LDOS via (for undoped graphene at zero temperature) $n(\boldsymbol{r}) = \sum_j n_j(r) = \sum_j \int_{-D}^{0} n_j(\varepsilon, r)d\varepsilon$, where D is the cutoff scale for the linearly dispersing band. The induced charge density is just $\delta\rho(\boldsymbol{r}) = -|e|\delta n(\boldsymbol{r})$. Closed form expressions for $n_j(r)$ are provided in Eq. (4.9). One difficulty with this approach is that the resulting density per partial wave behaves asymptotically as

$$\delta n_j(r \to \infty) \sim \frac{1}{r}\left[D - \frac{g}{r} - D^0 + \mathcal{O}(r^{-2})\right], \tag{4.13}$$

which diverges upon summation over j (a reminiscence of the problems associated with the ultraviolet scale alluded to above). In the above expression, D and D^0 represent the cutoff in the presence and in the absence of the Coulomb center, respectively. Since the subleading terms in Eq. (4.13) are convergent in j, we regularize it by taking a position dependent cutoff: $D \to D^0 + g/r$. As a result, the total induced density acquires the form $\delta n(r) \sim H(D^0 r)/r^3$, where $H(x)$ is a constant-amplitude oscillating function (Pereira, Nilsson, and Castro Neto, 2007). Since it is desirable to have control over the validity of the regularization procedure outlined above, we have calculated the total induced density $\delta n(\boldsymbol{r})$ in the full tight-binding problem, via exact diagonalization. The result is plotted in Fig. 20(a), and unequivocally shows the predicted $1/r^3$ decay, with oscillations on the scale of the lattice. Such fast decay implies that the induced charge concentrates within a small vicinity of the impurity. Moreover, the numerical results in the lattice further suggest that such distance is of the order of the lattice parameter a: the inset in Fig. 20(a) reveals that the total charge pulled inside a region $r < R_{\rm max}$ saturates within very few lattice spacings. In fact, since $D^0 \propto 1/a$, in the limit $a \to 0$ (where the effective mass description is meaningful) the analytical expression $\delta n(r) \sim H(D^0 r)/r^3$ can be seen as a representation of the 2D Dirac delta function. In other words, we expect the induced charge density to behave as

$$\delta\rho(\boldsymbol{r}) = -|e|\delta n(\boldsymbol{r}) \overset{a\to 0}{\to} -Q|e|\delta(\boldsymbol{r}). \tag{4.14}$$

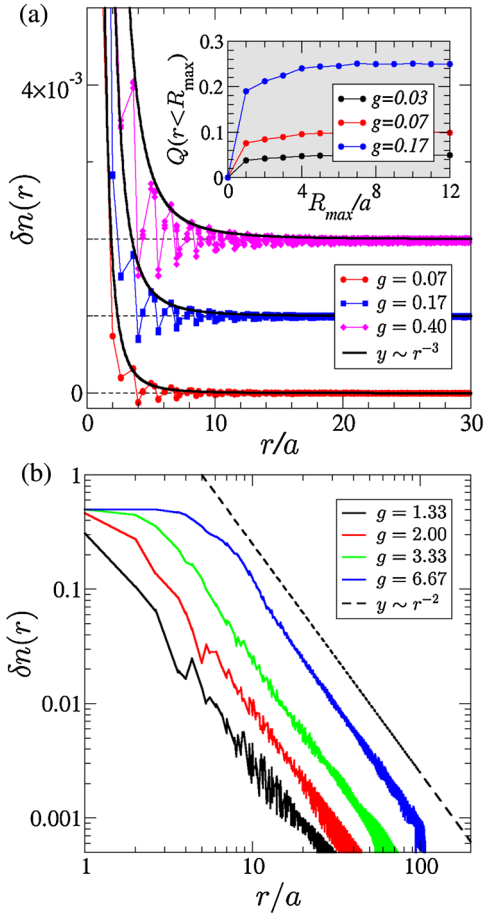

FIG. 20 (color online). (a) Induced electron density $\delta n(\boldsymbol{r})$ plotted as a function of distance to the Coulomb center, for different impurity strengths, $g < g_c$. Data obtained from full diagonalization of the tight-binding Hamiltonian in a lattice with 124^2 atoms. The black lines are $\propto 1/r^3$ and guides for the eye. The inset shows the saturation of the integrated charge accumulated inside $r < R_{\rm max}$, as a function of $R_{\rm max}$. (b) Same as (a), but for the supercritical case, $g > g_c$, and the dashed line is now $\propto 1/r^2$.

The same conclusion follows from a modified Friedel argument (Shytov, Katsnelson, and Levitov, 2007a), and from the exact calculation of the noninteracting Green's function in the Coulomb field (see below) (Terekhov *et al.*, 2008). The induced charge has a screening sign, as expected, but the strongly localized distribution of the induced charge (4.14) implies that undoped graphene cannot screen in the usual sense, because it merely renormalizes the strength of the impurity: $Z \to Z_{\rm eff} = Z - Q$. This leaves Coulomb's law unaltered, except for the substitution $Z \to Z_{\rm eff}$.

b. Linear (RPA) screening

Single-particle results, such as the one above, are not generally sufficient to draw conclusions about screening. Consider now the same problem in linear response, at the RPA level, which is justified for small, undercritical couplings. Within the RPA, the Fourier transform of the statically screened potential is given by $U_s(q) = U_0(q)/[1 - \Pi^{(1)}(q)V(q)]$ (Fetter and Walecka, 1971), where $V(q) = 2\pi e^2/\epsilon_0 q$ is the electron-electron interaction and $U_0(q) = ZV(q)$ the external impurity potential. From Eq. (2.14), we know that $\Pi^{(1)}(q \to 0) \approx -q/4v$, and hence

$$U_s(q) \approx U_0(q)\left(1 + \frac{\pi}{2}\alpha\right)^{-1} = \frac{U_0(q)}{\epsilon_{\rm RPA}}. \tag{4.15}$$

Therefore, linear response confirms the absence of screening, except for the trivial renormalization of the static dielectric constant: $\epsilon_0 \to \epsilon_{\rm RPA} = \epsilon_0(1 + \pi\alpha/2)$ (Ando, 2006). Likewise, the induced density can be computed in linear response from $\delta n(\boldsymbol{q}) = -ZV(\boldsymbol{q})\Pi(\boldsymbol{q})$ or in the RPA

$$\delta n(\boldsymbol{r}) = -Z\int d\boldsymbol{q}\,\frac{\Pi^{(1)}(\boldsymbol{q})V(\boldsymbol{q})}{1 - \Pi^{(1)}(\boldsymbol{q})V(\boldsymbol{q})}e^{i\boldsymbol{q}\cdot\boldsymbol{r}}, \tag{4.16}$$

yielding $\delta\rho(r \gg a) \sim -\delta(\boldsymbol{r})Z|e|\pi\alpha/2$ to linear order in α (Kolezhuk *et al.*, 2006). This is exactly what was obtained in Eq. (4.14) from a single-particle, wave function perspective. In addition, the argument that the Fourier transform of $\delta n(\boldsymbol{r})$ is dimensionless can be used to show that it should be a pure constant in undoped graphene, for which there is no natural length scale. As a result, $\delta\rho(\boldsymbol{r}) \propto \delta(\boldsymbol{r})$ remains true in all orders of perturbation theory (Biswas, Sachdev, and Son, 2007). For consistency, the total induced charge Q introduced in Eq, (4.14) is then given by

$$Q = \frac{\pi}{2}Z\alpha + (\text{higher orders in } Z\alpha). \tag{4.17}$$

To verify this correspondence, we can compare Eq. (4.17) with the value of Q extracted from the noninteracting exact diagonalization in the honeycomb lattice. As shown in Fig. 21(a), the numerical Q for different values of Z follows Eq (4.17) for most of the range $0 < g < g_c$, thereby confirming the correspondence, and showing how weakly undoped graphene screens (Pereira, Nilsson, and Castro Neto, 2007; Shytov, Katsnelson, and Levitov, 2007a). Given that only the global dielectric constant is affected, one can say that undoped graphene screens as an insulator.

At finite densities, however, the system screens as a conventional metal. This derives at once from the fact that, at finite Fermi momentum, $\Pi^{(1)}(q \approx 0) \approx -2k_F/\pi v$, no longer vanishing, and leading to the screened potential

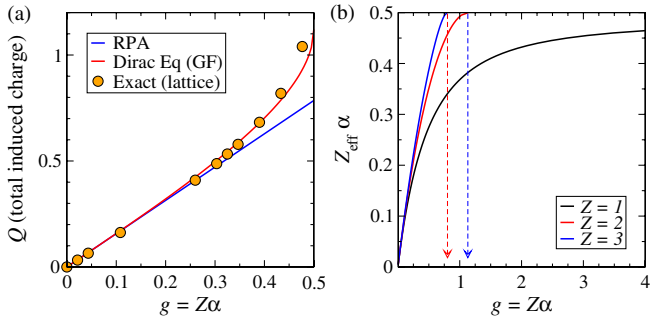

FIG. 21 (color online). (a) Total integrated charge in the vicinity of the impurity Q obtained from exact diagonalization in the lattice (dots), from RPA (4.16), and from the exact Green's function in the Coulomb field (4.19). (b) The self-consistent $Z_{\rm eff}$, obtained from Eq. (4.21) (Terekhov *et al.*, 2008). Numerical data (dots) are plotted after accounting for finite-size renormalization of g_c (Pereira, Kotov, and Castro Neto, 2008).

$$U_s(q) = \frac{U_0(q)}{\epsilon_{\rm RPA}(q)}, \qquad \epsilon_{\rm RPA}(q) = 1 + \frac{q_s}{q}, \tag{4.18}$$

$q_s = 4\alpha k_F$ playing here the role of inverse screening length (Ando, 2006; Nomura and MacDonald, 2006). Contributions from interband transitions can be simply incorporated by renormalizing the background dielectric constant by the factor $1 + \pi\alpha/2$, as in Eq. (4.15). Using Eq. (4.16), the total integrated charge is now seen to be $\int \delta\rho(\boldsymbol{r})d\boldsymbol{r} = -Z|e|$. This means that, unlike the undoped situation, at finite electron densities the system completely screens the Coulomb center, just as expected in a metallic system (Castro Neto *et al.*, 2009b).

For transport considerations, it is important to underline that, even though at finite densities charged impurities have a finite range determined by q_s, the Boltzmann conductivity remains linear in density. This happens because the screened potential (4.18) entering in the relaxation time calculation maintains the same dependence with k_F. From this perspective, the mobility remains constant in density for both screened and unscreened charges, differing only by an overall constant related to $\epsilon_{\rm RPA}(k_F)$ (Nomura and MacDonald, 2006).

c. Nonlinear screening

As Fig. 21(a) documents, even as linear response is acceptable at small values of $g = Z\alpha$, the approximation becomes increasingly unwarranted as g nears the critical threshold, $g_c = 1/2$, which is nonperturbative. Rather than analyze this limit on the basis of exact wave functions in the Coulomb field, as done in Sec. IV.B.1.a, we now describe the solution obtained by Terekhov *et al.* (2008). They bypass the solution of the Dirac equation, obtaining instead an exact integral expression for the Green's function in a Coulomb field, using a proper-time approach common in QED (Mil'shtein and Strakhovenko, 1982). The main result is that

$$\delta\rho(\boldsymbol{r}) = -Q\delta(\boldsymbol{r}) + \delta\rho_{\rm dist}, \tag{4.19}$$

where $\delta\rho_{\rm dist}(\boldsymbol{r})$ represents a positive charge distributed at $r = \infty$ (needed to satisfy the constraint of total zero induced charge). It is significant that this approach affords an exact expression for the dependence of Q upon $g = Z\alpha$, which is

shown in Fig. 21(a). A series expansion of this dependence yields the following:

$$Q(g) \approx \frac{\pi}{2} g + 0.783 g^3 + 1.398 g^5 + \cdots, \tag{4.20}$$

with each term corresponding to successive orders in perturbation theory. The linear term is the one that appeared already in Eq. (4.17) at the RPA level. The next term in the expansion was also calculated perturbatively by Biswas, Sachdev, and Son (2007). Interestingly, even though this problem is analogous to conventional QED vacuum polarization of a point charge, the perturbative coefficients in $Q(g)$ are not small, and increase with order, in stark opposition with the behavior known in 3D QED (Brown, Cahn, and McLerran, 1975). This offers another perspective upon the uniqueness of electron-electron interactions in graphene, for, even though the problem is on the surface analogous to the QED situation, the physics can be qualitatively different. In this particular case, the difference seems to arise from the 2D dimensionality of the problem and the absence of Lorentz invariance in graphene, which renders the Coulomb interactions instantaneous.

Inspection of the curve $Q(g)$ in Fig. 21(a) reveals that it reaches 1 at $g = 0.49$, slightly before g_c. This implies that, for a monovalent impurity ($Z = 1$), the noninteracting result predicts complete shielding before g_c, insofar as $Z_{\rm eff}(Z, \alpha) = Z - Q(g) \to 0$. Such strong renormalization of the potential source immediately begs the consideration of interaction and correlation effects. They can be incorporated at the Hartree level by solving the self-consistent equation

$$Z_{\rm eff}\alpha = Z\alpha - \alpha Q(Z_{\rm eff}\alpha), \tag{4.21}$$

which encodes an infinite summation of a selected set of bubble diagrams (Terekhov *et al.*, 2008). Since $Q(g)$ is obtained exactly, one obtains the renormalized effective potential strength $Z_{\rm eff}\alpha$ with an accuracy much beyond the RPA. In addition, the reduction of $Z_{\rm eff}$ with respect to the bare Z means that g_c is also self-consistently renormalized to $\tilde{g}_c = Z_{\rm eff}\alpha$. The effect is shown in Fig. 21(b), which reveals that, as $\tilde{g}_c > g_c$, self-consistent screening delays the supercritical threshold because the condition $Z_{\rm eff}\alpha = 0.5$ requires a higher bare Z. This phenomenon is most striking for $Z = 1$, in which case the supercritical point disappears altogether ($\tilde{g}_c < 1/2$ even as $Z \to \infty$), whereas $g_c^{Z=2} = 1.136$ and $g_c^{Z=3} = 0.798$. The prediction of this self-consistent Hartree renormalization of $Z_{\rm eff}$ is that impurities with $Z = 1$ can never become supercritical. In addition, Hartree screening is sufficient to suppress the tendency for overshielding of the Coulomb center [as seen in the inset of Fig. 21(b), $Z_{\rm eff}$ remains always positive].

An alternative approach to the Hartree screening consists in treating the induced charge in linear response $\delta\rho(\boldsymbol{q}) = ZV(\boldsymbol{q})\Pi(\boldsymbol{q})$ but taking into account electron-electron interactions perturbatively, via the renormalization of the coupling constant (Biswas, Sachdev, and Son, 2007). This is valid for small α (weak interaction), and leads to a result formally equivalent to Eq. (4.19), but where $\delta\rho_{\rm dist}$ now arises from the electronic correlations. The distributed charge in the interacting case also has an antiscreening sign, but decays as $1/r^2$, while the noninteracting $\delta\rho_{\rm dist}(\boldsymbol{r})$ is zero everywhere, except at infinity.

Even though the above considerations pertain to undoped graphene, since all screening charge accumulates completely within a narrow distance, finite densities are not expected to alter the picture as long as $q_s = 4\alpha k_F$ remains large compared to the lattice scale a.

2. Strong coupling ($g > g_c$)

In Sec. IV.B.1.c, Hartree screening was shown to renormalize g_c and delay the critical threshold. Two important questions naturally arise: (i) Since the self-consistent solution of Eq. (4.21) is uncontrolled, how certain can one be that the critical regime is reachable at all? (ii) So far, we have looked only at screening from the undercritical side (i.e., as long as $Z_{\rm eff}\alpha < 1/2$). How can one address screening from the supercritical side, given that this regime cannot be reached perturbatively?

The answer to these questions is far from trivial. In QED it is related to the ground state and stability of superheavy nuclei ($Z \gtrsim 170$), when the bound spectrum dives into the positron continuum (see Fig. 18). Despite having received considerable attention throughout the 1970–1980's (Greiner *et al.*, 1985), the fact that these systems require such high Z's has turned it largely into an academic problem. The exciting prospect about graphene is that impurities with $Z = 1$, 2 might already display supercritical physics, in which case it would afford a bench-top test of some yet untested QED predictions.

The essence of the difficulties in treating the supercritical regime clearly lies in its nonperturbative nature. Graphene, being gapless, is even more pathological because of the infinite quasispectrum that appears in the hole channel (see Fig. 18). This quasispectrum is akin to an atom filled with infinitely many electrons and, as known from studies of heavy atoms (Landau and Lifshitz, 1981), it requires full consideration of correlations and interactions, and self-consistent techniques such as the Thomas-Fermi method (Fermi, 1927; Thomas, 1927).

a. Noninteracting induced charge

In Sec. IV.A.3, we saw some unusual consequences for the DOS and cross sections extracted from the exact solution of the Dirac equation for $g > g_c$. Now we address the corresponding induced charge obtained using the same procedure as in Sec. IV.B.1.a. Consideration of the exact wave functions (Pereira, Nilsson, and Castro Neto, 2007) or the exact phase shifts (Shytov, Katsnelson, and Levitov, 2007a) leads to the conclusion that the supercritical partial waves contribute with an induced charge $\propto 1/r^2$. This could be expected on dimensional grounds: $\delta(\boldsymbol{r})$ and $1/r^2$ are the only dimensionally consistent possibilities in the absence of any intrinsic length scale in massless graphene. The exact induced density per partial wave reads (Shytov, Katsnelson, and Levitov, 2007a)

$$\delta\bar{n}_j(\boldsymbol{r}) = \frac{2s_g}{\pi^2 r^2}\sqrt{g^2 - j^2}, \tag{4.22}$$

and, like the undercritical contributions, has a screening sign. The full induced charge is obtained from $\delta\rho(\boldsymbol{r}) = -|e|\delta n(\boldsymbol{r})$, $n(\boldsymbol{r}) = \sum_{|j|<g_c}\delta\bar{n}_j + \sum_{|j|>g_c}\delta n_j$, and has the general form

$$\delta n(\boldsymbol{r}) = s_g A \frac{1}{r^2} + B s_g \delta(\boldsymbol{r}). \tag{4.23}$$

If $1/2 < g < 3/2$, Eq. (4.23) reduces to $\delta n(\boldsymbol{r}) = (\pi g/2)\delta(\boldsymbol{r}) + 2s_g\sqrt{g^2 - g_c^2}/\pi^2 r^2$. The general behavior (4.23) is also confirmed numerically by exact diagonalization of the tight-binding Hamiltonian in the honeycomb lattice, whose results are plotted in Fig. 20(b).

b. Supercritical protection

Unlike the undercritical regime, the additional power law decay in Eq. (4.23) causes a modification of Coulomb's law at large distances. But since we have a quasiatom with all levels (4.8) filled, the noninteracting result in Eq. (4.23) cannot be the final answer. Each level is quasilocalized on the lattice scale, and should contribute significantly to shield the Coulomb center. For g, not too much above g_c we can follow an argument advanced by Shytov, Katsnelson, and Levitov (2007a) that assumes electrons at some distance r feel the effect of a point charge consisting of the impurity subtracted from all the accumulated screening charge up to r. In other words, we introduce a distance dependent impurity strength $Z_{\rm eff}(r) = Z - \int_R^r \delta n(\boldsymbol{r}) d\boldsymbol{r}$ and substitute Eq. (4.23) for $\delta n(\boldsymbol{r})$

$$Z_{\rm eff}(r) = Z - \frac{\pi}{2} g - \frac{4\sqrt{g^2 - g_c^2}}{\pi} \log\frac{r}{R}. \tag{4.24}$$

Since the logarithmic term represents the renormalization coming from screening at distances away from the center, we should replace $(g \equiv Z\alpha) \to (Z_{\rm eff}\alpha \equiv g_{\rm eff})$. This leads to a self-consistent renormalization of the coupling that can be written in an appealing RG fashion as $dg_{\rm eff}/d\log(r) = -4\alpha\sqrt{g_{\rm eff}^2 - g_c^2}$. In this way, it can be immediately seen that the coupling $g_{\rm eff}$ will "flow" to the constant value g_c within a finite distance [see also Gupta and Sen (2009) for a related renormalization procedure]. As such, irrespective of the bare Z, the system self-consistently rearranges itself so that electrons at large distances never feel a supercritical effective coupling. The undercritical (stable) situation is therefore protected. This reasoning agrees with expectations for the corresponding problem in QED, where it was shown that, within the Thomas-Fermi approximation, the vacuum polarization charge in superheavy nuclei behaves in such a way as to reduce Z to the threshold value (Müller and Rafelski, 1975).

This is quite different from a metal, to the extent that graphene always leaves a universal amount of charge $(Z_c = g_c/\alpha)$ unscreened at large distances. Such behavior derives from the sharp transition between the undercritical and supercritical regimes. On the one hand, the system wishes to screen as much charge as it possibly can. But, on the other hand, it cannot screen if $g < g_c$, therein lying the compromise that makes screening stop when Z reaches Z_c.

c. Nonlinear Thomas-Fermi theory and beyond

While the above approach is valid in principle only for $g \gtrsim g_c$, the fact that qualitatively supercritical graphene resembles a superheavy atom suggests the use of TF theory, which is exact for atoms with $Z \to \infty$ (Lieb, 1981), and affords an approximation from the opposite limit $g \gg g_c$. If we wish to calculate how Coulomb's law is modified in this regime, we can calculate the total potential $V_{\rm eff}(\boldsymbol{r}) = V(\boldsymbol{r}) + \delta V(\boldsymbol{r})$, where $\delta V(\boldsymbol{r}) = (e^2/\epsilon_0)\int[\delta n(\boldsymbol{r}')/|\boldsymbol{r} - \boldsymbol{r}'|]d\boldsymbol{r}'$ is the potential induced by the screening charge. Within TF we replace $\delta n(\boldsymbol{r}') = n[\mu - V(\boldsymbol{r})] - n(\mu)$, and the homogeneous density depends on μ via $n = s_E\mu^2/\pi v^2$. Solution of the resulting integral equation leads to the correction to Coulomb's law, which asymptotically reads (Katsnelson, 2006)

$$V_{\rm eff}(\boldsymbol{r}) \approx \frac{e^2}{\epsilon_0 r}\left[\frac{Z}{1 + 2Z\alpha^2\log(r/R)}\right], \tag{4.25a}$$

$$V_{\rm eff}(\boldsymbol{r}) \approx \frac{e^2}{\epsilon_0 r(q_s r)^2}\left[\frac{Z}{1 - 2Z\alpha^2\log(q_s R)}\right], \tag{4.25b}$$

valid for $\mu = 0$, $r \gg R$ and $\mu \neq 0$, $rq_s \gg 1$, respectively, where $q_s = 4\alpha\mu/v$ is the screening length (4.18). One notes that the overall space dependence is formally the same as the one obtained within RPA, at both zero and finite density. Hence the bracketed coefficients in Eq. (4.25) can be interpreted as a renormalization of the valence. The important difference is that, in the limit $Z \to \infty$ of interest in the context of TF, the nominal valence Z disappears from $V_{\rm eff}(\boldsymbol{r})$, which thus becomes universal (and undercritical). Hence, even for strong impurities one can formally use perturbative expressions for the screened potential, corrected for this renormalization of Z.

It is important to emphasize that, since at this stage we are concerned with screening and corrections to the induced charge coming from electron-electron interactions, $g = Z\alpha$ is no longer the relevant parameter alone, but both Z and α (that controls the interaction) independently. For this reason, Fogler, Novikov, and Shklovskii (2007) argued that the result (4.25) is valid only for small α. More precisely, it applies for $1/Z \ll \alpha \ll 1/\sqrt{Z}$, and provided that $\log(r/R) < 1/\alpha$. Otherwise, for intermediate electron-electron coupling $(\alpha \sim 1)$, the asymptotic screened potential should follow $V_{\rm eff} \approx Z_c e^2/\epsilon_0 r$, with $Z_c = g_c/\alpha = 1/(2\alpha)$. This result embodies the undercritical protection discussed in Sec. IV.B.2.b, insofar as the supercritical core is always self-consistently screened so that $Z_{\rm eff} \to Z_c$. Moreover, within the supercritical core region $r < 2Z\alpha^2 R$ the effective potential decays as $\propto 1/r^{3/2}$. This obtains treating graphene as an ideal classical metal, under the assumption of quasicomplete screening in the core region (Fogler, Novikov, and Shklovskii, 2007).

3. Finite mass

We now briefly address the differences expected in the screening properties of charged impurities in massive graphene. We consider only the undoped situation, and assume $\mu = -m$, such that none of the bound levels (4.6) are occupied.

a. Weak coupling ($g < g_c$)

It is clear that at weak coupling one can directly rely on perturbative results [Sec. IV.B.1], and obtain the induced density from $\delta n(\boldsymbol{q}) = -ZV_0(\boldsymbol{q})\Pi(\boldsymbol{q})$. $\Pi^{(1)}(\boldsymbol{q})$ has been calculated in Eq. (2.14), and simple substitution yields the following asymptotics:

$$\delta n(\boldsymbol{r}) \sim Z\alpha \begin{cases} \frac{\pi}{2}\delta(\boldsymbol{r}) & r \simeq a \to 0 \\ -\lambda_C^{-2}\log(\lambda_C/r) & a \ll r \ll \lambda_C, \\ -\lambda_C r^{-3} & r \gg \lambda_C \end{cases} \quad (4.26)$$

where $\lambda_C = 1/mv$ is the Compton wavelength and a the lattice parameter of graphene. The short distance term is the same as found in the massless case (4.14) and (4.17), which makes sense given that when $r \ll \lambda_C$ the system does not "feel" the mass yet. It has a screening sign. However, as the distance increases screening is increasingly suppressed, first weakly up to λ_C, and then strongly, beyond λ_C. In fact, since here $\delta n(\boldsymbol{q} = 0) = 0$, we have exactly $\int \delta n(\boldsymbol{r})d\boldsymbol{r} = 0$. The meaning of this is simple: the total induced charge is zero. The system cannot screen beyond $r \gtrsim \lambda_C$ because it is essentially an insulator (or a semiconductor with μ in the middle of the gap). Notwithstanding, unlike a conventional insulator, gapped graphene shows a novel screening behavior at short distances, reflected in the live dependence of $\delta n(\boldsymbol{r})$ on the distance up to λ_C.

b. Strong coupling ($g > g_c$)

In gapped graphene, screening in the supercritical regime is qualitatively easier to understand, at least when $g \gtrsim \tilde{g}_c$. If the first level has just merged inside to hole continuum, its effective probability density $|\Psi_c(\boldsymbol{r})|^2$ remains exponentially localized, as described in Sec. IV.A.2.a. Invoking completeness of the set of single-particle states, one can easily show that the noninteracting induced charge follows (Pereira, Kotov, and Castro Neto, 2008)

$$\delta n(\boldsymbol{r}) \approx |\Psi_c(\boldsymbol{r})|^2 + \delta n_{\mathrm{pol}}(\boldsymbol{r}), \quad (4.27)$$

where $\delta n_{\mathrm{pol}}(\boldsymbol{r}) \approx \sum_{E<-m}|\chi_E(\boldsymbol{r})|^2 - |\chi_E^0(\boldsymbol{r})|^2$ represents the vacuum polarization (i.e., the induced charge coming from the full set of plane wave states), and is the same quantity that obtains in RPA (4.26). Clearly, the contribution from the supercritical state alone makes $\delta n(\boldsymbol{r})$ in Eq. (4.27) highly localized within the Compton wavelength λ_C. For all purposes, this state screens as a bound state would, and consequently one expects the impurity valence to be reduced by one unit times the degeneracy N of the level. But since $N = 4$, this would imply, for the experimentally significant cases of $Z \sim 1$, a tendency to overscreen the Coulomb center. This brings us again to the role of interactions. The above would be true in the limit of weak interaction $\alpha \ll 1$. But, in that case, the supercritical regime would require $Z \gg 1$, which is not feasible. In the end, if supercritical systems are to be produced, electron-electron interactions should be strong which, besides requiring the computation of the vacuum polarization in strong coupling, brings the question of the renormalization of the bound levels themselves (Lamb shift). This situation, however, is completely analogous to the problem of superheavy nuclei in QED, and an extensive account of its particular features and difficulties can be found in Greiner *et al.* (1985).

C. From single to many particle interactions

Coupling to an external Coulomb field can be seen as the zeroth order approach to the full many-body electron interactions in graphene. The decisive difference that leaves graphene apart from standard electronic systems is the existence of the supercritical region, which, for the Coulomb field, has the peculiarities discussed so far. Since the coupling constant in vacuum is $\alpha \approx 2$, one can justifiably ask whether supercritical effects carry to electrons interacting among themselves. After all, even if a simplification from a reference frame moving with an electron the problem becomes an impurity one again.

1. Interacting two-body problem

The two particle problem has traditionally provided valuable insights into the full many-body phenomena in condensed matter [e.g., the Cooper pairing (Cooper, 1956)]. The chiral nature of the electronic states, however, precludes the usual decoupling between center-of-mass and relative coordinates, except for s states in a quiescent center of mass (Sabio, Sols, and Guinea, 2010b). Even so, they showed that the supercritical collapse is a general effect present in the two-body problem. In this case, the critical coupling occurs at $\alpha_c = 1$ and 2.24 for s and p channels, respectively. The interacting two-body problem usually encodes much of the physics that the many-body system displays. One example is the study of pairing, pair condensation, and other processes which are dominated by two particle channel events. This has a clear relation with the issue of spontaneous gap generation, discussed in Sec. III.B. The prospect of exact solution of the two particle problem would afford more controllable means to explore this instability in graphene.

2. Excitons and spontaneous mass generation

It is noteworthy that the value $\alpha_c = 1$ quoted above is tantalizingly close to recent calculations of the critical coupling which precipitates a spontaneous mass generation and metal-insulator transition in undoped graphene. Those values range from $\alpha_c = 0.8$ (Vafek and Case, 2008) to $\alpha_c = 1.1$ obtained with Monte Carlo calculation (Drut and Lähde, 2009b) or by using the Schwinger-Dyson equation (Khveshchenko, 2009). As described in Sec. III.B, this metal-insulator transition in graphene has been ascribed to the emergence of an excitonic instability beyond α_c.

Recently, the excitonic problem has been considered *vis-á-vis* the supercritical instability of the Coulomb center. Instabilities in the particle-hole channel appear at critical couplings consistent with the above (Gamayun, Gorbar, and Gusynin, 2009; Wang, Fertig, and Murthy, 2010). For example, Gamayun, Gorbar, and Gusynin (2009) showed that solving the Bethe-Salpeter equation in graphene leads to instability-prone tachyonic states ($E^2 < 0$) at $\alpha_c = 1.6$. Such states are the analog in the two channel many-body language of the quasibound resonances for supercritical impurities, and a glimmer of supercritical effects in the fully interacting problem.

D. Supercritical physics in experiments

The nonperturbative nature of supercritical Coulomb impurities and the associated analytical difficulties preclude unequivocal predictions regarding the possibility of crossing

the supercritical threshold. Experimental investigation of this problem requires the ability to vary the strength of the Coulomb impurity and/or the electron-electron interactions. Control over the dielectric environment provides a handle to tune interactions and impurity strength at the same time, via selection of ϵ_0. Experiments in this vein have been performed by Jang *et al.* (2008) and Ponomarenko *et al.* (2009), showing that it is possible to controllably tune the value of ϵ by exploring substrates with different dielectric properties. Variation of Z is a more delicate issue. Chen *et al.* (2008) devised a way to add monovalent ions to graphene via K irradiation, in quantities that can be controlled with some precision. But exploration of the supercritical regime might require higher valences. For real impurities, the valence is determined by the nature of the impurity atom and the host system, and cannot be changed. One can, in principle, use ions of different valence, but here the difficulty lies in the fact that valences higher than $Z = 2$ are very unlikely. One possible alternative to this constraint imposed by nature would be to resort to sharp STM tips, whose strong local field could mimic a strong local charge. As mentioned in the beginning of this section, the experimental exploration and/or confirmation of the supercritical state would be a rather important milestone, not only in understanding the physics of graphene, but because it would afford a glimpse to what might happen in the more fundamental QED situation.

V. STRONG CORRELATIONS IN GRAPHENE

A. Mass gaps in the honeycomb lattice

Graphene is a semimetal (SM) with gapless quasiparticles. The Dirac points in graphene are protected by the combination of sublattice and translational symmetries of the honeycomb lattice. The point group symmetry of the honeycomb lattice C_{6v} can be decomposed into the point group of the triangular sublattice and the $\mathbb{Z}_2$ sublattice symmetry group, $C_{3v} \otimes \mathbb{Z}_2$. Violation of sublattice symmetry leads to the opening of a mass gap in the Dirac Hamiltonian. This broken symmetry can be physically implemented either by the Semenoff gap (Semenoff, 1984), which is induced by a staggered scalar potential that breaks the sublattice inversion symmetry, as discussed in Eq. (3.40), or by the Haldane gap (Haldane, 1988), where there is an additional broken TRS induced by the inclusion of circulating current loops with zero magnetic flux per unit cell, corresponding to a staggered magnetic field. In particular, a system that breaks inversion and TRS is susceptible to a "parity" anomaly, where the application of an electric field generates a net axial current flowing between the two valleys in graphene (Jackiw, 1984).

In the presence of mirror symmetry along the z axis, the spin-orbit interaction in graphene has the form (Kane and Mele, 2005)

$$\mathcal{H}_{\mathrm{SO}} = \Delta_{\mathrm{SO}} \sum_{\mathbf{k},\sigma} \Psi^{\dagger}_{\mathbf{k},\sigma} \tau_0 \otimes \sigma_3 \otimes s_3 \Psi_{\mathbf{k},\sigma}, \tag{5.1}$$

where Δ_{SO} is the spin-orbit coupling gap and s_3 is the diagonal Pauli matrix in spin space. The other matrices follow the convention in the Dirac Hamiltonian (2.6). The spin-orbit interaction in graphene breaks the spin degeneracy in the valleys, giving rise to spin polarized currents that flow along the edge states of the system, a quantum spin Hall state (Kane and Mele, 2005). Although the spin-orbit coupling gap in graphene is rather small, $\Delta_{\mathrm{SO}} \approx 10^{-3}$ meV, (Huertas-Herno, Guinea, and Brataas, 2006; Min *et al.*, 2006; Yao *et al.*, 2007), it can be drastically enhanced either by curvature effects (Huertas-Herno, Guinea, and Brataas, 2006) or by impurities (Castro Neto and Guinea, 2009). The spin-orbit coupling is also logarithmically enhanced by Coulomb interactions (Kane and Mele, 2005), as discussed in Sec. III.B. When the mirror symmetry is broken by either a substrate or an external electric field, an additional Rashba term is allowed

$$\mathcal{H}_R = \lambda_R \sum_{\mathbf{k},\sigma} \Psi^{\dagger}_{\mathbf{k},\sigma} \tau_3 \otimes (\sigma_1 \otimes s_2 - \sigma_2 \otimes s_1) \Psi_{\mathbf{k},\sigma}, \tag{5.2}$$

where $\lambda_R > 0$ is the Rashba coupling. The induced gap is $2(\Delta_{\mathrm{SO}} - \lambda_R)$for $\lambda_R < \Delta_{\mathrm{SO}}$, closing to zero when $\lambda_R > \lambda_{\mathrm{SO}}$ (Kane and Mele, 2005).

Kekule lattice distortions (Hou, Chamon, and Mudry, 2007), which break the translational symmetry of the lattice, also lead to the opening of gaps in graphene, whereas lowering the rotational symmetry of the C_{3v} group, by stretching the honeycomb lattice in one direction, does not. In the presence of topological defects in the order parameter, such as vortices, the midgap states which are bounded to them allow the emergence of excitations with fractional statistics under vortex exchange (Hou, Chamon, and Mudry, 2007; Chamon *et al.*, 2008a; Chamon *et al.*, 2008b; Seradjeh and Franz, 2008). In the superconducting case, the vortex core may sustain a quantum Hall state in the presence of a strong Zeeman coupling of the electrons with the magnetic field, which lifts the spin degeneracy (Herbut, 2010). In the most general case, where any spin, valley, and pairing symmetries are allowed, 36 different types of instabilities that generate mass gaps in graphene have been classified (Ryu *et al.*, 2009).

B. Charge and magnetic instabilities

Although no evidence of mass gaps has been found in graphene, numerical results predicted a semimetal-insulator transition in the presence of strong correlations. Quantum Monte Carlo calculations on the Hubbard model for the honeycomb lattice at half-filling predicted the opening of a Mott gap above the critical ratio $U/t \gtrsim 5$ (Sorella and Tosatti, 1992; Martelo *et al.*, 1997; Paiva *et al.*, 2005), where $t \approx 2.8$ eV is the hopping energy and U is the on-site electronic repulsion. A more recent quantum Monte Carlo calculation found a gapped antiferromagnetic (AF) state at half-filling for $U/t > 4.3$, preceded by an intermediate coupling insulating phase for $3.5 < U/t < 4.3$, which has been attributed to a gapped spin liquid state formed by short-range resonating valence bonds (Meng *et al.*, 2010). An insulating AF ground state has also been predicted above $U/t \gtrsim 4$ (Martelo *et al.*, 1997; Furukawa, 2001). Variational (Hanisch *et al.*, 1995) and mean-field calculations (Peres, Araújo, and Bozi, 2004) predicted the possibility of Nagaoka ferromagnetism (where the polarization is maximal) above a

critical coupling both in the half-filled and in the doped regimes. Although the validity of the Hubbard model in graphene may be questioned since it does not include long-range Coulomb interactions, it could be in principle justified if one accounts for a strong screening effect from a substrate which can deplete the long-range part of the interactions [or also, perhaps, by accounting for dynamical screening effects from graphene itself (Reed *et al.*, 2010)], leaving only the short-range part of the electron-electron interactions. The extent of validity of the Hubbard model in graphene is a subject of ongoing debate.

The bare spin polarization in graphene is a 2×2 tensor (Peres, Araújo, and Bozi, 2004),

$$\Pi^{+-}_{x,y}(\mathbf{q}, \tau) = \langle S^{+}_{x}(\mathbf{q}, \tau) S^{-}_{y}(-\mathbf{q}, 0)\rangle, \tag{5.3}$$

where S^{+}_{x} and S^{-}_{x} are the spin raising and lowering operators in the two sublattices, $x = a, b$. Written in terms of the Green's function (2.11) with additional spin labels,

$$\Pi^{(1)+-}_{x,y}(\mathbf{q}, i\omega) = -\frac{1}{4}\sum_{\mathbf{k},s,s'=\pm} \mathcal{A}^{s}_{x,y}(\mathbf{k})\mathcal{A}^{s'}_{y,x}(\mathbf{k}+\mathbf{p}) \times \frac{f[E_{s,\uparrow}(\mathbf{k})] - f[E_{s',\downarrow}(\mathbf{k}+\mathbf{q})]}{i\omega + E_{s,\uparrow}(\mathbf{k}) - E_{s',\downarrow}(\mathbf{k}+\mathbf{q})}, \tag{5.4}$$

where $\hat{\mathcal{A}}^{s} \equiv 1 + s\mathbf{k}\cdot\boldsymbol{\sigma}/k$, and $E_{s,\sigma}(\mathbf{k}) = sv|\mathbf{k}| - \mu$ describes the two branches of the spectrum near the Dirac points. Since $\Pi_{a,a} = \Pi_{b,b}$ and $\Pi_{a,b} = \Pi^{*}_{b,a}$ by the honeycomb lattice symmetry, the eigenvalues of the spin polarization are $\Pi_{F/\mathrm{AF}} = \Pi^{+-}_{a,a} \pm |\Pi^{+-}_{a,b}|$, which correspond to ferromagnetic (+) and AF (−) states. In RPA, the spin susceptibility is $\hat{\chi} = [\hat{\mathbf{1}} - U\hat{\Pi}^{(1)}]^{-1}\hat{\Pi}^{(1)}$, and the critical Hubbard coupling required for a divergence in the spin susceptibility in graphene is (Peres, Araújo, and Bozi, 2004)

$$U^{F/\mathrm{AF}}_{c} = \frac{1}{\Pi^{(1)}_{F/\mathrm{AF}}(0)}. \tag{5.5}$$

The ferromagnetic transition translates to the condition $U^{F}_{c} = 2/\rho(\mu) \approx D^2/|\mu|$, which is the Stoner criterion, where $\rho(E)$ is the DOS and D is the band width. The AF transition occurs at $U^{\mathrm{AF}}_{c} \approx D^2/(D - |\mu|)$.

Application of an in-plane magnetic field B splits the spin degeneracy at the Dirac points, creating two Fermi surface pockets with opposite spins. Including the Zeeman coupling, $H_B = \sum_{\sigma}\sigma B\hat{n}_{\mathbf{k},\sigma}$ into the Hamiltonian, the spin polarized energy spectrum is $E_{s,\sigma}(\mathbf{k}) = sv|\mathbf{k}| + \sigma B - \mu$. The nesting between the two Fermi surface sheets can produce a logarithmic divergence in the spin polarization in the limit $|B| \gg \max(T, |\mu|)$ (Bercx, Lang, and Assaad, 2009),

$$\Pi^{(1)}_{AF}(0) \sim \rho(B)\ln\left(\frac{|B|}{\max(T, |\mu|)}\right). \tag{5.6}$$

This instability brings the possibility of a canted AF state in graphene. In the presence of Landau level quantization due to the application of an out-of-plane magnetic field, electronic interactions may lead to the formation of quantum Hall ferromagnetic states at integer values of the filling factor (Nomura and MacDonald, 2006). The magnetic field has also been proposed as a source of a charge density wave (CDW) Peierls distortion in the zero Landau level in graphene, breaking the parity symmetry between the valleys (Fuchs and Lederer, 2007). For a discussion of interaction effects at strong magnetic fields, see Sec. VIII.

For Dirac fermions in $2 + 1$ dimensions, a CDW instability translates into the phenomenon of chiral symmetry breaking, with spontaneous generation of a mass term that breaks the sublattice symmetry. The AF state is favored by strong on-site repulsion and competes with the long-range part of the Coulomb field, which can favor either strong-coupling ferromagnetism (Peres, Araújo, and Bozi, 2004) or else excitonic CDW instabilities at strong coupling (Khveshchenko, 2001a; 2001b; Khveshchenko and Leal, 2004; Drut and Lähde, 2009a; 2009b; Liu, Li, and Cheng, 2009).

At large N, with N the number of fermionic flavors, the continuum limit of the Hubbard model in the honeycomb lattice falls in the universality class of the Gross-Neveu model (Gross and Neveu, 1974) for massless Dirac fermions in $2 + 1$ dimensions, with four-fermion contact interactions. The extended version of this model accommodates the short-range piece of the Coulomb interaction involving the repulsion between nearest neighbor sites V (Herbut, 2006). In addition to the Gaussian fixed point, which controls the SM phase, the RG flow of the extended model was shown to be controlled by two other fixed points at large N: an AF fixed point and a CDW fixed point, both unstable towards the Gaussian fixed point at weak coupling, and having a runaway direction to strong coupling when U or V are sufficiently large. The two fixed points compete, resulting in the phase diagram shown in Fig. 22. The fact that the AF fixed point has only one unstable direction to leading order in $1/N$ motivated the conjecture that the semimetal-insulator transition to the AF state is continuous and of the Gross-Neveu type (Herbut, 2006). The symmetry analysis of the possible quartic terms has been discussed by Herbut, Juricic, and Roy (2009).

The $1/N$ results were confirmed qualitatively by numerical renormalization group (NRG) calculations for the extended Hubbard model in the honeycomb lattice (Raghu *et al.*, 2008). In the presence of next-nearest-neighbor repulsion, the NRG calculations suggested the possibility of competition between the CDW and spin density wave (SDW) phases with nontrivial topological insulating states, such as the quantum spin Hall state, where TRS is spontaneously broken (Raghu *et al.*, 2008). Functional renormalization group calculations for the $t - J$ model on the honeycomb lattice

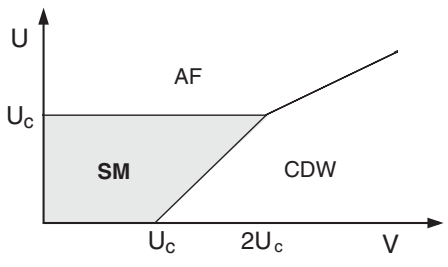

FIG. 22. Semimetal (SM) insulator transition predicted by the renormalization group analysis of the extended Hubbard model, in large N expansion. U is the on-site Hubbard coupling and V is the nearest neighbor site repulsion. U_c stands for the critical coupling. AF: antiferromagnetic phase; CDW: charge density wave state. From Herbut, 2006.

with on-site and nearest neighbor repulsion also suggested the possibility of strong-coupling CDW and SDW instabilities in graphene at half-filling (Honerkamp, 2008). In the doped regime, the $t-J$ model can favor the formation of superconducting states for $J>2t$, either in the triplet or in the d-wave singlet channels (Honerkamp, 2008).

In the high doping regime, the proximity of the Fermi level to the Van Hove singularities, where the graphene DOS diverges logarithmically, may favor a Pomeranchuck instability, rather than a gapped state. In that case, the redistribution of the electronic density generates a deformation of the Fermi surface, which lowers the lattice C_{3v} point group, instead of breaking the $\mathbb{Z}_2$ sublattice symmetry. In the extended Hubbard model at high doping, the Pomeranchuck instability is favored by the repulsion between nearest neighbor sites, which renormalizes the kinetic energy at the mean-field level, and competes with the on-site repulsion, which favors a ferromagnetic state when the Stoner criterion is satisfied (Valenzuela and Vozmediano, 2008).

When coated with metallic atoms that have a strong tendency to hybridize with the carbon p_z orbitals, graphene can induce strong itinerant ferromagnetism in the metallic bands (Uchoa, Lin, and Castro Neto, 2008).

C. Local magnetic moments

For massless Dirac particles, the formation of localized states is usually harder than in usual Fermi systems due to the Klein paradox, in which the fermions can easily tunnel through a barrier regardless of its height. Defects such as vacancies, where a carbon atom is knocked out from the plane, have been shown to generate localized states in graphene (Vozmediano *et al.*, 2005; Pereira *et al.*, 2006), and were recently observed in STM experiments (Ugeda *et al.*, 2010). Vacancies have also been found to host local magnetic states (Yazyev and Helm, 2007; Chen *et al.*, 2011).

Short-range interacting impurities can generate local resonances, which are quasilocalized states. At half-filling, the energy of the resonance ε_0 is given by (Skrypnyk and Loktev, 2006; Wehling *et al.*, 2007)

$$U_0=\frac{D^2}{\varepsilon_0\ln|\varepsilon_0^2/(D^2-\varepsilon_0^2)|}, \tag{5.7}$$

where U_0 is the scattering potential of the impurity and D is the bandwidth. The resonance induces accumulation of LDOS at the Fermi level around the impurity $\rho(r,\omega)$, which decays as $1/r$ (Bena and Kivelson, 2005), whereas the Friedel oscillations decay as $1/r^2$ for intracone scattering and as $1/r$ for intercone scattering (Bena, 2008).

Besides defects, zigzag edges also lead to local magnetism in the presence of interactions (for a more detailed discussion, see Sec. VI). In bulk graphene, a simple way to generate localized magnetic states is provided by the adsorption of adatoms with inner shell electrons. On the lattice, the adatoms can stay in different locations relative to the two sublattices in graphene. Transition metals are usually more stable sitting in the hollow site, at the center of the honeycomb hexagon (Chan, Neaton, and Cohen, 2008), whereas simple molecules and atoms such as hydrogen (H) tend to hybridize more strongly with the carbons, sitting on top of them and generating a large local moment (Yazyev and Helm, 2007). In particular, H adsorption creates a midgap state (Boukhvalov, Katsnelson, and Lichtenstein, 2008; Wehling, Yuan *et al.*, 2010) and distorts locally the sp^2 carbon bonds, which acquire sp^3 character (Elias *et al.*, 2009). This distortion can induce a strong local enhancement of the spin-orbit coupling up to ≈ 7 meV, as in diamond, and generate a strong local magnetic anisotropy (Castro Neto and Guinea, 2009). Adatoms can also form local moments from substitutional defects on single and double vacancies in graphene (Krasheninnikov *et al.*, 2009; Venezuela *et al.*, 2009).

The heuristic criterion that describes the formation of a local magnetic moment is addressed at the mean-field level by the Anderson impurity model (Anderson, 1961). In the top carbon case, assuming that the adatom sits on a carbon (see Fig. 23), say on sublattice B, the hybridization Hamiltonian is $H_V=V\sum_\sigma[f_\sigma^\dagger b_\sigma(0)+\text{H.c.}]$, where f_σ ($f_\sigma^\dagger$) annihilates (creates) an electron with spin $\sigma=\uparrow,\downarrow$ at the impurity. In momentum space, this translates into

$$\mathcal{H}_V=V\sum_{\mathbf{p},\sigma}(f_\sigma^\dagger b_{\mathbf{p},\sigma}+b_{\mathbf{p},\sigma}^\dagger f_\sigma). \tag{5.8}$$

If $n_\sigma=\langle f_\sigma^\dagger f_\sigma\rangle$ is the occupation of the localized level for a given spin, the effective Hamiltonian of the level is

$$\mathcal{H}_f=\sum_\sigma \varepsilon_\sigma f_\sigma^\dagger f_\sigma, \tag{5.9}$$

with $\varepsilon_\sigma=\varepsilon_0+Un_{-\sigma}$, after a proper mean-field decomposition of the Hubbard term $H_U=Uf_\uparrow^\dagger f_\uparrow f_\downarrow^\dagger f_\downarrow$, which accounts for the charging energy U to doubly occupy the level. The hybridized level becomes magnetic when $n_\uparrow\neq n_\downarrow$. The occupation is derived self-consistently by integrating the f-electron DOS from the bottom of the graphene band up to the Fermi level μ,

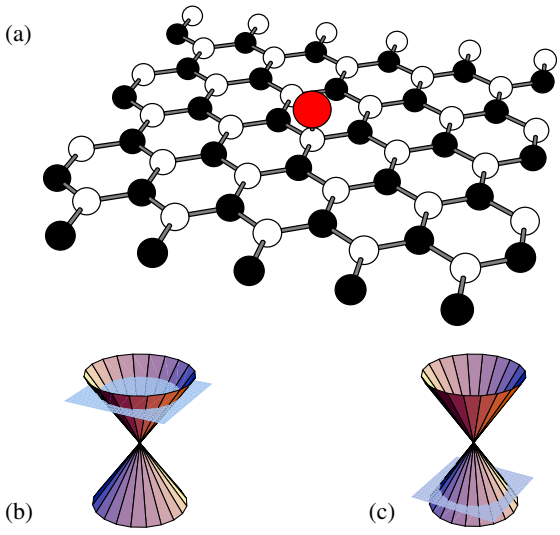

FIG. 23 (color online). (a) Honeycomb lattice with an impurity atom. Black: sublattice A; white: sublattice B. Intersection of the Dirac cone spectrum $E(\mathbf{k})=\pm v|\mathbf{k}|$ with the localized level $E_f=\varepsilon_0$: (b) $\varepsilon_0>0$, (c) $\varepsilon_0<0$.

$$n_\sigma = -\frac{1}{\pi}\,\mathrm{Im}\int_{-\infty}^{\mu} d\omega \frac{1}{\omega - \varepsilon_\sigma - \Sigma_{ff}(\omega)}, \tag{5.10}$$

where $\Sigma_{ff}(\omega)$ is the self-energy of the localized electrons. In the cone approximation of the spectrum in graphene, for the top carbon case,

$$\Sigma_{ff}(\omega) = \omega[1 - Z^{-1}(\omega)] - i\Delta|\omega|\theta(D - |\omega|), \tag{5.11}$$

where $\Delta = \pi V^2/D^2$ is the dimensionless hybridization, D is the effective bandwidth, and

$$Z^{-1}(\omega) = 1 + \frac{V^2}{D^2}\,\ln\left|1 - \frac{D^2}{\omega^2}\right| \tag{5.12}$$

gives the quasiparticle residue $Z(\omega)$ which vanishes logarithmically at the Dirac points ($\omega \to 0$).

Because of the vanishing DOS, the level broadening [given by $\mathrm{Im}\Sigma^R_{ff}(\omega)$] scales linearly with the energy around the Dirac points (González-Buxton and Ingersent, 1998; Zhang, Hu, and Yu, 2001; Skrypnyk and Loktev, 2006; Uchoa *et al.*, 2008). The DOS induced around the bare level ε_σ does not decay as a Lorentzian as in usual metals, but shows a long tail proportional to $1/\omega$. This tail induces several peculiar features in the magnetic states. For instance, a local moment is allowed to exist when the bare level is empty ($\varepsilon_0 < \mu$) or doubly occupied ($\varepsilon_0 + U > \mu$) (see Fig. 24). The presence of the Dirac point also breaks the symmetry around the line $\mu - \varepsilon_0 = U/2$, and makes the scaling of the curves shown in Fig. 24 nonuniversal. Furthermore, there is a physical asymmetry between the cases where the level is above ($\varepsilon_0 > 0$) or below ($\varepsilon_0 < 0$) the Dirac point. When $\varepsilon_0 = 0$, as in the case of a vacancy, the level decouples from the bath and becomes magnetic for any $\mu > 0$, regardless of the value of U (Pereira *et al.*, 2006; Uchoa *et al.*, 2008).

Since the chemical potential in graphene can be tuned, the formation of local magnetic states can be controlled by the application of a gate voltage (Uchoa *et al.*, 2008). The low density of states around the localized level also makes the formation of local moments in graphene much easier than in usual metallic hosts. As a result, the adatoms can achieve high magnetic moments at relatively small U (Uchoa *et al.*, 2008; Cornaglia, Usaj, and Balseiro, 2009).

The formation of local moments is also affected by the specific location of the adatom in the lattice (see Fig. 25). For instance, when the adatom sits in the center of the honeycomb hexagon (H site), the tight-binding hybridization Hamiltonian is (Uchoa *et al.*, 2009)

$$H_V = \sum_{\sigma,i}[V_{a,i}a^\dagger_\sigma(\mathbf{a}_i) + V_{b,i}b^\dagger_\sigma(-\mathbf{a}_i)]f_\sigma(0) + \text{H.c.}, \tag{5.13}$$

where $\mathbf{a}_i$ ($i = 1, 2, 3$) are the three nearest neighbor vectors of the honeycomb lattice and $V_{x,i}$ ($x = a, b$) is the hybridization strength of the adatom with each of the nearest surrounding carbon atoms. In momentum representation,

$$H_V = \sum_{\mathbf{p}\sigma}(V^*_{a,\mathbf{p}}a^\dagger_{\mathbf{p}\sigma} + V_{b,\mathbf{p}}b^\dagger_{\mathbf{p}\sigma})f_\sigma + \text{H.c.}, \tag{5.14}$$

where

$$V_{x,\mathbf{p}} = \sum_{i=1}^{3} V_{x,i}e^{i\mathbf{p}\cdot\mathbf{a}_i}. \tag{5.15}$$

The top carbon case is recovered by setting $V_{a,\mathbf{p}} \equiv V$ and $V_{b,\mathbf{p}} = 0$ or vice versa. For s-wave orbitals, $V_{x,i} \equiv V$, whereas for in-plane f-wave orbitals the hybridization is antisymmetric in the two sublattices, $V_{a,i} = -V_{b,i} \equiv V$. In the case of substitutional impurities (S sites), either $V_{a,i} = 0$ or $V_{b,i} = 0$. The quantum interference between the different hybridization paths of the electrons can modify the energy scaling of the level broadening in Eq. (5.11) (Uchoa *et al.*, 2009), and can also change the shape of the Fano resonances in scanning tunneling spectroscopy measurements, allowing a clear identification of the adatom position with a scanning tunneling spectroscopy tip (Uchoa *et al.*, 2009; Saha, Paul, and Sengupta, 2010; Wehling, Dahal, *et al.*, 2010).

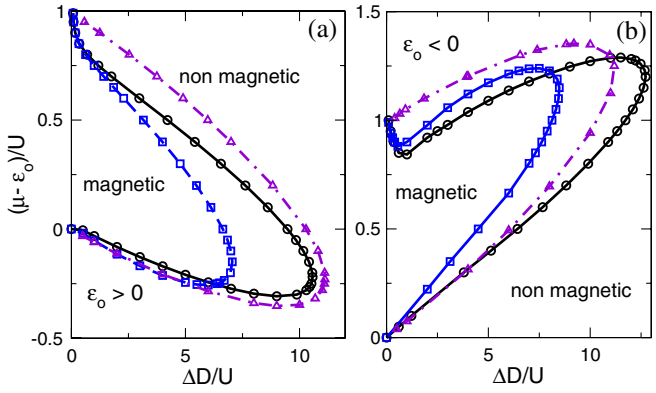

FIG. 24 (color online). Boundary between magnetic and nonmagnetic impurity states in the scaling variables $x = \Delta D/U$ and $y = (\mu - \varepsilon_0)/U$ for (a) $\varepsilon_0 > 0$ and (b) $\varepsilon_0 < 0$. $|\varepsilon_0|/D = 0.029, 0.043, 0.029$ and $V/D = 0.14, 0.14, 0.04$ for circles, squares, and triangles, respectively. The upturn close to $y = 1$ and $x \to 0$ in (b) signals a crossover to the Fermi-liquid regime $\mu, U \gg |\varepsilon_0| > 0$, where the Dirac points are physically irrelevant. This feature is not visible in this scale when V is very small (triangles). From Uchoa *et al.*, 2008.

D. Kondo effect

The formation of a Kondo screening cloud around a magnetic moment is described by the Anderson Hamiltonian (5.8) in the strong-coupling limit, $U \to \infty$, where the valence fluctuations are suppressed and the local moment becomes

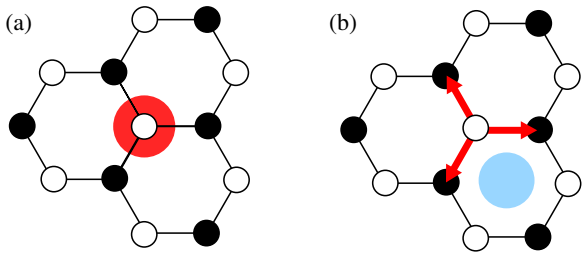

FIG. 25 (color online). Two adatom configurations in graphene: (a) the adatom (circle) sits on top of a carbon atom, and (b) the adatom (circle) sits at the center of the honeycomb hexagon, hybridizing equally with the two sublattices. Arrows: nearest neighbor vectors.

a good quantum number. In the standard mean-field approach, the spin $1/2$ fermionic fields are replaced by fermionic fields with larger degeneracy, $N > m$, which corresponds to an SU(N) extension of the problem, with a corresponding Kondo Hamiltonian (Coqblin and Schrieffer, 1969)

$$\mathcal{H}_K = J_K \sum_{mm'} \sum_{\mathbf{k}\mathbf{k}'} \psi^\dagger_{\mathbf{k},m} f^\dagger_{m'} f_m \psi_{\mathbf{k}',m'}, \tag{5.16}$$

where $J_K \sim V^2/|\varepsilon_0 - \mu|$ is the Kondo coupling, ψ_m ($\psi^\dagger_m$) are annihilation (creation) operators of the itinerant electrons, and the local f fields are constrained to a fixed occupancy. At the mean-field level, which is asymptotically exact at large N, the Kondo order parameter can be extracted either from the standard slave boson approach to the Anderson model (Coleman, 1983; Newns and Read, 1987) or else by an equivalent path integral approach starting from the Kondo Hamiltonian (5.16) (Read and Newns, 1983).

The application of these methods to semimetals with a vanishing DOS, $\rho(\omega) = \rho_0|\omega|^r$, with $r > 0$, resulted in the prediction of a Kondo quantum critical point (QCP) at half-filling ($\mu = 0$). In that case, a Kondo cloud is expected for $J_K > J_K^c = r/\rho_0 D^r$, below the Kondo temperature (Withoff and Fradkin, 1990)

$$T_K \approx |J_K - J_K^c|^\nu, \tag{5.17}$$

where $\nu = 1/r$ and D is the ultraviolet cutoff. Since the scaling dimension of the hybridization V in the Anderson model is $\dim[V] = (1 - r)/2$, the case $r = 1$ acts as an upper critical scaling dimension in the problem, where the scaling is marginal (Vojta and Fritz, 2004). In the marginal case, the Kondo temperature may have an additional logarithmic scaling with the coupling, upon implementation of an ultraviolet cutoff smoothly connected to the metallic case ($r = 0$) (Cassanello and Fradkin, 1996). Away from half-filling, there is a crossover to the usual Fermi-liquid case in the weak-coupling regime, $J_K < J_K^c$, where (Withoff and Fradkin, 1990)

$$T_K \approx \mu \exp[r^{-1}(D/\mu)^r(1 - J_K^c/J_K) - 1/r]. \tag{5.18}$$

Further studies based on NRG techniques (González-Buxton and Ingersent, 1998; Vojta, 2001; Fritz and Vojta, 2004) predicted a variety of fixed points. At half-filling, in the particle-hole symmetric case, $\varepsilon_0 = -U/2$, the Kondo problem has a metallic Kondo screened fixed point at $r = 0$, which evolves into a strong-coupling fixed point for $0 < r \leq 1/2$. In this case, the strong- ($J_K > J_K^c$) and weak-coupling ($J_K < J_K^c$) regimes are separated by a symmetric quantum critical point, whereas for $r > 1/2$ the local moment remains unscreened for all initial values of the Kondo coupling (Chen and Jayaprakash, 1995). In the particle-hole asymmetric case ($\mu = 0$, $U \neq -2\varepsilon_0$), for $r > r^* \approx 0.375$, the weak- and strong-coupling regimes are separated by an asymmetric critical point. For $r < r^*$, the particle-hole symmetry is dynamically restored (González-Buxton and Ingersent, 1998; Fritz and Vojta, 2004).

The phase diagram around the QCP is schematically shown in Fig. 26. The critical local moment fluctuations were studied by Ingersent and Si (2002), who found linear ω/T scaling of the dynamical spin susceptibility at the critical point for

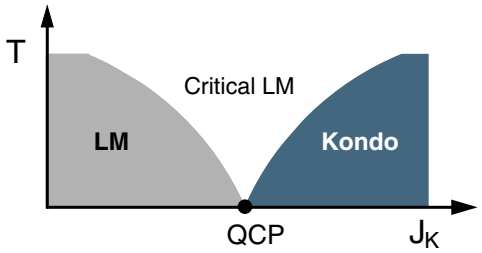

FIG. 26 (color online). Schematic phase diagram around the Kondo QCP at half-filling: temperature vs Kondo coupling. LM: local moment phase, where the Kondo cloud is suppressed. In the critical LM phase, quantum critical fluctuations dominate. From Ingersent and Si, 2002.

$0 < r < 1$. In the marginal case, $r = 1$, there are logarithmic corrections to scaling (Cassanello and Fradkin, 1997). The Kondo problem for gapless excitations was also extensively studied in the context of magnetic impurities in d-wave superconductors (Borkowski and Hirschfeld, 1992; Cassanello and Fradkin, 1996; Cassanello and Fradkin, 1997; Zhu and Ting, 2000; Polkovnikov, Vojta, and Sachdev, 2001; Vojta and Bulla, 2001; Zhang, Hu, and Yu, 2001; Polkovnikov, 2002). For a review, see Balatsky, Vekhter, and Zhu (2006).

In the graphene case, where $r = 1$, the Dirac fermions in the bath have an additional pseudospin structure, which motivated several proposals for multichannel Kondo physics (Cassanello and Fradkin, 1996; Sengupta and Baskaran, 2008; Dell'Anna, 2010; Zhu, Ding, and Berakdar, 2010). The Kondo resonance in graphene has been calculated with NRG by Cornaglia, Usaj, and Balseiro (2009). At half-filling, the local DOS around the impurity can be spontaneously enhanced by the formation of midgap states due to the scattering potential of the impurity (Hentschel and Guinea, 2007), frustrating the Kondo QCP.

At finite doping, the Kondo temperature has an exponential dependence with the DOS at weak coupling, allowing the Kondo cloud to be tuned by gating (Sengupta and Baskaran, 2008). In the crossover regime, at $J = J_c$, the scaling of the Kondo temperature with doping becomes power law, $T_K \propto |\mu|^x$. Recent NRG calculations in graphene have found a particle-hole asymmetric scaling of the Kondo temperature with doping, $T_K \propto |\mu|^x$, where $x = 1$ for $\mu > 0$ and $x = 2.6$ for $\mu < 0$ (Vojta, Fritz, and Bulla, 2010), in contradiction with the mean field and scaling analysis for the marginal case (Vojta, Fritz, and Bulla, 2010). In the presence of Landau level quantization, the Kondo temperature has reentrant behavior as a function of the chemical potential (Dora and Thalmeier, 2007).

Looking at the problem on the lattice, *ab initio* calculations on cobalt have found that the interplay of spin and orbital degrees of freedom can give rise to an SU(4) Kondo effect in graphene when the spin-orbit coupling is strong enough (Wehling, Balatsky, *et al.*, 2010). Another *ab initio* calculation accounting for dynamic correlations, also on Co, has identified the possibility of a spin $3/2$ Kondo effect, involving multiple orbitals (Jacob and Kotliar, 2010). From a tight-binding perspective, for a spin $1/2$ impurity, the hybridization Hamiltonian (5.14) can be written in the diagonal basis

$$\mathcal{H}_V = V \sum_{\alpha=\pm} \sum_{\mathbf{p},\sigma} [\Theta_{\alpha,\mathbf{p}} c^\dagger_{\alpha,\mathbf{p}\sigma} f_\sigma + \text{H.c.}], \tag{5.19}$$

where $c_{\pm,\mathbf{k}\sigma} = (1/\sqrt{2})[b_{\mathbf{k}\sigma} \pm (\phi^*_{\mathbf{k}}/|\phi_{\mathbf{k}}|) a_{\mathbf{k}\sigma}]$ are the fermionic operators that diagonalize the graphene Hamiltonian (2.2), $\phi_{\mathbf{k}} = \sum_{i=1}^{3} e^{i\mathbf{a}_i\cdot\mathbf{k}}$ is the tight-binding hopping matrix element defined by Eq. (2.3), and $\alpha = \pm$ labels the conduction and valence bands. Θ is a phase factor, which accounts for the symmetry and position of the localized orbital with respect to the sublattices (Uchoa *et al.*, 2009),

$$\Theta_{\alpha,\mathbf{p}} = \frac{1}{\sqrt{2}V}\left(V_{b,\mathbf{p}} + \alpha V^*_{a,\mathbf{p}} \frac{\phi^*_{\mathbf{p}}}{|\phi_{\mathbf{p}}|}\right), \tag{5.20}$$

where $V_{x,\mathbf{p}}$ is the hybridization as defined in Eq. (5.15).

As in metals, the Anderson Hamiltonian in graphene can be mapped into the spin exchange Hamiltonian by a canonical transformation (Schrieffer and Wolff, 1966). In the large U limit, the spin exchange Hamiltonian between the magnetic adatom and the graphene electrons is (Uchoa, Rappoport, and Castro Neto, 2011)

$$\mathcal{H}_e = -J \sum_{\mathbf{k}\mathbf{k}'} \sum_{\alpha\alpha'} \Theta^*_{\alpha,\mathbf{k}} \Theta_{\alpha',\mathbf{k}'} \mathbf{S}\cdot c^\dagger_{\alpha',\sigma',\mathbf{k}'} \boldsymbol{\sigma} c_{\alpha,\sigma,\mathbf{k}}, \tag{5.21}$$

where $\boldsymbol{\sigma} = (\sigma_1, \sigma_2, \sigma_3)$ are the Pauli matrices, $\mathbf{S} = \frac{1}{2} f^\dagger_\sigma \boldsymbol{\sigma} f_{\sigma'}$ is the localized spin, and

$$J(\mu) \approx \frac{V^2 U}{(\varepsilon_0 - \mu)(\varepsilon_0 + U - \mu)} < 0 \tag{5.22}$$

is the exchange coupling defined at the Fermi level, μ. Within the tight-binding description, we realize that the determinant of the exchange coupling matrix in Eq. (5.21) is identically zero, $\det[\hat{J}_{\alpha\alpha'}] \equiv 0$, and hence the exchange Hamiltonian (5.21) can be rotated into a new basis where one of the hybridization channels is decoupled from the bath (Pustilnik and Glazman, 2001). The eigenvalues in the new diagonal basis are $J_{u,\mathbf{k},\mathbf{k}'} = J\sum_\alpha \Theta^*_{\alpha,\mathbf{k}} \Theta_{\alpha,\mathbf{k}'}$ and $J_v = 0$, implying that the one-level exchange Hamiltonian (5.21) maps into the problem of a *single* channel Kondo Hamitonian, $\mathcal{H}_e = -2\sum_{\mathbf{k}} J_{u,\mathbf{k}\mathbf{k}'} \mathbf{S}\cdot\mathbf{s}_{\mathbf{k},\mathbf{k}'}$, where $\mathbf{s}$ is the itinerant spin, in spite of the implicit valley degeneracy. A multichannel description of the one-level problem is nevertheless possible, for example, in graphene quantum dots, in the continuum limit, where valley and angular momentum channels become good quantum numbers.

Unlike the situation in metals, the exchange coupling in graphene can be controlled by gating (Jacob and Kotliar, 2010; Uchoa, Rappoport, and Castro Neto, 2011), as shown in Fig. 27, in particular, when the chemical potential is brought to the proximity of the localized level, where the Kondo coupling becomes resonant. This effect opens the possibility of tuning J to the vicinity of the critical coupling that sets the crossover between the weak- and strong-coupling regimes. In this region, at finite doping, quantum criticality is reminiscent of the frustrated QCP at $\mu = 0$. Since the width of the Kondo peak in the spectral function is set by the Kondo temperature only, the gating effect permits measuring the quantum critical scaling of the Kondo temperature with doping (Vojta, Fritz, and Bulla, 2010; Uchoa, Rappoport, and Castro Neto, 2011) directly with STM probes (Uchoa *et al.*, 2009; Zhuang, Sun, and Xie, 2009; Saha, Paul, and Sengupta, 2010; Wehling, Dahal *et al.*, 2010).

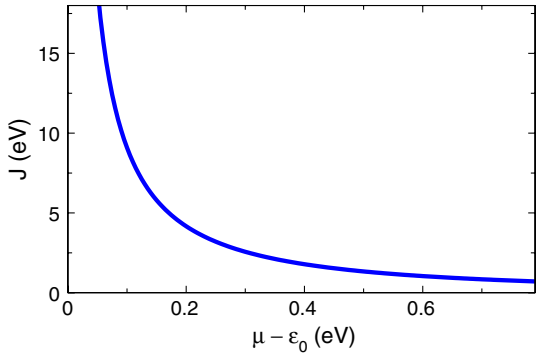

FIG. 27 (color online). Kondo coupling vs chemical potential in graphene for $U = 1$ eV and $V = 1$ eV. The Kondo coupling can be controlled by gate voltage across the weak ($J \ll J_c$) and strong coupling ($J \gtrsim J_c$) Kondo regimes, where J_c is the critical coupling at half-filling.

E. Ruderman-Kittel-Kasuya-Yosida interaction

The Ruderman-Kittel-Kasuya-Yosida (RKKY) interaction between two local spins is obtained by integrating out the itinerant fermions in Eq. (5.21), which gives $\mathcal{H}_{\text{RKKY}} = -J^2 \chi_{ij} \mathbf{S}_i \cdot \mathbf{S}_j$, where χ_{ij} is a two point correlation function, with i, j indexing the positions of the local spins. In momentum space (Brey, Fertig, and Das Sarma, 2007; Saremi, 2007; Uchoa, Rappoport, and Castro Neto, 2011),

$$\chi^{xy}(\mathbf{q}) = \sum_{\mathbf{k}\alpha\alpha'} \mathcal{M}^{xy}_{\alpha\alpha',\mathbf{k},\mathbf{q}} \frac{f[E_{\alpha'}(\mathbf{k}+\mathbf{q})] - f[E_\alpha(\mathbf{k})]}{E_\alpha(\mathbf{k}) - E_{\alpha'}(\mathbf{k}+\mathbf{q})}, \tag{5.23}$$

where (omitting the $\alpha\alpha'$ labels for simplicity)

$$\mathcal{M}^{xy}_{\mathbf{k},\mathbf{q}} = \Theta^{*x}_{\alpha,\mathbf{k}} \Theta^{y}_{\alpha,\mathbf{k}} \Theta^{x}_{\alpha',\mathbf{k}+\mathbf{q}} \Theta^{*y}_{\alpha',\mathbf{k}+\mathbf{q}}, \tag{5.24}$$

with $x, y = A, B, H, S$, etc., indexing the position of the spins on the lattice, $E_\alpha(\mathbf{k}) = \alpha|\phi_{\mathbf{k}}| - \mu$, and f is the Fermi distribution. $\mathcal{M}^{\text{AA}}_{\mathbf{k},\mathbf{q}} = \mathcal{M}^{\text{BB}}_{\mathbf{k},\mathbf{q}} = 1/4$ for spins on the same sublattice, whereas

$$\mathcal{M}^{\text{AB}}_{\mathbf{k},\mathbf{q}} = \frac{1}{4}\alpha\alpha' \frac{\phi_{\mathbf{k}}\phi^*_{\mathbf{k}+\mathbf{q}}}{|\phi_{\mathbf{k}}||\phi_{\mathbf{k}+\mathbf{q}}|} \tag{5.25}$$

for spins on opposite sublattices. In the continuum limit, where the spectrum is linearized around the Dirac points, $\mathcal{M}^{\text{AB}}_{\mathbf{k},\mathbf{q}} = \frac{1}{4}\alpha\alpha' e^{i\theta_{\mathbf{k},\mathbf{k}+\mathbf{q}}}$, where θ is the angle between $\mathbf{k}$ and $\mathbf{k}+\mathbf{q}$ (Brey, Fertig, and Das Sarma, 2007).

At half-filling, $k_F = 0$, the Fermi surface collapses into points and the RKKY interaction is mediated by interband transitions, which polarize the vacuum as in QED. In this case, the Friedel oscillations disappear and the sign of the interaction is ferromagnetic for spins on the same sublattice and antiferromagnetic for spins in opposite sublattices (Brey, Fertig, and Das Sarma, 2007; Saremi, 2007). In the overdoped regime, at $\mu = t$, the nesting among the Van Hove singularities in graphene reverses the sign of the RKKY interaction

compared to the $\mu = 0$ case (Uchoa, Rappoport, and Castro Neto, 2011).

At long distances, the spatial decay of the RKKY is r^{-3} when μ is at the neutrality point (Vozmediano *et al.*, 2005; Cheianov and Fal'ko, 2006; Brey, Fertig, and Das Sarma, 2007; Saremi, 2007; Wunsch *et al.*, 2006). Away from half-filling, the Friedel oscillations are restored by the intraband transitions and the RKKY interaction decays at $r \gg 1/k_F$ as $1/r^2$, similarly to the 2DEG case (Brey, Fertig, and Das Sarma, 2007; Wunsch *et al.*, 2006). For H or S site spins formed in C_{3v} symmetric orbitals, the RKKY interaction decays with a fast power law $1/r^7$ at half-filling (Uchoa, Rappoport, and Castro Neto, 2011). In carbon nanotubes, the RKKY interaction decays as $1/r$ for top carbon spins and as $1/r^5$ for H site spins in isotropic orbitals (Kirwan *et al.*, 2008).

When distributed regularly on top of graphene, magnetic adatoms such as hydrogen (H) can form macroscopic magnetic states at room temperature (Zhou *et al.*, 2009). In the disordered case, H atoms, in particular, can cluster on top of graphene due to rippling. On top of a ripple, the sp^2 carbon (C) bonds are spontaneously stretched by the curvature and acquire sp^3 character. Contrary to the perfectly flat case, the adsorption of H atoms on top of the hills helps to stabilize the ripples (Boukhvalov and Katsnelson, 2009). The interplay between the correlations due to the ripples and the RKKY interaction among the H spins can generate magnetoresistance hysteresis loops and a variety of magnetic spin textures (Rappoport, Uchoa, and Castro Neto, 2009).

F. Superconductivity

The observation of proximity induced superconductivity in graphene junctions has stirred much excitement in the field of mesoscopics (Heersche *et al.*, 2007). The Dirac nature of the quasiparticles gives rise to ballistic transport on a micron scale and allows graphene to sustain supercurrents in long junctions, the size of the coherence length in the superconducting metallic leads (Heersche *et al.*, 2007; Miao *et al.*, 2007; Du, Skachko, and Andrei, 2008; Ojeda-Aristizabal *et al.*, 2009). The experimental realization of the proximity effect motivated theoretical studies of the differential conductance in normal-superconductor interfaces, in graphene (Beenakker, 2006; Burset, Yeyati, and Martín-Rodero, 2008), in graphene nanoribbons (Rainis *et al.*, 2009), and in graphene normal-insulator-superconductor junctions (Bhattacharjee and Sengupta, 2006). Because of the Dirac nature of the spectrum, at half-filling, the Andreev conversion of an electron into a hole at the interface between a normal and a superconducting region involves specular reflection rather than retroreflection (Beenakker, 2006). The specular Andreev reflection leads to the presence of Andreev modes in superconductor-normal metal-superconductor (SNS) junctions that propagate along the graphene edges at the interface with the superconductor (Titov, Ossipov, and Beenakker, 2007). The Josephson current in graphene SNS junctions was studied by Titov and Beenakker (2006), followed by Moghaddam and Zareyan (2006), Maiti and Sengupta (2007), Black-Schaffer and Doniach (2008), and Bergman and Hur (2009). Possible applications involving the proximity effect in graphene include proposals for valley sensors (Akhmerov and Beenakker, 2007), current switches (Linder *et al.*, 2008; Lutchyn *et al.*, 2008), and a spin current filter (Greenbaum *et al.*, 2007). A review on Andreev and Klein tunneling processes in graphene can be found in Beenakker (2008).

These experimental developments in transport motivated a surge of interest in the possibility of making graphene an intrinsic superconductor. Graphene parent compounds, such as the graphite intercalated materials CaC_6 and KC_8, are low-temperature superconductors, although neither graphite nor alkaline metals alone superconduct (Hannay *et al.*, 1965; Csanyi *et al.*, 2005; Weller *et al.*, 2005). Even though intrinsic superconductivity has not been observed in the single layer so far, a few different superconducting mechanisms have been proposed. One possibility is a plasmon-mediated mechanism in graphene coated with metallic adatoms, in which the plasmons of the metallic band mediate the attraction between the graphene electrons (Uchoa and Castro Neto, 2007). When isolated islands of metallic atoms are adsorbed on top of graphene, superconductivity can also be induced by proximity effect (Feigel'man, Skvortov, and Tikhonov, 2009). Another possibility is the Kohn-Luttinger mechanism, which explores the proximity of the Fermi surface to the Van Hove singularities in the high doping regime (Kohn and Luttinger, 1965). In this scenario, the superconductivity can be mediated by a purely electronic mechanism, when the interactions become attractive along a specific direction of the BZ near the Van Hove singularity (González, 2008). The superconductivity can also be mediated by in plane or out of plane flexural phonons (Lozovik and Sokolik, 2010). In graphene, strong doping regimes can be currently achieved by chemical adsorption of alkaline metals, such as potassium (Uchoa, Lin, and Castro Neto, 2008; Grüneis *et al.*, 2009; McChesney *et al.*, 2010), or with metal contacts (Giovannetti *et al.*, 2008).

Alternative proposals include edge state superconductivity, induced by the large DOS at the edges (Sasakia *et al.*, 2007), or strong correlations, which so far have not been observed in graphene. As in the cuprates, the antiferromagnetic attraction between spin singlets on nearest neighbor sites has been proposed as a possible pairing channel in graphene, provided the on site Hubbard repulsion is strong enough to suppress the local fluctuations (Pathak, Shenoy, and Baskaran, 2010). González, Guinea, and Vozmediano (2001) considered the possible competition between ferromagnetic and superconducting states in graphene sheets through a renormalization group analysis accounting for Coulomb interactions. A recent functional renormalization group calculation has proposed the possibility of a strongly correlated SDW state that gives way to a singlet superconducting instability in the d-wave channel, or else a CDW solution that allows a triplet pairing instability in the f-wave channel (Honerkamp, 2008). In two-layer graphene, the possibility of excitonic pairing of electrons in one layer with holes in the other one has been considered (Kharitonov and Efetov, 2008; Min *et al.*, 2008).

Regardless of the microscopic origin, the superconducting state in graphene can be analyzed based on the symmetries of the order parameter in the honeycomb lattice. On the lattice,

the electrons in graphene carry spin, angular momentum, and sublattice quantum numbers. There are four possible pairing channels: singlet or triplet spin channels and same or opposite sublattices. In the singlet case, if we restrict the analysis to nearest neighbor site interactions only, two competing order parameters can be identified:

$$\Delta_0 = g_0\langle a_{i\uparrow}a_{j\downarrow}\rangle = g_0\langle b_{i\uparrow}b_{j\downarrow}\rangle, \tag{5.26}$$

which corresponds to an s-wave state, and Δ_1, defined as

$$\Delta_{1,ij} = g_1\langle a_{i\uparrow}b_{j\downarrow} - a_{i\downarrow}b_{j\uparrow}\rangle \tag{5.27}$$

for nearest neighbors and zero otherwise, where g_0 and g_1 are the coupling strengths. In momentum space, the latter state is described by

$$\Delta_{1,\mathbf{k}} = \sum_{i=1}^{3}\Delta_{1,i}e^{i\mathbf{a}_i\cdot\mathbf{k}}, \tag{5.28}$$

where $\Delta_{1,i} \equiv \Delta_1(\mathbf{a}_i)$ are the real space pairing amplitudes along the three different bond directions in the honeycomb lattice (see Fig. 28). In the simplest case, the pairing amplitudes are the same, $\Delta_{1,i} \equiv \Delta_1$, and Δ_1 is real, giving

$$\Delta_{1,\mathbf{k}} = \Delta_1\phi_{\mathbf{k}}, \tag{5.29}$$

where $\phi_{\mathbf{k}} = \sum_{i=1}^{3} e^{i\mathbf{k}\cdot\mathbf{a}_i}$ gives the hopping matrix element in the single-particle tight-binding spectrum (Uchoa and Castro Neto, 2007). This order parameter represents the pairing between electronic states in opposite sides of the BZ, and preserves all the physical symmetries of the honeycomb lattice, including point group and time-reversal symmetry $\Delta_{1,\mathbf{k}} = \Delta^*_{1,-\mathbf{k}}$, where the momentum $\mathbf{k}$ is measured with respect to the center of the BZ, at the Γ point. In real space, this order parameter (OP) has *extended* s-wave symmetry. If expanded around the Fermi surface centered at the Dirac point $\mathbf{K}$, from the perspective of the quasiparticle excitations near the Fermi level,

$$\Delta_{1,\mathbf{K}+\mathbf{p}} = \Delta_1 e^{i\theta}(p_x + ip_y) \tag{5.30}$$

describes a $p + ip$ state in one valley and $p - ip$ in the opposite one (Uchoa and Castro Neto, 2007). This state is therefore a $p + ip$ state with additional valley degeneracy. Unlike the case of conventional $p + ip$ superconductivity, the time-reversal operation involves an additional exchange of valleys, preserving the TRS of this state, and we refer to it as $p + ip$.

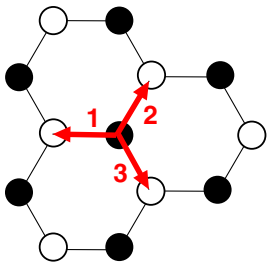

FIG. 28 (color online). Superconducting order parameter $\Delta_{1,j} = \Delta_1 e^{i\theta_j}$ ($j = 1, 2, 3$), with phases along the three different bond directions in the lattice.

Another possible paring symmetry is the state (Black-Schaffer and Doniach, 2007; Jiang *et al.*, 2008)

$$\Delta_{1,j} = \Delta_1 e^{i(2\pi/3)j}, \tag{5.31}$$

$j = 1, 2, 3$, which describes on the lattice a real space pairing wave function with $d_{x^2-y^2} + id_{xy}$ wave symmetry, breaking TRS. This broken symmetry is caused by the circulation of plaquette current loops, which amounts to global circulation of current along the edges. The low-energy description of this state around the Dirac points is a combination of s wave in one valley and $p + ip$ state in the opposite valley (Jiang *et al.*, 2008), as shown in Fig. 29. At the mean-field level, this state was shown to have lower energy than the pure $p + ip$ state (Black-Schaffer and Doniach, 2007). Because of the broken TRS, disorder and quantum fluctuations, which are paramount in a 2D system, may strongly inhibit the coherence of the $d + id$ state. Other alternatives are the degenerate states with $d_{x^2-y^2}$ and d_{xy} wave symmetries, represented by the $\Delta_{1,i}$ pairing amplitudes $(2, -1, -1)$ and $(0, 1, -1)$, respectively (Black-Schaffer and Doniach, 2007). These states conserve TRS but lower the crystal point group symmetry.

In the spin triplet channel, the OP is a superposition of $S_z = -1, 0, +1$ states. Since on-site pairing is forbidden by the Pauli principle, for nearest neighbors interaction the triplet superconducting states are $\Delta^t_{ij,\sigma\sigma} = \langle a_{i\sigma}b_{j\sigma}\rangle$, with $\sigma = \uparrow, \downarrow$ for $S_z = \pm 1$, and $\Delta^t_{0,\uparrow\downarrow} = \langle a_{i\uparrow}b_{j\downarrow} + a_{i\downarrow}b_{j\uparrow}\rangle$, in the $S_z = 0$ channel. The OP in this case is commonly defined as a 2×2 tensor,

$$\Delta_{ij} = i\sigma_2\boldsymbol{\sigma}\cdot\mathbf{d}_{ij}, \tag{5.32}$$

where the Pauli matrices act in spin space, and $\mathbf{d}_{ij} = -\mathbf{d}_{ji}$ is an antisymmetric tensor, violating parity. The case where the OP $\mathbf{d}$ has a single vector component describes the spinless fermionic case, discussed by Bergman and Hur (2009). The possibility of spin triplet states beyond nearest neighbors in the $S_z = 0$ channel was recently examined in a variational cluster approximation calculation (Sahebsara and Sénéchal, 2009). Another possibility is a Kekule superconducting state

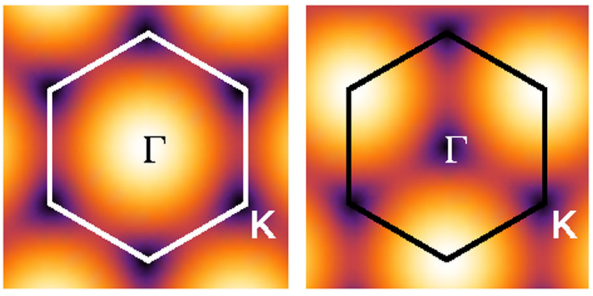

FIG. 29 (color online). Order parameter (OP) amplitude $|\Delta_{1,\mathbf{k}}|$ in the BZ: (left panel) $\Delta_{1,j} = \Delta_1$ with $j = 1, 2, 3$ indexing the three different bond directions of the crystal [see Eq. (5.28)] and (right panel) $\Delta_{1,j} = e^{i2\pi j/3}$, which describes a flux phase. Light colors represent higher amplitude. Dirac points are located at the K points, at the edges of the BZ. In all dark spots, the OP has $p + ip$ symmetry around the respective high symmetry points. In the three light spots on the right panel, the OP has s-wave symmetry around the K' points.

in the triplet channel, which breaks the translational symmetry of the lattice and allows the presence of topological excitations (Roy and Herbut, 2010).

At the level of nearest neighbor sites, the electron-electron interaction can be decomposed into an effective local Hubbard term,

$$\mathcal{H}_I^0 = \frac{g_0}{2}\sum_{i\sigma}(a_{i\sigma}^\dagger a_{i\sigma} a_{i-\sigma}^\dagger a_{i-\sigma} + b_{i\sigma}^\dagger b_{i\sigma} b_{i-\sigma}^\dagger b_{i-\sigma}), \tag{5.33}$$

and a nonlocal part,

$$\mathcal{H}_I^1 = g_1 \sum_{\langle ij\rangle}\sum_{\sigma\sigma'} a_{i\sigma}^\dagger a_{i\sigma} b_{j\sigma'}^\dagger b_{j\sigma'}. \tag{5.34}$$

In the singlet pairing channel, the nonlocal term can be decomposed into $\mathcal{H}_I^1 = g_1\sum_{\langle ij\rangle}(-\mathcal{B}_{ij}^\dagger\mathcal{B}_{ij} + \mathcal{D}_{ij}^\dagger\mathcal{D}_{ij})$, plus one body terms that can be absorbed into the chemical potential μ. $\mathcal{D}_{ij} = a_{i\uparrow}b_{j\downarrow} - a_{i\downarrow}b_{j\uparrow}$ is a standard singlet pair operator and $\mathcal{B}_{ij} = \sum_\sigma a_{i\sigma}^\dagger b_{j\sigma}$ is a bond operator. Decomposition of the interaction at the mean-field level with $\langle\mathcal{B}_{ij}\rangle = 0$ results in the graphene tight-binding Hamiltonian for the superconducting phase, $\mathcal{H}^s = \sum_{\mathbf{k}}\Psi_{\mathbf{k}}^\dagger\hat{\mathcal{H}}^s\Psi_{\mathbf{k}} + E_0$, where

$$E_0 = -|\Delta_0|^2/g_0 - 3\Delta_1^2/g_1, \tag{5.35}$$

and

$$\hat{\mathcal{H}}_{\mathbf{k}}^S = \begin{pmatrix} -\mu & -t\phi_{\mathbf{k}} & \Delta_0 & \Delta_{1,\mathbf{k}} \\ -t\phi_{\mathbf{k}}^* & -\mu & \Delta_{1,-\mathbf{k}} & \Delta_0 \\ \Delta_0^* & \Delta_{1,-\mathbf{k}}^* & \mu & t\phi_{\mathbf{k}} \\ \Delta_{1,\mathbf{k}}^* & \Delta_0^* & t\phi_{\mathbf{k}}^* & \mu \end{pmatrix} \tag{5.36}$$

is the Bogoliubov–de Gennes matrix written in the sublattice and Nambu basis $\Psi_{\mathbf{k}} = (a_{\mathbf{k}\uparrow}, b_{\mathbf{k}\uparrow}, a_{-\mathbf{k}\downarrow}^\dagger, b_{-\mathbf{k}\downarrow}^\dagger)$.

The Hamiltonian (5.36) can be diagonalized in a basis of Bogoliubov quasiparticles: $H^s = \sum_{\mathbf{k}\alpha s}E_{\mathbf{k},\alpha,s}\hat{n}^B_{\mathbf{k},\alpha,s} + E_0$, where $\hat{n}^B$ is the quasiparticle number operator and s, $\alpha = \pm 1$. In the isotropic case, $\Delta_{1,\mathbf{k}} = \Delta_1\phi_{\mathbf{k}}$, the spectrum is $E_{\mathbf{k},\alpha,s} = \alpha E_{\mathbf{k},s}$, with (Uchoa and Castro Neto, 2007)

$$E_{\mathbf{k},s} = \sqrt{(t|\phi_{\mathbf{k}}| + s\mu)^2 + (|\Delta_0| + s\Delta_1|\phi_{\mathbf{k}}|)^2}, \tag{5.37}$$

where the phase of the OP Δ_0 is locked in with Δ_1, and Δ_1 is real. The electronic gap described by the spectrum (5.37) is

$$E_g = 2|t\Delta_0 - \mu\Delta_1|/\sqrt{t^2 + \Delta_1^2}. \tag{5.38}$$

In the $p + ip$ state ($\Delta_0 = 0$, $\Delta_1 \neq 0$), E_g is proportional to the deviation of the chemical potential away from half-filling, and at $\mu = 0$ this state becomes quantum critical and gapless. The instability in this case translates into the renormalization of the Fermi velocity, where $\bar{t} = t\sqrt{1 + \Delta_1^2}$ is the renormalized hopping amplitude, instead of the opening of a gap (Uchoa and Castro Neto, 2007). Minimization of the free energy

$$F = -T\sum_{\mathbf{k},s}\ln[2 + 2\cosh(E_{\mathbf{k},s}/T)] + E_0 \tag{5.39}$$

with respect to Δ_0 and Δ_1 gives a set of two coupled BCS-like equations, and leads to the phase diagram shown in Fig. 30. At half-filling, $\mu = 0$, the emergence of superconductivity is controlled by quantum critical lines in the parameters g_0 and g_1, with critical values $g_0^c = -\pi v^2/D$ and $g_1^c = -4\pi v^4/D^3$, in the linear cone approximation, where D is an ultraviolet cutoff and v is the Fermi velocity near the Dirac point (Castro Neto, 2001; Marino and Nunes, 2006; Zhao and Paramekanti, 2006; Uchoa and Castro Neto, 2007). For finite μ, there is a crossover to the standard Fermi-liquid case at weak coupling, as shown in Fig. 30.

When $\Delta_{1,j} = \Delta_1 e^{i(2\pi/3)j}$ [see Eq. (5.28)], the electronic wave functions collect different phases along the different bond links, which gives rise to a current flow, and the $d + id$ state cannot coexist with an isotropic TRS s-wave state. The gap properties of the $d + id$ state and the differential conductance in SN junctions were derived by Jiang *et al.* (2008). The Josephson current for this state in SNS junctions was calculated by Linder *et al.* (2009).

In the s-wave state (we assume Δ_0 to be real), the gap variation with the coupling at half-filling, near the quantum critical point $g_0^c = -\pi v^2/D$, is (Castro Neto, 2001)

$$\Delta_0 = D(1 - g_0^c/g_0). \tag{5.40}$$

Away from half-filling, the gap crosses over to (Uchoa, Cabrera, and Castro Neto, 2005)

$$\Delta_0 = 2|\mu|\exp[D(1 - g_0^c/g_0)/|\mu| - 1] \tag{5.41}$$

for $|\mu| \gg \Delta_0$, which corresponds to the weak-coupling BCS limit, where $g \ll g_c$, as shown in Fig. 31. The $|\mu|/\Delta_0 \ll 1$ limit corresponds to the strong-coupling regime ($g > g_c$), and the intermediate coupling region near $g \sim g_c$ sets the crossover scale between the two regimes at finite μ. Nonequilibrium effects in the presence of a dissipative environment may also lead to a dissipation driven quantum phase transition away from half-filling (Takei and Kim, 2008).

At the mean-field level, the critical temperature at $\mu = 0$ is $T_c = \Delta_0/2\ln 4$, whereas in the opposite limit, $|\mu| \gg \Delta_0$, $T_c = \gamma\Delta_0/\pi$, as in the BCS case, where $\ln\gamma \approx 0.577$ is the Euler constant (Uchoa, Cabrera, and Castro Neto, 2005). Of course, in two dimensions there is no true long-range order. The superconducting transition is of Kosterlitz-Thouless (KT) type and coherence is actually lost at much lower temperatures due to the role of thermal fluctuations, which unbind vortex and antivortex pairs above the KT transition temperature, at $T_{\mathrm{KT}} < T_c$. The mean-field result indicates the

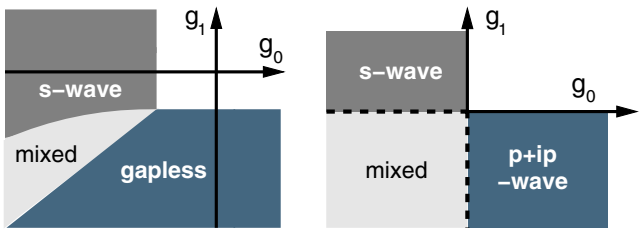

FIG. 30 (color online). Phase diagram between the s wave and effective $p + ip$ phases in the spin singlet channel. Left: $\mu = 0$ case, which is quantum critical. Right: $\mu \neq 0$ case. Continuous lines represent second order transitions, and dashed lines represent first order transitions. From Uchoa and Castro Neto, 2007.

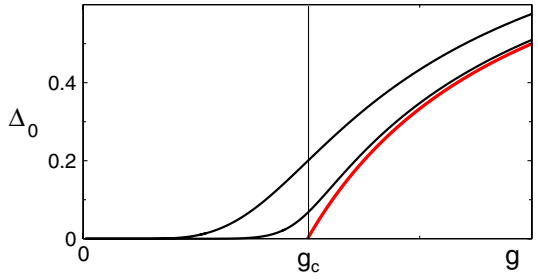

FIG. 31 (color online). Dependence of the gap, normalized by the band cutoff D, on g in the weak- ($g < g_c$) and strong-coupling ($g > g_c$) sectors for $\mu = 0$, $\mu/D = 0.1$ and 0.3. The value of μ decreases from the top to bottom curve.The model has a QCP at half-filling. From Uchoa, Cabrera, and Castro Neto, 2005.

onset of critical fluctuations where the amplitude of the Cooper pairs is completely destroyed, although the phase coherence is suppressed much earlier, at T_{KT}. The KT fluctuations of the superconducting order parameter have been considered by Loktev and Turkowski (2009), without accounting, nevertheless, for the chiral nature of the quasiparticles in graphene.

Zero field thermodynamic properties, such as the specific heat at fixed volume $C_V = -T(\partial^2 F/\partial T^2)_V$, can be extracted from the free energy (5.39). For an isotropic condensate of Dirac fermions, the jump of the specific heat at the phase transition, normalized by the specific heat on the normal side, is (Uchoa, Cabrera, and Castro Neto, 2005)

$$\delta C_V = 2(\ln 4)^2/9\zeta(3) \approx 0.35, \tag{5.42}$$

at half-filling. In the $|\mu|/\Delta_0 \gg 1$ limit, the jump grows to the standard BCS value $\delta C_V = 12/7\zeta(3) \approx 1.43$.

The Meissner effect in graphene, which describes the expulsion of an external magnetic field by the circulation of diamagnetic supercurrents, has been recently examined by Kopnin and Sonin (2008) and Uchoa and Castro Neto (2009). In the presence of vortices, the Bogoliubov–de Gennes equations for Dirac fermions in $2+1$ dimensions allow the presence of zero energy modes (Jackiw and Rossi, 1981) which are bound to the vortex cores. For a vortex with vorticity n (the winding number of the OP), $\Delta_0 = |\Delta_n(r)|e^{in\phi}$, with (r, ϕ) as cylindrical coordinates. The physical solutions allowed by the boundary conditions at the center of the vortex and at infinity result in n zero modes at half-filling (Ghaemi and Wilczek, 2012). The subgap spectrum and the wave functions in the vortex core have been derived by Seradjeh (2008) and Bergman and Hur (2009). Away from half-filling, for *odd* vorticity n, there is only one energy branch that crosses zero energy for zero angular momentum. For n *even*, no subgap branch intersects zero energy, and no exact zero modes exist (Bergman and Hur, 2009; Khaymovich *et al.*, 2009). Because of the fermionic degeneracy in the valleys, the topological zero modes do not lead to fractional statistics under vortex exchange, as in conventional $p+ip$ superconductors, unless additional interactions that lift the fermionic degeneracy are included (Herbut, 2010). Vortex zero modes for excitonic condensates in bilayers have been discussed by Seradjeh, Weber, and Franz (2008).

VI. INTERACTIONS AT BOUNDARIES AND LATTICE DEFECTS

A. Surface states

The vanishing density of states of graphene at the neutrality point implies that localized states can exist at the Dirac energy, much in the same way as localized states appear inside a forbidden energy gap in semiconductors and insulators. In order for these states to be normalizable, special boundary conditions are required. These conditions imply the breaking of the translational symmetry of the lattice, so that they can only exist near edges or defects.

The most extensively studied examples are the surface states which exist at graphene zigzag edges, where the lattice is abruptly terminated (Fujita *et al.*, 1996; Nakada *et al.*, 1996). Such edges have been observed in graphene flakes (Girit *et al.*, 2009; Jia *et al.*, 2009), and also in graphite (Niimi *et al.*, 2005). As the localized states form an energy band of zero width, the local density of states at the Dirac energy near a zigzag edge changes from zero to infinity, and the electron compressibility becomes divergent. Interactions of arbitrarily small strength lead to instabilities when the Fermi energy lies at the Dirac point. A mean-field analysis showed that a short-range Hubbard interaction can lead to a ferromagnetic ground state (Harigaya, 2001; Harigaya and Enoki, 2002). In zigzag ribbons with two edges, the spins at the two edges are aligned antiferromagnetically; see Fig. 32. These early theoretical results, based on the tight-binding approximation, were later confirmed by calculations based on the local density approximation (Son, Cohen, and Louie, 2006; Pisani *et al.*, 2007). The ferromagnetic order remained when the dangling bonds at the zigzag edges were saturated by hydrogen, which probably is closer to the actual experimental situation. The optimization of the atomic positions at the edges leads to reconstructed phases with gaps, where the spin up and spin down bands do not overlap near the gap, suggesting a half metallic phase (Son, Cohen, and Louie, 2006). Other phases with ferroelectric properties (Fernández-Rossier, 2008) or canted moments have been studied (Jung and MacDonald, 2010). A sketch of the magnetization induced near a zigzag edge of a graphene ribbon is shown in Fig. 32. Recent experiments (Enoki and Takai, 2009; Joly

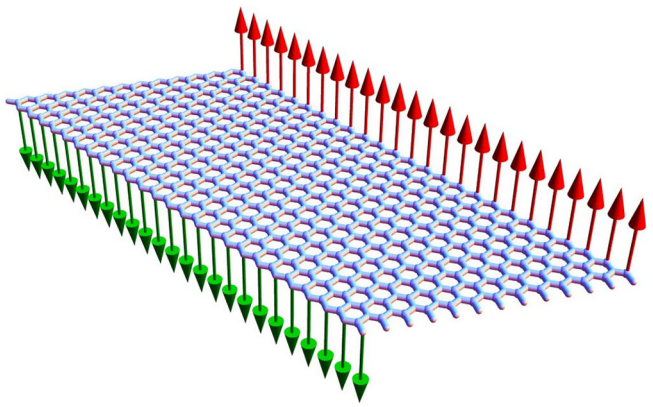

FIG. 32 (color online). Sketch of the magnetization at the zigzag edges of a graphene ribbon.

et al., 2010) confirm the existence of magnetic moments at graphene edges.

The effects of the electron-electron interaction on the midgap states have also been studied beyond the mean-field approximation. The calculations show that the ferromagnetic phase is stable when the band of localized states is half-filled. Both a local on-site interaction or the long-range exchange effect lead to this phase. At very low fillings, electrons tend to form a charge density wave state, similar to a Wigner crystal (Wunsch, Stauber, and Guinea, 2008; Wunsch *et al.*, 2008). More complex correlated states are possible at other fillings. The fact that the midgap states at a zigzag edge resemble the wave functions of Landau levels, in that the momentum parallel to the edge and the spatial extension are coupled, leads to the intriguing possibility of states similar to the Laughlin wave functions, which describe the fractional quantum Hall effect (Wunsch, Stauber, and Guinea, 2008).

At long distances, straight graphene edges of arbitrary orientation other than armchair can support midgap states, as zigzag edges (Akhmerov and Beenakker, 2008). Hence, local magnetic moments can be a generic property of abrupt graphene edges. Zigzag edges and vacancies in bilayer (Bernal) graphene also give rise to midgap states, at least when only the direct nearest neighbor interlayer hopping is included (Castro *et al.*, 2008a), and magnetic moments can be formed at the edges of bilayer graphene (Sahu *et al.*, 2008). Models which include other interlayer hoppings lead to sharp resonances near edges and vacancies. These results suggest that moderate interactions can produce local moments in graphene bilayers or in three-dimensional graphite. The combination of the Zeeman field associated with magnetic ordering and the spin-orbit coupling can lead to phases characterized by quantized spin currents at the edges (Soriano and Fernández-Rossier, 2010).

B. States at vacancies and cracks

Midgap states can occur in other situations where the translational symmetry of the lattice is broken. Similar to the case of surface states at a zigzag edge, interactions will lead to the spin polarization of these states. The simplest situation where the existence of a partially localized midgap state can be demonstrated is a lattice vacancy (Pereira *et al.*, 2006; Pereira, Lopes dos Santos, and Castro Neto, 2008). This analysis can be extended to multilayer samples (Castro, López-Sancho, and Vozmediano, 2010).

The existence of these states has been confirmed by STM spectroscopy on vacancies in irradiated graphite (Ugeda *et al.*, 2010). It can be expected that interactions lead to the formation of a magnetic moment around the vacancy. The formation of local moments near vacancies is consistent with the observation of ferromagnetism in irradiated graphite (Esquinazi *et al.*, 2003; Barzola-Quiquia *et al.*, 2007; Ohldag *et al.*, 2007; Ramos *et al.*, 2010; Chen *et al.*, 2011). Absorption of hydrogen leads to similar effects to those of a vacancy, including the formation of magnetic moments (Yazyev, 2008). Other dopants, such as carbon atoms and NO_2, also lead to the formation of spins (Lehtinen *et al.*, 2003; Wehling, Novoselov *et al.*, 2008).

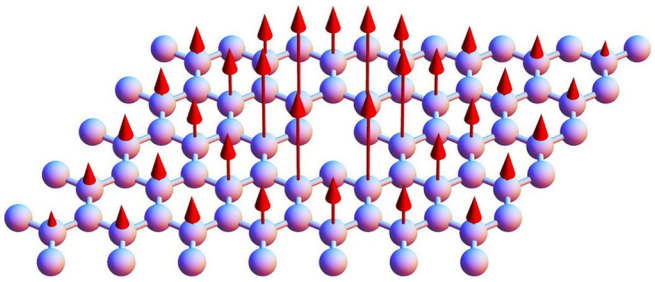

FIG. 33 (color online). Sketch of the magnetization induced near a vacancy.

A sketch of the magnetization induced near a graphene vacancy is shown in Fig. 33. The moment associated with the localized level around the vacancy is coupled to the extended states, leading to the possibility of the Kondo effect. Some differences between usual magnetic impurities and the situations described here can be expected: (i.) The vacancy or adatom modifies significantly the electronic density of states, rendering invalid perturbative treatments which relate the magnitude of the exchange coupling to the unperturbed electronic structure. The phase shift induced in the conduction band remains significant, even near the Dirac energy (Hentschel and Guinea, 2007). (ii.) The localized state is orthogonal to the extended states. Hence, the coupling between the local moment and the conduction band does not take place via virtual hops between the two types of states. Instead, it can be expected that the electron-electron interaction favors a ferromagnetic alignment of the local moment and the spins of the conduction electrons.

Spins at different vacancies interact ferromagnetically or antiferromagnetically (Brey, Fertig, and Das Sarma, 2007; Palacios, Fernández-Rossier, and Brey, 2008), depending on whether the vacancies occupy the same or different sublattices. At half-filling, the RKKY interaction mediated by the π band decays as $1/|\mathbf{r}-\mathbf{r}'|^3$, and it goes to the $1/|\mathbf{r}-\mathbf{r}'|^2$ dependence typical of a two-dimensional electron gas at finite carrier concentrations (Cheianov and Fal'ko, 2006). Voids or cracks can be considered an intermediate case between vacancies and edges (Vozmediano *et al.*, 2005). They also support localized spins at the boundaries.

C. Midgap states and random gauge fields

Midgap states in bulk graphene can also be induced by magnetic fields (see below), or by strains which mimic the effect of a magnetic field (Guinea, Katsnelson, and Vozmediano, 2008). These states have been analyzed using the tight-binding approximation (Guinea, Katsnelson, and Vozmediano, 2008), or by means of the local density functional method (Wehling, Balatsky *et al.*, 2008). Corrugations and wrinkles also induce midgap states in graphene (Katsnelson and Prokhorova, 2008; Pereira *et al.*, 2010). The presence of these states enhances the effects of the interactions. Mean-field calculations suggest the formation of magnetic moments, which will order ferromagnetically or antiferromagnetically (Guinea, Horowitz, and Doussal, 2008; Guinea, Katsnelson, and Vozmediano, 2008).

A random strain distribution leads to a random gauge field acting on the electrons. The changes in the electronic density of states induced by a random gauge field have been studied by RG techniques (Ludwig *et al.*, 1994; Horowitz and Doussal, 2002). Related problems arise at the transition between plateaus in the quantum Hall effect, and in d-wave superconductors. It can be shown that, above a certain disorder strength, a random gauge field leads to a divergent density of states at the Dirac energy (Riu and Hatsugai, 2001; Horowitz and Doussal, 2002). This divergence leads to a vanishing electron compressibility, and enhances the effects of interactions in the same way as the midgap states considered earlier. A random gauge field $\mathbf{A}(\mathbf{r})$ can be characterized by a dimensionless number Δ,

$$\langle A_\mu(\mathbf{r})A_\nu(\mathbf{r}')\rangle = \Delta\delta_{\mu\nu}\delta^{(2)}(\mathbf{r}-\mathbf{r}'). \tag{6.1}$$

If the gauge potential is assumed to arise from random corrugations of average height h and length ℓ, then $\Delta \sim h^4/a^2\ell^2$, where a is the lattice constant (Guinea, Horowitz, and Doussal, 2008; Guinea, Katsnelson, and Vozmediano, 2008). A similar parameter can be defined if the gauge potential is due to topological defects, such as dislocations (González, Guinea, and Vozmediano, 2001). The regime $\Delta \sim 1$ corresponds to ripples large enough to accommodate midgap states, leading to a divergence in the density of states. The changes in the density of states induced by a gauge field can be written as a logarithmic renormalization of the Fermi velocity

$$v \to v\left[1 - c\Delta \log\left(\frac{\Lambda}{|\mathbf{k}|}\right)\right], \tag{6.2}$$

where c is a numerical constant and Λ is a high momentum cutoff of the order of the inverse of the lattice constant.

The scaling towards lower Fermi velocities in Eq. (6.2) can be combined with the RG analysis of the long-range Coulomb interaction (Stauber, Guinea, and Vozmediano, 2005; Foster and Ludwig, 2006a, 2006b, 2008). Disorder tends to increase the density of states near the Dirac energy, while interactions lead to the opposite effect. To lowest order, this analysis leads to a line of fixed points characterized by a finite disorder and finite interactions, as discussed in Sec. III.A.1; see Fig. 9. The temperature and frequency dependence of properties such as the conductivity or the specific heat acquire anomalous exponents (Herbut, Juricic, and Vafek, 2008). For high disorder, $\Delta \gtrsim 1$, it can be shown that a gapped state is more stable than the gapless density of states expected in the absence of interaction effects (Guinea, Horowitz, and Doussal, 2008).

Certain strain configurations lead to effects similar to those induced by a constant magnetic field (Guinea, Katsnelson, and Geim, 2009). The possible ways in which the degeneracies of these states are lifted by the interactions have been studied (Herbut, 2008), and new phases with properties similar to those of topological insulators may exist. It is worth noting that STM experiments suggest the existence of very large effective fields due to strains, $B_{\text{eff}} \sim 300$ T, in small graphene bubbles under high strains (Levy *et al.*, 2010). The effects of electron-electron interactions in this regime remain unexplored.

VII. INTERACTION EFFECTS IN MESOSCOPIC SYSTEMS

A. Magnetism in quantum dots

Mesoscopic samples have a large ratio between the perimeter and the area. Midgap states localized at the edges can have a significant weight in the total density of states, and interaction effects are enhanced. Early calculations for planar carbon molecules (Stein and Brown, 1987; Tyutyulkov *et al.*, 1998) showed gaps associated with the electron-electron interaction, and magnetic moments at the edges. A large magnetic moment can be found in triangular graphene flakes (Fernández-Rossier and Palacios, 2007), where the three boundaries have the zigzag orientation, and the carbon atoms at the edges belong to the same sublattice.

As mentioned, edges of arbitrary orientations, except the armchair direction, support midgap states (Akhmerov and Beenakker, 2008). Hence, local moments and magnetism can be expected in graphene quantum dots of any shape, provided that the termination at the edges is abrupt. Model results suggest that this is the case, and the orientation of the moments at the edges depends on the type of sublattice at the edge (Fernández-Rossier and Palacios, 2007), as sketched in Fig. 34. Away from half-filling, correlated states with unsaturated magnetization and charge density wave states are also possible (Wunsch, Stauber, and Guinea, 2008; Romanovsky, Yannouleas, and Landman, 2009). The charging of a quantum dot leads to a substantial rearrangement of the electronic levels, in a similar way to the well studied orthogonality catastrophe in metals (Anderson, 1967; Wunsch, Stauber, and Guinea, 2008). The conductance can acquire a nontrivial voltage or temperature dependence, as in a Luttinger liquid (Kane and Fisher, 1992).

A simple estimate of the number of magnetic moments in a quantum dot can be obtained by assuming that the average density of edge states is of order $\rho_{\text{edge}} \approx c(R/aW)$, where $c \sim 1$ is a numerical constant, R is the radius of the dot, a is the lattice spacing, and W is the bandwidth of the band of

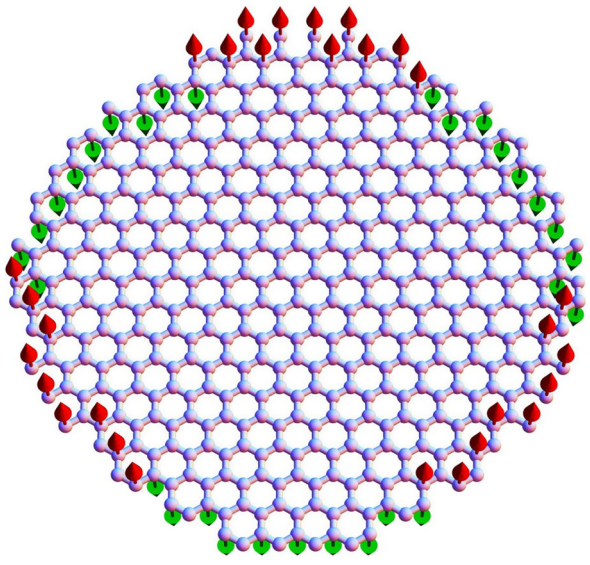

FIG. 34 (color online). Sketch of the magnetization induced at the edges of a quantum dot.

edge states (Wimmer, Akhmerov, and Guinea, 2010). The Coulomb interaction within each state which leads to the formation of local moments is $E_c \approx (e^2/R)\log(R/a)$; see below. Naturally, one has to replace $e^2 \to e^2/\epsilon_0$ in all formulas, but we do not write the dielectric constant explicitly in this section. The states which are spin polarized are those whose distance from the Fermi energy is less than E_c. This condition, combined with the estimate for ρ_{edge}, gives a maximum number of magnetic moments within the dot $N \approx E_c \rho_{\text{edge}} \approx c(e^2/aW)\log(R/a)$. This number is not too large. For $W \sim 0.3$–0.5 eV and $R \sim 100$ nm we obtain $N \sim 10$–20. The total magnetic moment of the dot depends on the sign of the couplings between the edge spins; see Fig. 34.

Experimentally, there is evidence which suggests the formation of local moments in small graphene flakes, of dimensions $10 - 50$ nm (Sepioni *et al.*, 2010).

B. Charging effects: Coulomb blockade

Graphene quantum dots of many shapes and dimensions have been extensively studied (Bunch *et al.*, 2005; Özyilmaz *et al.*, 2007; Avouris, Chen, and Perebeinos, 2007; Han *et al.*, 2007; Huard *et al.*, 2007; Williams, DiCarlo, and Marcus, 2007; Guettinger *et al.*, 2008; Ponomarenko *et al.*, 2008; Stampfer *et al.*, 2008; Güttinger *et al.*, 2009; Molitor, Droscher *et al.*, 2009; Moser and Bachtold, 2009). Single electron effects have been observed in many of them. Experiments show clear evidence of charging effects in graphene quantum dots, as evidenced in the diamond patterns formed by the resonances in the conductance through the dot as a function of gate and bias voltages (Guettinger *et al.*, 2008; Ponomarenko *et al.*, 2008; Stampfer *et al.*, 2008; Güttinger *et al.*, 2009; Molitor, Droscher *et al.*, 2009; Molitor, Jacobsen *et al.*, 2009; Moriyama *et al.*, 2009; Moser and Bachtold, 2009; Ritter and Lyding, 2009; Schnez *et al.*, 2009); see Fig. 35.

The electrostatic interaction between electrons leads to Coulomb blockade, which modulates the energy difference between levels, and induces non-Ohmic features in the conductance through the dot. In a graphene quantum dot of dimension R, the electrostatic energy required to add a unit of charge scales as e^2/R. The mean level spacing between extended states in a ballistic dot scales as v/R. As the dimensionless parameter $\alpha = e^2/\epsilon_0 v$ in graphene is of order unity, the energy scales associated with charging and confinement effects are comparable. The edge states discussed earlier can lead to charging energies larger than those for extended states. Assuming that these states are delocalized along the perimeter of the ribbon, over a scale $L \sim R$, see Fig. 36, and width a comparable to the lattice spacing, see Fig. 36, the charging energy becomes $(e^2/R)\log(R/a)$ (Wimmer, Akhmerov, and Guinea, 2010).

Charging effects can also modify the transport properties of narrow graphene ribbons. Irregularities in the edges may induce the formation of constrictions and quantum dots, as shown in Fig. 37, where charging effects will lead to a transport gap. In a nanoribbon of width W, the typical size of these dots will also be W, and the transport gap will be of order e^2/W. In the absence of charging effects, a ribbon

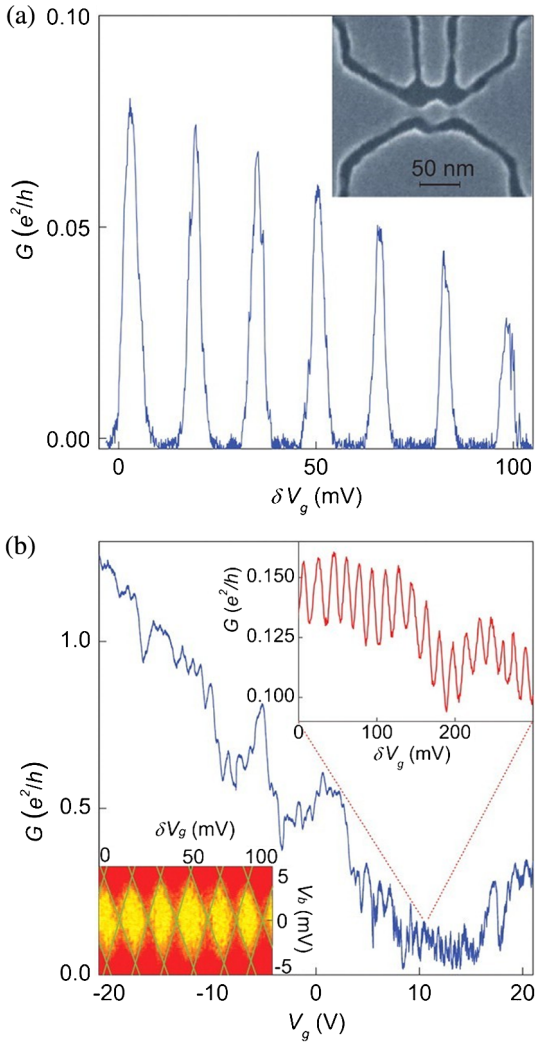

FIG. 35 (color online). Single energy peaks and Coulomb diamonds in a graphene quantum dot. From Ponomarenko *et al.*, 2008.

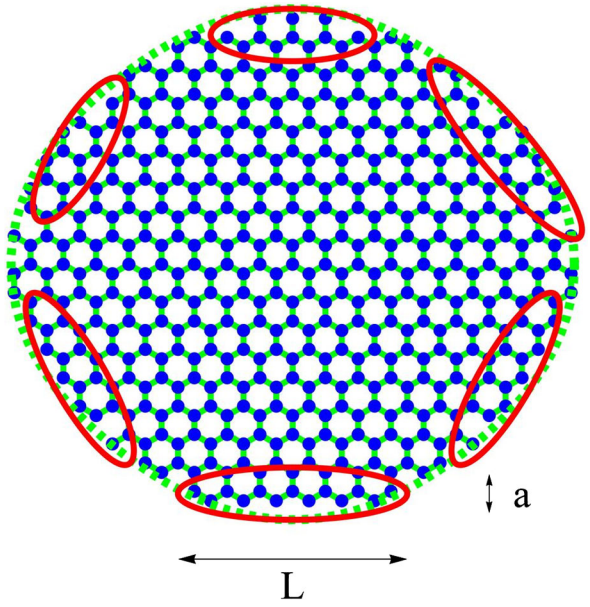

FIG. 36 (color online). Sketch of the extension of edge states in a graphene quantum dot.

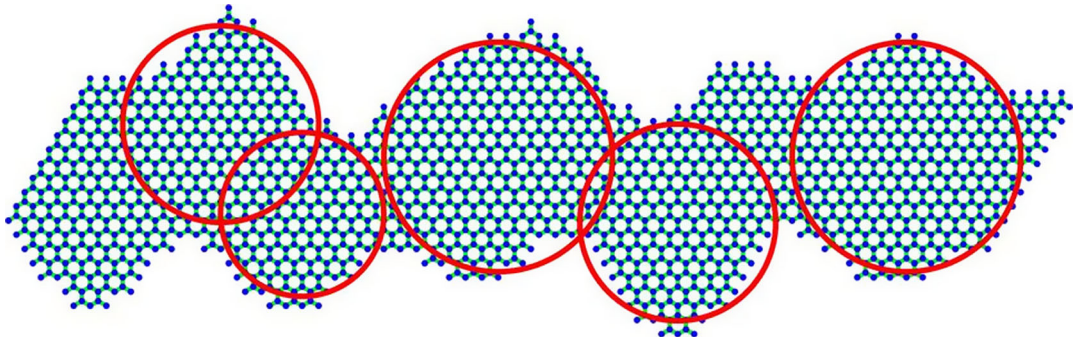

FIG. 37 (color online). Sketch of a graphene ribbon with disordered edges as a series of quantum dots.

will have confined subbands, separated by gaps of order v/W. Hence, the similarity between the energy scales arising from quantum confinement and charging effects, which exists in a quantum dot, also exists in a graphene ribbon. An experimental realization of an all graphene circuit with a point contact coupled to a quantum dot (Stampfer *et al.*, 2009) is shown in Fig. 38. This setup can be used to count the passage of charges through the quantum dot.

Experiments in graphene nanoribbons are compatible with the relevance of charging effects (Han *et al.*, 2007; Todd *et al.*, 2009; Han, Brant, and Kim, 2010). Some observations can be explained by a model of dots formed in the ribbon connected through many channels with the rest of the structure. Such a strongly coupled dot always shows Coulomb blockade effects, unless there is a perfect transmission through one or more of the channels. The effective charging energy, however, is strongly renormalized by the coupling between the dot and the rest of the system (Sols, Guinea, and Castro Neto, 2007) $E_c \approx e^2/We^{-g}$, where g is the conductance, in dimensionless units, of the junction between the dot and the electrodes. In general, $g \sim \langle|T|^2\rangle k_F W$, where T is the transmission amplitude of a given channel.

The electron-electron interactions can be studied in mesoscopic samples through their effect on the magnetoconductance at low magnetic fields. These experiments probe the phase coherence of electrons at low temperatures. This quantum effect is suppressed due to the dephasing induced by the interactions. Electronic quantum coherence also gives rise to the universal conductance fluctuations observed in disordered metals, which are also reduced by the dephasing due to interactions. The dephasing length shows a temperature dependence consistent with the expected behavior in a dirty metal $\ell_\phi \sim g\hbar v/T \log(g)$, where g is the conductivity in dimensionless units (Tikhonenko *et al.*, 2009) [see also Chen *et al.* (2010)]. This dependence is replaced by a $\ell_\phi \propto T^{-2}$ in high-mobility samples (Tikhonenko *et al.*, 2009), as expected in a clean Fermi liquid. Experiments that tune the ratio between the dephasing length and the mean free path (Moser *et al.*, 2010) show a variety of regimes, interpolating between weak and strong localization.

VIII. INTERACTIONS IN STRONG MAGNETIC FIELDS

A comprehensive review of graphene in magnetic field has recently appeared (Goerbig, 2011), and here we only mention some of the main effects. The electronic energy bands of graphene in a strong magnetic field collapse into Landau levels. In the absence of disorder, the electronic compressibility diverges when the chemical potential coincides with the

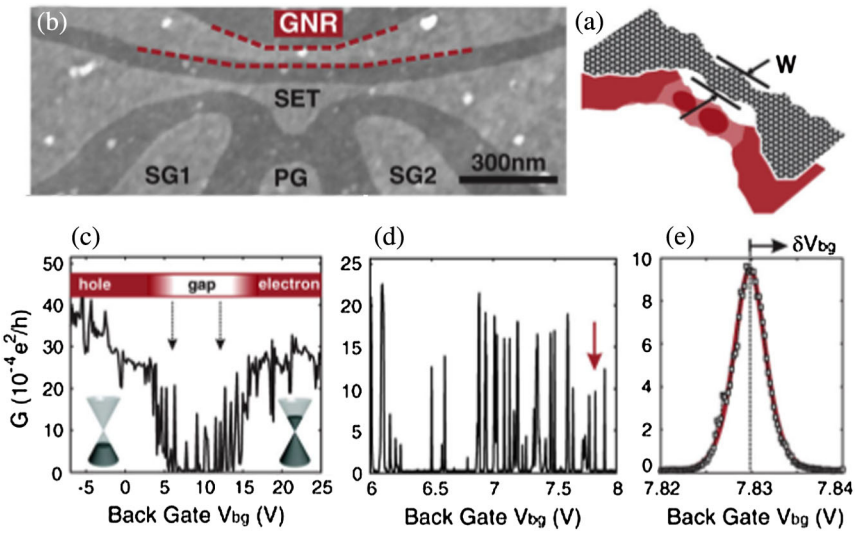

FIG. 38 (color online). Graphene point contact coupled to a quantum dot. From Stampfer *et al.*, 2009.

energy of a Landau level, and the effects of the interactions are enhanced, as in other two-dimensional metallic systems. The typical scale of the electronic wave functions is the magnetic length $\ell_B = \sqrt{\hbar/eB} = \sqrt{\Phi_0/2\pi B}$, where B is the applied field and Φ_0 is the quantum unit of flux. The separation between levels is of order v/ℓ_B, while the relevant scale for interaction effects is e^2/ℓ_B.

There are two sets of Landau levels in graphene, one for each valley. In addition, graphene has the $n = 0$ level, which combines electron and hole features. Hence, interactions can break either the valley degeneracy or the spin degeneracy. The long-range part of the Coulomb interaction is independent of the valley index. The $n = 0$ Landau level is localized in a given sublattice, and its degeneracy can be lifted by interactions which break the symmetry between sublattices, such as the coupling to out of plane optical phonons (Fuchs and Lederer, 2007). Hence, the removal of the spin and valley degeneracies of the Landau levels due to interactions depends on other energy scales (Goerbig, 2011), such as the Zeeman splitting, or the nearest neighbor repulsion, for the case $n = 0$. A sketch of the possible symmetry breaking patterns as a function of magnetic field is shown in Fig. 39. Early observations of splittings between Landau levels are shown in Fig. 40 [see Zhang *et al.* (2006)].

It is usually assumed that the Zeeman splitting is much smaller than the other energy scales. Calculations suggest that the spin degeneracy is lifted first, leading to excitations with combined spin and valley indices (Alicea and Fisher, 2006; Goerbig, Moessner, and Doucot, 2006; Nomura and MacDonald, 2006; Yang, Das Sarma, and MacDonald, 2006; Abanin *et al.*, 2007; Shibata and Nomura, 2008; Wang *et al.*, 2008; Gusynin *et al.*, 2009). The fourfold spin and valley degeneracy when the Zeeman coupling is neglected gives a new SU(4) symmetry, which may lead to new features, not observable in other two-dimensional electron gases (Goerbig and Regnault, 2007; Töke and Jain, 2007). The formation of Landau levels favors the excitonic transition which can also exist in the absence of a magnetic field (Gusynin *et al.*, 2006). The spin split $n = 0$ level leads to spin polarized edge states (Abanin, Lee, and Levitov, 2006; Fertig and Brey, 2006; Abanin *et al.*, 2007; Shimshoni, Fertig, and Pai, 2009) where the orientation of the spin depends on the sign of the current, as in topological insulators (Hasan and Kane, 2010; Qi and Zhang, 2011).

A magnetic field oriented parallel to the plane does not give rise to Landau levels. In neutral graphene, it leads to metallic states with electrons and holes polarized in opposite

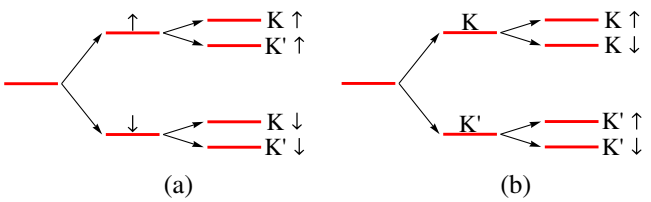

FIG. 39 (color online). Sketch of the successive splittings of the Landau levels as the magnetic field is increased. (a) Spin states are split first, and then the valley degeneracy is broken. (b) Valley degeneracy is lifted first, followed by the breaking of spin degeneracy.

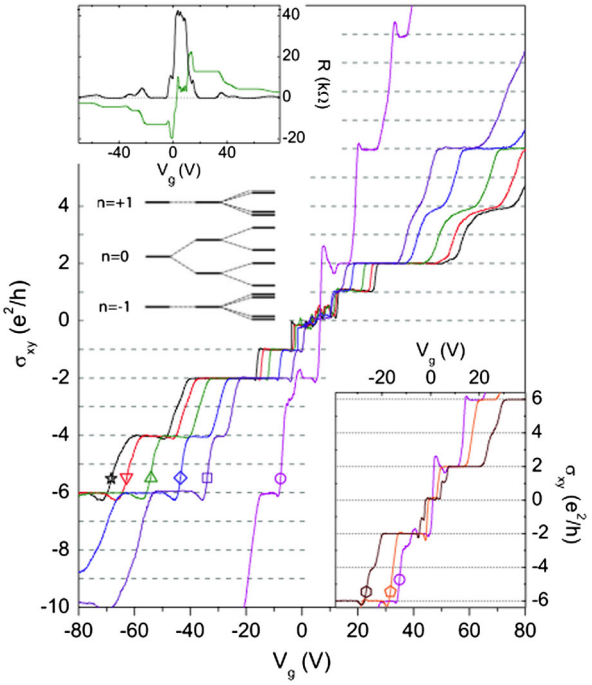

FIG. 40 (color online). Splittings of the Landau levels in graphene as function of magnetic field. From Zhang *et al.*, 2006.

directions, providing another route towards an excitonic transition (Aleiner, Kharzeev, and Tsvelik, 2007).

Experiments show that, indeed, the spin and valley degeneracies of Landau levels in graphene are lifted (Zhang *et al.*, 2006; Giesbers *et al.*, 2007; Jiang *et al.*, 2007; Giesbers *et al.*, 2009). The opening of a gap in the $n = 0$ level in graphene has been extensively studied, and a metal-insulator transition with critical features consistent with a Berezinskii-Kosterlitz-Thouless transition has been reported (Checkelsky, Li, and Ong, 2008; Checkelsky, Li, and Ong, 2009; Amado *et al.*, 2010).

The most striking manifestation of the interactions in the presence of a strong magnetic field is the fractional quantum Hall effect. Early theoretical calculations showed that the FQHE could be stable in graphene (Apalkov and Chakraborty, 2006; Castro Neto, Guinea, and Peres, 2006; Töke *et al.*, 2006). The conditions for the FQHE are the existence of sharp Landau levels and sufficiently strong electron-electron interactions. The analysis of FQHE states in graphene can be done in a similar way to that of a two-dimensional electron gas. The main difference is a change in the pseudopotentials which describe the interactions between electrons in a given Landau level, because the wave functions in graphene and in a two-dimensional electron gas differ.

This fractional quantum Hall effect was extensively, but unsuccessfully, sought in samples deposited on SiO_2. Suspended samples, which showed a much higher electron mobility, did not exhibit the FQHE, using the standard experimental four terminal setup. The observation of the integer quantum Hall effect in suspended bilayer graphene using a two terminal setup (Feldman, Martin, and Yacoby, 2009) led quickly to the discovery of the FQHE in single layer graphene (Bolotin *et al.*, 2009; Du *et al.*, 2009), using the same technique. More recently, four terminal measurements in

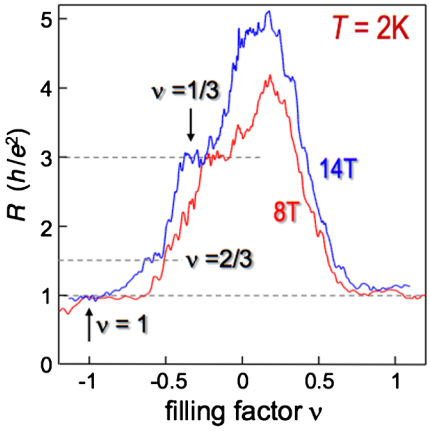

FIG. 41 (color online). Resistance of a suspended graphene sample as a function of carrier density for two different magnetic fields. From R. V. Gorbachev, D. C. Elias, A. S. Mayorov, A. A. Zhukov, K. S. Novoselov, and A. K. Geim, unpublished.

high-mobility suspended samples (Ghahari *et al.*, 2011), and also samples deposited on a new substrate, boron nitride (Dean *et al.*, 2010, 2011), also show the FQHE. In two terminal measurements, the existence of the FQHE is inferred from plateaus of the longitudinal resistance at carrier densities which correspond to fractional fillings of Landau levels; see Fig. 41. The $\nu = 1/3$ state turns out to be more robust than in other materials, such as GaAs, which exhibit the FQHE, and it can be observed at temperatures greater than 10 K. Fractional plateaus at $\nu = 2/3$ and $1/2$ have also been reported. Theoretical calculations suggest that the so-called Moore-Read ground state at fillings with even denominators, which leads to the existence of non-Abelian anyonic quasiparticles, is not favored in graphene (Wojs, Moller, and Cooper, 2011).

IX. INTERACTIONS IN BILAYERS

Bilayers are the building blocks for 3D stacks of graphene, such as graphite. In a bilayer one has two parallel graphene sheets, separated by an equilibrium distance similar to the interlayer distance of graphite (3.35 Å) (Dresselhaus and Dresselhaus, 1981). The relative position of the two graphene layers is not unique, and this leads to different stacking arrangements of the bilayer, and even more possibilities for multilayers, or graphite. The most stable configuration seems to be the so-called Bernal AB stacking, in which the two layers are rotated by 60°. As a consequence, one of the sublattices in the lower layer (say, sublattice A) is vertically aligned with one of the sublattices of the upper layer (say, sublattice B) [see Fig. 42(a)]. Note that this particular rotation leads to a breaking of sublattice symmetry between layers. As a first approximation, the electronic coupling between the layers can be described in terms of the hopping of electrons between the nearest neighbor atoms in different layers with an energy $t_\perp$ [also known as $\gamma_1 \approx 0.39$ eV in the graphite literature (Castro Neto *et al.*, 2009a]. Another possible arrangement between the layers is the fully aligned configuration, also called AA stacking. In both AB and AA stacking, the unit cell is comprised of 4 atoms, and has the same 2D

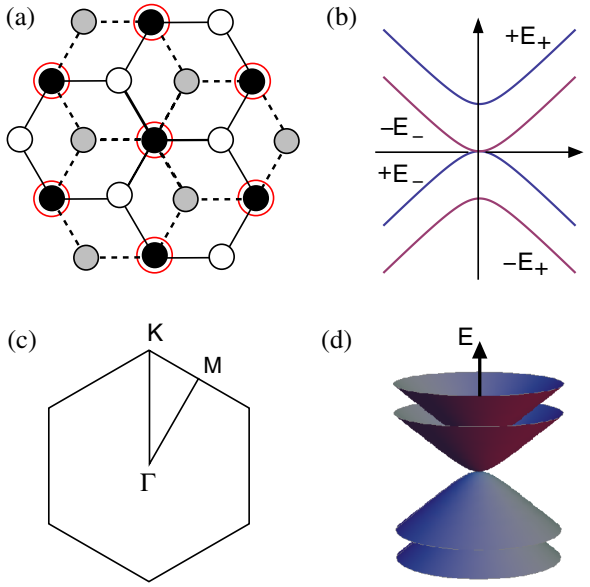

FIG. 42 (color online). (a) Top view of a graphene bilayer. White and solid black circles: top layer carbon atoms; gray and thin circles around the black ones: bottom layer. (b) Four-band spectrum of the bilayer $\pm E_\gamma(\mathbf{p})$, with $\gamma = \pm$ as shown in Eq. (9.4), near the corner of the Brillouin zone. (c) Brillouin zone with high symmetry points. (d) Illustration of the four-band spectrum around the K point.

extension as the unit cell of a single layer; this implies that the Brillouin zone is precisely the same as in monolayer graphene.

Note, however, that these configurations are just a few of an infinite series of commensurate structures between two layers, the so-called *twisted bilayer graphene* (Lopes dos Santos, Peres, and Castro Neto, 2007). The problem of commensurate and incommensurate structures always appears when two crystalline materials are superimposed, as in the case of bilayers. For commensurate structures, the angle between the layers is not arbitrary but follows a well-defined sequence (Lopes dos Santos, Peres, and Castro Neto, 2007). Obviously, different angles lead to different broken symmetries and hence to different electronic states. When the angle of rotation is 60°, as in the case of the Bernal structure, the sublattices are nonequivalent, which leads to a broken sublattice symmetry and hence to a putative gap opening. For other angles, there is no broken sublattice symmetry but the unit cell is enlarged as the rotation angle becomes smaller. In this case, the massless Dirac dispersion has to be preserved for symmetry reasons (Lopes dos Santos, Peres, and Castro Neto, 2007; Li *et al.*, 2009; Mele, 2010). From this perspective, the Bernal configuration is an exception. The twisted bilayer graphene presents a very rich physics of its own that we will not cover in this review. Instead, we focus on the Bernal configuration which is the most studied case.

We start from the minimal tight-binding model for Bernal bilayers, which includes a basis with two additional layer flavors (denoted by an overbar),

$$\Psi_{\mathbf{k},\sigma} = (a_{\mathbf{k},\sigma}, b_{\mathbf{k},\sigma}, \bar{b}_{\mathbf{k},\sigma}, \bar{a}_{\mathbf{k},\sigma}), \tag{9.1}$$

with $\sigma = \uparrow, \downarrow$ representing the spin. The resulting Bloch Hamiltonian is then a 4×4 matrix with two sublattice, and two-layer degrees of freedom,

$$\mathcal{H}_B = \sum_{\mathbf{k}\sigma} \Psi^\dagger_{\mathbf{k},\sigma} \begin{pmatrix} 0 & -t\phi_{\mathbf{k}} & -t_\perp & 0 \\ -t\phi^*_{\mathbf{k}} & 0 & 0 & 0 \\ -t_\perp & 0 & 0 & -t\phi^*_{\mathbf{k}} \\ 0 & 0 & -t\phi_{\mathbf{k}} & 0 \end{pmatrix} \Psi_{\mathbf{k},\sigma}, \tag{9.2}$$

where $t_\perp \approx 0.39$ eV is the interlayer hopping and $t \approx 2.8$ eV is the in-plane, nearest neighbor, hopping amplitude. The momentum dependence is contained in $\phi_{\boldsymbol{k}}$, which is the same as for a monolayer (2.3). The band structure associated with Eq. (9.2) consists of four nondegenerate bands given by

$$E(\boldsymbol{k}) = \pm\tfrac{1}{2}(t_\perp \pm \sqrt{t_\perp^2 + 4t^2|\phi_{\boldsymbol{k}}|^2}). \tag{9.3}$$

An expansion $\boldsymbol{k} = \boldsymbol{K} + \boldsymbol{p}$ around the $\boldsymbol{K}$ points of the BZ when $v|\mathbf{p}| \ll t$ shows that the four-band tight-binding spectrum (9.3) resolves into four hyperbolic bands (Nilsson *et al.*, 2006), as shown in Fig. 42(b), and whose form reads

$$\pm E_\gamma(\mathbf{p}) = \pm\frac{t_\perp}{2}[1 + \gamma\sqrt{1 + 4(v|\mathbf{p}|/t_\perp)^2}], \tag{9.4}$$

with $v \approx 6$ eV Å the Fermi velocity (the same Fermi velocity of a monolayer) and $\gamma = \pm 1$. The Bernal stacking explicitly breaks the sublattice symmetry in each layer, causing an energy split of $t_\perp$ between the two $\gamma = \pm 1$ branches E_+ and E_- at $p = 0$ (see Fig. 42). Because of a degeneracy at the K points, the two symmetric branches $+E_-$ and $-E_+$ touch there, resulting in a gapless spectrum. Just as in a monolayer, the Fermi surface of an undoped bilayer reduces to only two points, at K and K'; but now the valence and conduction bands have a finite curvature and, hence, notwithstanding the absence of a gap, the effective electronic degrees of freedom are massive, but still chiral. The degeneracy at K is protected by the Z_2 symmetry between the two layers only (McCann, 2006), and can be lifted with arbitrarily small perturbations, such as the ones induced by a bias voltage, by polarizing the two sheets (Zhang *et al.*, 2009), or else by independently changing the carrier concentration in each layer (Ohta *et al.*, 2006). This property opens the exciting prospect of using graphene bilayers as materials with a gate-tunable band gap (Castro Neto *et al.*, 2007; Castro *et al.*, 2007; Min *et al.*, 2007).

We stress that the low-energy effective theory of bilayers remains Lorentz invariant, in the following sense. The rotation of $\pi/3$ between layers breaks the sublattice symmetry leading to two pairs of massive Dirac particles at the K (K') point. Nevertheless, the system remains metallic because two bands, belonging to different pairs, touch at a point. More explicitly, the noninteracting bands (9.4) have the form

$$E_1(\boldsymbol{k}) = -E_-(\boldsymbol{k}) = -mv^2 + E(\boldsymbol{k}), \tag{9.5a}$$
$$E_2(\boldsymbol{k}) = +E_-(\boldsymbol{k}) = mv^2 - E(\boldsymbol{k}), \tag{9.5b}$$
$$E_3(\boldsymbol{k}) = +E_+(\boldsymbol{k}) = mv^2 + E(\boldsymbol{k}), \tag{9.5c}$$
$$E_4(\boldsymbol{k}) = -E_+(\boldsymbol{k}) = -mv^2 - E(\boldsymbol{k}), \tag{9.5d}$$

where $E(\boldsymbol{k}) = \sqrt{(mv^2)^2 + (vk)^2}$ and $m = t_\perp/(2v^2)$. Hence, $E_1(\boldsymbol{k})$ and $E_4(\boldsymbol{k})$ [or $E_2(\boldsymbol{k})$ and $E_3(\boldsymbol{k})$] describe a massive relativistic dispersion with rest energy given by mv^2. Again, the gapless nature of the full spectrum of this problem is due to an accidental degeneracy of the simplest tight-binding parametrization. Additional hopping terms (Castro Neto *et al.*, 2009a) in the Hamiltonian or many-body interactions can easily lift this degeneracy. This implies that the Bernal bilayer problem is unstable from the electronic point of view. In contrast, the twisted bilayer (Lopes dos Santos, Peres, and Castro Neto, 2007) is stable because it does not rely on this particular accidental degeneracy. Just as in the case of monolayer graphene, the introduction of the instantaneous Coulomb interaction does not preserve this Lorentz invariance.

At very low-energy, below $\Delta_w \approx 1.5$ meV, additional trigonal warping effects take place due to the influence of next-nearest-neighbor hopping matrix elements [which we neglect in Eq. (9.2)]. Trigonal warping introduces an asymmetry in the conductivity under electron or hole doping (Li *et al.*, 2009), and leads to a remarkable Lifshitz transition at low densities, whereby the lowest energy bands split into four Dirac cones (McCann and Fal'ko, 2006; Cserti, Csordás, and Dávid, 2007). These effects, however, happen at very low densities (around 1 electron per flake for typical 1 μm^2 samples), and hence are experimentally very challenging. A detailed description of the spectral properties of graphene bilayers can be found in Nilsson *et al.* (2008) and Castro Neto *et al.* (2009a).

When $\Delta_w < v|\mathbf{p}| \ll t_\perp$, we recover the so-called *classical limit* of the "relativistic" problem. This means that the presence of the uppermost band is not too relevant, and the energy disperses quadratically with momentum (the opposite limit of $v|\mathbf{p}| \gg t_\perp$ corresponds to the "ultrarelativistic" regime, where the band structure is essentially linear in momentum, as in the monolayer). In this case the Hamiltonian (9.2) near the K points can be projected onto an effective two-band model, written in terms of the two valleys and a mixed sublattice-layer basis (McCann and Fal'ko, 2006)

$$\tilde{\Psi}_{\mathbf{p},\sigma} = (a_{\mathbf{K}+\mathbf{p},\sigma}, \bar{b}_{\mathbf{K}+\mathbf{p},\sigma}, \bar{b}_{-\mathbf{K}+\mathbf{p},\sigma}, a_{-\mathbf{K}+\mathbf{p},\sigma}). \tag{9.6}$$

In such a basis, the effective kinetic Hamiltonian is

$$\mathcal{H}_B = \sum_{\mathbf{p}\sigma}\sum_{\alpha=\pm} \tilde{\Psi}^\dagger_{\mathbf{p},\sigma}\frac{p_\alpha^2}{2m}[\tau_0 \otimes \sigma_\alpha]\tilde{\Psi}_{\mathbf{p},\sigma}, \tag{9.7}$$

where $p_\pm = p_x \pm ip_y$, $\sigma_\pm = (\sigma_1 \pm i\sigma_2)/2$ operating in the sublattice basis, and τ operates in the valley space. The resulting energy spectrum is parabolic

$$E(\boldsymbol{p}) = \pm\frac{p^2}{2m}, \tag{9.8}$$

with $m = t_\perp/(2v^2) \approx 0.054m_e$ as the effective mass of the electron. From now on we omit the valley indexes and assume the two component basis $\tilde{\Psi}_{\mathbf{p},\sigma} \to (a_{\mathbf{p},\sigma}, \bar{b}_{\mathbf{p},\sigma})$ with a total degeneracy $N = 4$ in valley and spin.

The electronic Green's function in this two-band model $\hat{G}^{(0)}(\mathbf{k}, \tau) = -\langle T[\tilde{\Psi}_{\mathbf{k}}(\tau)\tilde{\Psi}^\dagger_{\mathbf{k}}(0)]\rangle$ is given by $\hat{G}^{(0)}(\mathbf{k}, i\omega) = (i\omega - \hat{\mathcal{H}}_B)^{-1}$ or, equivalently, by

$$\hat{G}^{(0)}(\mathbf{k}, i\omega) = \frac{1}{2}\sum_{s=\pm}\frac{1 + s\hat{\sigma}_{\mathbf{k}}}{i\omega - s|E(\mathbf{k})|} \tag{9.9}$$

in the chiral representation, where

$$\hat{\sigma}_{\mathbf{k}} = \sum_{\alpha=\pm} \frac{k_\alpha^2}{|\mathbf{k}|^2} \sigma_\alpha. \tag{9.10}$$

Although the fermions are chiral, in bilayers the wave functions of the quasiparticles acquire a 2π phase when winding around the K points, rather than a π phase as for Dirac fermions. This property is an admixture of the behavior of Dirac particles, which are chiral, with conventional electrons, which disperse quadratically. The combination of chirality and a trivial Berry phase has a clear experimental signature in the suppression of the zero-level plateau in the quantum Hall effect of the bilayer, whose plateaus are quantized by integer numbers (McCann and Fal'ko, 2006; Novoselov *et al.*, 2006).

A. Charge polarization

Within the two-band model, the one-loop polarization function has the generic form given in Eq. (2.12) for the single layer. The adaptations for the present case consist in considering the bilayer spectrum, and a new overlap factor, which, for the bilayer, reads

$$\mathcal{F}_{s,s',\mathbf{p},\mathbf{q}} = \tfrac{1}{2}[1 + ss' \cos(2\theta_{\mathbf{p},\mathbf{p}+\mathbf{q}})]. \tag{9.11}$$

In this expression $\theta_{\mathbf{p},\mathbf{p}+\mathbf{q}}$ is, again, the angle between the vectors $\mathbf{p}$ and $\mathbf{p}+\mathbf{q}$. Next we focus our discussion in terms of the effective two-band Hamiltonian (9.7) and dispersion (9.8).

The polarization function $\Pi^{(1)}(q,\omega)$ at finite density was obtained by Hwang and Das Sarma (2008a) in the $T=0$ static limit. The full dynamical case was calculated by Sensarma, Hwang, and Sarma (2010) at $T=0$, and by Lv and Wan (2010) at finite temperature. The finite density result can be obtained in closed analytical form for $T=0$; but, in order to avoid reproducing here those lengthy expressions, we simply present $\Pi^{(1)}(q,\omega)$ graphically in Figs. 1(a) and 1(b). The explicit form of the static limit reads (Hwang and Das Sarma, 2008a; Lv and Wan, 2010)

$$-\frac{\Pi^{(1)}(q,0)}{\rho(\mu)} = g\left(\frac{q}{k_F}\right) - f\left(\frac{q}{k_F}\right)\theta(q-2k_F) \tag{9.12}$$

at zero temperature, with

$$f(x) = \frac{2+x^2}{2x}\sqrt{x^2-4} + \ln\left(\frac{x-\sqrt{x^2-4}}{x+\sqrt{x^2-4}}\right) \tag{9.13a}$$

$$g(x) = \frac{1}{2}\sqrt{4+x^4} - \ln\left(\frac{2+\sqrt{4+x^4}}{4}\right). \tag{9.13b}$$

The DOS at the Fermi energy $\rho(\mu) = Nm/(2\pi)$ is constant and density independent, by virtue of the parabolic nature of the low-energy approximations (9.7) and (9.8) [note, however, that the consideration of the full four-band spectrum leads to a DOS which is linear in energy; in this sense, the correction to the DOS that arises from considering the four- versus the two-band model is not negligible (Ando, 2007)]. In this sense,

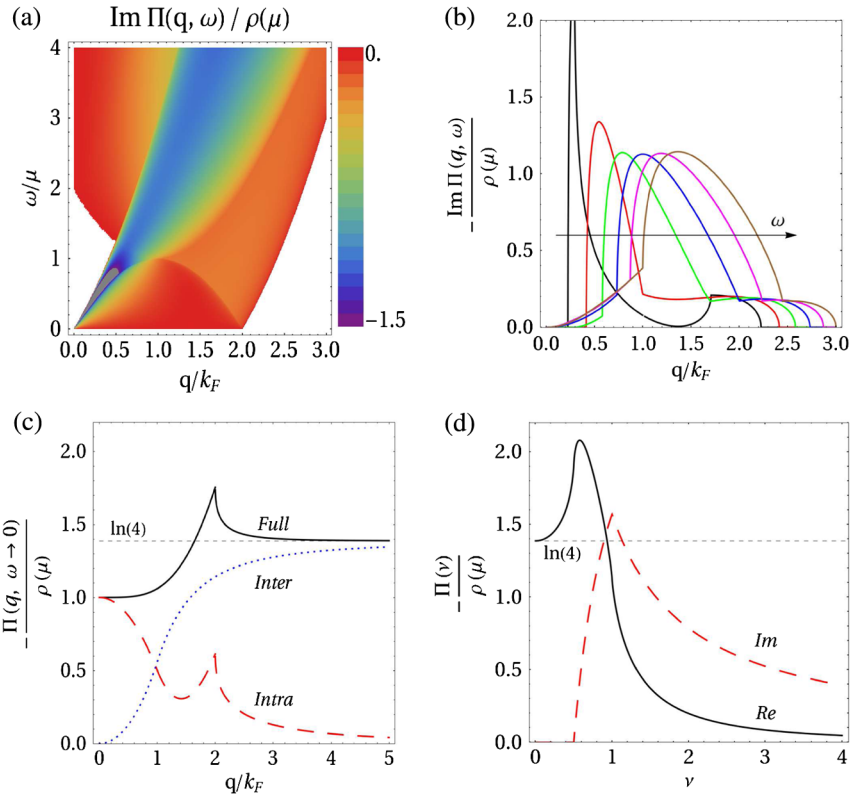

FIG. 43 (color online). The polarization $\Pi^{(1)}(q,\omega)$ of bilayer graphene, obtained within the two-band approximation, for finite chemical potential, and zero temperature. All panels are normalized to the DOS at the Fermi energy, μ. (a) Density plot of the imaginary part and, in (b) we have cuts of the same at constant frequency, for $\omega/\mu = 0.5, 1.0, 1.5, 2.0, 2.5, 3.0$. (c) The static limit $\Pi^{(1)}(q,0)$ in Eq. (9.12), and includes the intraband contribution (dashed), the interband contribution (dotted), and the full polarization (solid). (d) The real and imaginary parts of the polarization in the undoped case (9.14) as a function of $\nu = 2m\omega/q^2$.

the bilayer is similar to the conventional 2DEG. However, just as in the monolayer, the existence of two symmetric bands adds an interband channel, leading to a rather different quasiparticle spectrum, in comparison with the 2DEG. This can be seen by directly comparing Figs. 4(b) and 43(a). The behavior of $\Pi^{(1)}(q, 0)$ is shown in Fig. 43(c), together with its decomposition into intraband and interband contributions, which are, respectively, associated with the choice $ss' = 1$ and $ss' = -1$ in Eq. (9.11). As intuitively expected, the interband contribution dominates at large momenta and/or small densities, whereas the intraband transitions dominate the low momenta and/or large density regime. Unlike the monolayer, or the 2DEG, the polarization is constant for both $q \ll k_F$ and $q \gg k_F$. The former limit makes the bilayer similar to the conventional 2DEG and monolayer graphene, while the latter is neither akin to the 2DEG (for which the polarization decreases rapidly with q/k_F [Fig. 4(e)]) nor to the monolayer (for which it increases linearly [Fig. 3(e)]). Moreover, at precisely $q = 2k_F$, $\Pi^{(1)}(q, 0)$ is sharply cusped, which contrasts with the behavior of a monolayer, whose derivative is continuous. According to the standard theories of linear response, this feature at $2k_F$ has important implications for the behavior of the induced charge, the associated decay of the Friedel oscillations around charged impurities, the effective RKKY interaction among magnetic impurities, Kohn's anomaly in the phonon dispersion, etc. For example, one expects qualitative differences between the resistivity arising from Coulomb scattering in monolayer and bilayer graphene: it should be stronger in the bilayer, and have a more pronounced temperature dependence (Hwang and Das Sarma, 2008a; Lv and Wan, 2010).

At long wavelengths, the RPA screened potential reads $V^{\mathrm{RPA}}(q) = V(q)/[1 - V(q)\Pi^{(1)}(q)] \approx 2\pi e^2/\epsilon_0(q + q_{\mathrm{TF}})$, with a Thomas-Fermi momentum $q_{\mathrm{TF}} = Nme^2/\epsilon_0$. Note that q_{TF} is the same for the bilayer as in the 2DEG, i.e., it is constant (no density dependence), and also temperature independent (Lv and Wan, 2010). The temperature independence of q_{TF} at long wavelengths is another trait that distinguishes this system from both the monolayer and the 2DEG. In real space, the statically screened potential decays asymptotically as $V(r) \propto 1/r^3$ (Hwang and Das Sarma, 2008a).

At half-filling (undoped situation) and zero temperature, the form of the polarization bubble simplifies further, and can be cast as

$$\Pi^{(1)}(\nu) = -\frac{Nm}{2\pi}\left[\frac{1}{\nu}\ln\left(\frac{1+\nu}{1-\nu}\right) - \frac{1}{2\nu}\ln\left(\frac{1+2\nu}{1-2\nu}\right) + \ln\left(\frac{1-\nu^2}{\frac{1}{4}-\nu^2}\right)\right] \tag{9.14}$$

(Nilsson *et al.*, 2006; Barlas and Yang, 2009; Nandkishore and Levitov, 2010a), where $\nu = 2m\omega/q^2$ is the only scaling parameter. This function is plotted in Fig. 43(d). It follows at once that the static limit ($\omega \to 0$) is simply

$$\Pi^{(1)}(q, 0) = -\frac{N \ln 4}{2\pi} m, \tag{9.15}$$

consistent with the above discussion when $k_F = 0$. Despite the absence of a Fermi surface at half-filling, the Coulomb interaction among the quasiparticles is screened due to the finite density of states at the K points. However, an important difference here is that $\Pi^{(1)}(q, 0)$ is constant for all momenta, unlike traditional 2D systems, and stems from the presence of the interband channel. Hence, the Thomas-Fermi wave vector is exactly $q_{\mathrm{TF}} = Nm \ln(4) e^2/\epsilon_0$ for all wavelengths, and Friedel oscillations are suppressed at half-filling (Hwang and Das Sarma, 2008a). The additional numerical factor $\ln(4)$ means a slight increase in the screening strength of undoped bilayer, with respect to the doped situation. One way to interpret this $\ln(4)$ enhancement is the following: the factor Nme^2/ϵ_0, being exactly the same as in a simple 2DEG, is attributable to the finite DOS, while the extra $\ln(4)$ arises from the virtual interband transitions. In real space, the statically screened potential of undoped bilayer will decay as $1/r^3$, which contrasts with the corresponding behavior in the monolayer, where the decay is $1/r$ (as shown earlier this is due to the fact that, in the RPA, the effect of interactions in the monolayer is to simply renormalize the background dielectric constant, keeping the Coulomb form of the potential). Inspection of Fig. 43(d) reveals that the real part of the RPA dielectric function $\epsilon_{\mathrm{RPA}}(\mathbf{q}, \omega) = \epsilon_0[1 - V(\mathbf{q})\Pi^{(1)}(\mathbf{q}, \omega)]$ will be always nonzero. This means that, although the lack of a Fermi surface does not prevent screening in bilayers ($q_{\mathrm{TF}} \neq 0$), the formation of zero temperature infrared plasmons is suppressed at half-filling.

The screened Coulomb interaction between the layers is $V(q) = 2\pi e^2 e^{-qd}/\epsilon_0(q + q_{\mathrm{TF}} e^{-qd})$, where $d = 3.35$ Å is the interlayer distance. At long wavelengths, $q \ll t_\perp/v < 1/d \approx 0.3$ Å^{-1}, d can be effectively replaced by zero in a first approximation, and the screened interaction among electrons belonging to the same or different planes can be treated on the same footing.

We note that the behaviors discussed so far at large q have to be interpreted within the restrictions regarding the validity of the two-band approximation. For example, the fact that in Fig. 43(c) we see the polarization becoming constant at $q \gg k_F$ is an artifact of the two-band approximation. In reality, we should bear in mind that the full dispersion is hyperbolic, and hence becomes linear at high densities. We then expect to recover the linear-in-q dependence of $\Pi^{(1)}(q, 0)$ seen in Fig. 3(e) for the monolayer.

For this reason, proper caution is needed when considering the extrapolation of these results to highly doped bilayers, where the consideration of the four-band hyperbolic dispersion (9.4) is inevitably required. In terms of electronic densities, this corresponds to values above $\sim 10^{12}$ cm^{-2}, for which the two-band model is no longer warranted. The full dynamical response using the spectrum in Eq. (9.4) has been recently derived in closed analytical form by Borghi *et al.* (2009b). Notwithstanding the lengthy and cumbersome nature of these analytical results, they afford a more accurate perspective on the screening response of doped bilayer graphene, its collective modes, and the crossover between the regimes of a massive-chiral system at low densities, to a system of weekly coupled monolayers at higher densities. The approach of Borghi *et al.* (2009b) is ultimately limited by systems of such high densities that $\mu \approx t$, in which case the full tight-binding dispersion (9.3) is needed, but is beyond closed analytical approaches.

B. Quasiparticles

In the two-band model, the structure of perturbation theory for Coulomb interactions is set only by self-energy renormalizations in the effective mass of the electrons m and in the quasiparticle residue Z.

From the Hamiltonian (9.7), the renormalized Green's function is

$$\hat{G}(\mathbf{k},\omega)=\frac{1}{\omega-\sum_{\alpha=\pm}k_\alpha^2/(2m)\sigma_\alpha-\hat{\Sigma}(\mathbf{k},\omega)}. \tag{9.16}$$

$\hat{\Sigma}(\mathbf{k},\omega)$ is the quasiparticle self-energy correction, which is described in the $(a_{\mathbf{k},\sigma},\bar{b}_{\mathbf{k},\sigma})$ basis by a matrix of the form

$$\hat{\Sigma}=\begin{pmatrix}\Sigma_0 & \Sigma_+\\ \Sigma_- & \Sigma_0\end{pmatrix}, \tag{9.17}$$

or, equivalently, $\hat{\Sigma}=\Sigma_0\sigma_0+\Sigma_+\sigma_++\Sigma_-\sigma_-$, where $\sigma_\pm=(\sigma_x\pm i\sigma_y)/2$. By symmetry, $\Sigma_+=\Sigma_-^*$. In a more conventional form,

$$\hat{G}(\mathbf{k},\omega)=\frac{Z}{\omega-Z\sum_{\alpha=\pm}[k_\alpha^2/(2m)+\Sigma_\alpha]\sigma_\alpha}, \tag{9.18}$$

where $Z^{-1}=1-\partial\Sigma_0/\partial\omega$ corresponds to the quasiparticle residue and

$$\frac{m^*}{m}=\frac{1-\partial\Sigma_0/\partial\omega}{1+2m\partial\Sigma_+/\partial k_+^2} \tag{9.19}$$

is the mass renormalization.

We saw in the previous section that, unlike the monolayer, Coulomb interactions in the bilayer are screened. The self-energy is given in terms of the bare Green's function and the RPA effective interaction by

$$\hat{\Sigma}^{(1)}(\mathbf{q},\omega)=i\int\frac{d^2kd\varepsilon}{(2\pi)^3}V^{\mathrm{RPA}}(\mathbf{k},\varepsilon)\hat{G}^{(0)}(\mathbf{k}+\mathbf{q},\varepsilon+\omega), \tag{9.20}$$

where $V^{\mathrm{RPA}}(\mathbf{q},\omega)=V(\mathbf{q})/\epsilon_{\mathrm{RPA}}(\mathbf{q},\omega)$ is dressed by the RPA dielectric function. Even if the ratio between the Coulomb and kinetic energies diverges in the low-density limit (as in a 2DEG), the validity of RPA can be, in principle, justified in the large N limit. If only static screening is taken into account (Hartree-Fock-Thomas-Fermi theory), the self-energy is frequency independent and, to leading order, the quasiparticle residue Z does not renormalize. Calculations based on the static screening picture for the two-band model (Borghi *et al.*, 2009a), and also for the four-band model (Kusminskiy *et al.*, 2009), found mass renormalization in the bilayer. The mass decreases ($m^*/m<1$) and the renormalization grows stronger as the screening is suppressed. In Fig. 44 we show this renormalization within the two-band model, where the parameter λ interpolates between the Thomas-Fermi screened potential ($\lambda=1$) and the unscreened Coulomb potential ($\lambda\approx 0$). As a consequence of the reduced mass, the charge compressibility is also expected to decrease (Kusminskiy *et al.*, 2008; Borghi *et al.*, 2010).

More recent calculations that account for the full dynamical screening found quite different results. When the dynamical RPA polarization bubble, Eq. (9.14), is taken into account, the self-energy exhibits a strong $\ln^2$ leading divergence $\mathrm{Re}\Sigma_+^{(1)}(k.\omega)=(2k_+^2/Nm\pi^2)\ln^2(\Lambda/k)$ and $\mathrm{Re}\Sigma_0^{(1)}(k,\omega)=(-4\omega/N\pi^2)\ln^2(\Lambda/\sqrt{m\omega})$, at small energies and momenta (Barlas and Yang, 2009). The ultraviolet momentum scale $\Lambda\sim q_{\mathrm{TF}}$ is related to the effective "Bohr radius," $a_0=\epsilon_0/me^2$, and we set $\Lambda=1/a_0$. At leading ($\ln^2$) order, the two terms in the self-energy compensate each other exactly in Eq. (9.19) and the mass does not renormalize, $m^*/m\to 1$ at $k\to 0$, while the quasiparticle spectral weight vanishes as $Z\sim\ln^{-2}(\Lambda/k)$. The RG analysis of the dynamically screened interaction at large N was carried out by Nandkishore and Levitov (2010c), where subleading (single log) contributions were collected. These were found to cause a (weak) increase of the effective mass $m^*/m\approx 1+(0.56/N2\pi\ln 4)\ln\Lambda$, and consequently an increase of the compressibility.

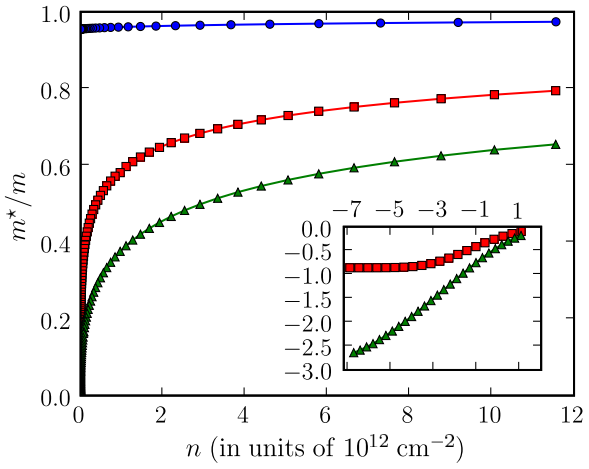

FIG. 44 (color online). Mass renormalization for $\alpha=0.5$ in the bilayer, calculated with a *static* Thomas-Fermi screened Coulomb interaction $V(q)=e^2/\epsilon_0(q+\lambda q_{\mathrm{TF}})$, as a function of the electronic density. Circles: $\lambda=1$; squares: $\lambda=0.01$; triangles: $\lambda=10^{-4}$. The inset shows $\log_{10}(m^*/m)$ as a function of $\log_{10}(n)$ for two of the λ values; the mass saturates at a finite value for $n\to 0$. From Borghi *et al.*, 2009a.

Once again, the validity of a two-band model rests on the assumption that all relevant energy scales are small compared to $t_\perp\approx 0.4$ eV. However, the Coulomb energy Λ_E on the scale of $a_0=\epsilon_0/me^2$ is substantial for not too strong dielectric screening $\Lambda_E=e^2/\epsilon_0 a_0\approx 1.47/\epsilon_0^2$ eV (Nandkishore and Levitov, 2010a; 2010c). Hence, Coulomb interactions can promote electronic transitions among the four bands, while the two-band model is only justified in the limit $\Lambda_E<t_\perp$. To what extent the two-band model provides a valid description of the quasiparticles in the presence of Coulomb interactions is a matter of ongoing discussion.

C. Many-body instabilities

The finite DOS in the bilayer enhances the possibility of many-body instabilities in comparison with the single layer case. For instance, the spin polarization tensor in the bilayer is defined in leading order by Eq. (5.4), with the matrix element $\hat{\mathcal{A}}^s(\mathbf{k})=1+s\sum_{\alpha=\pm}(k_\alpha^2/\mathbf{k}^2)\sigma_\alpha$. In matrix form,

$$\hat{\Pi}^{(1)+-} = \begin{pmatrix} \Pi^{(1)+-}_{aa} & \Pi^{(1)+-}_{ab} \\ \Pi^{(1)+-}_{ba} & \Pi^{(1)+-}_{bb} \end{pmatrix}, \tag{9.21}$$

which leads to one ferromagnetic and one antiferromagnetic eigenstate, $\Pi_{F/\mathrm{AF}} = \Pi_{aa} \pm |\Pi_{ab}|$, by symmetry under exchange of the a and b labels. In bilayers the AF state has a leading logarithmic divergence with the cutoff Λ at zero frequency and magnetic field (Nilsson *et al.*, 2006),

$$\Pi^{(1)}_{\mathrm{AF}}(\mathbf{q}, 0) = \frac{m}{\pi} \ln\left(\frac{2\Lambda}{|\mathbf{q}|}\right), \tag{9.22}$$

suggesting (within RPA) a tendency towards an AF instability for any value of the Hubbard interaction U. In addition, at finite U, a first order ferromagnetic transition can be driven by the Stoner criterion, leading to a ferromagnetoelectric state where the layers have different magnetization and polarized charge (Castro *et al.*, 2008b).

Other possibilities include the emergence of CDW instabilities induced by the short-range part of the Coulomb interaction (Dahal *et al.*, 2010) or else an excitonic instability at strong local electronic repulsion (Dillenschneider and Han, 2008). With long-range Coulomb interactions, the inverse electronic compressibility κ^{-1} becomes negative at small densities (Kusminskiy *et al.*, 2008), indicating a tendency to Wigner crystallization (Dahal *et al.*, 2006), which is compensated by the positive compressibility of the lattice.

Bilayers share similar features with one-dimensional (1D) electron systems, such as the pointlike Fermi surfaces and the parabolic spectrum. In particular, in biased bilayers the 1D interface between biased regions confines chiral modes that propagate as in a strongly interacting Luttinger liquid (Killi *et al.*, 2010). This affords the possibility of studying such interacting models experimentally in appropriately prepared samples of bilayer graphene.

For short-ranged interactions in 2D, the structure of the diagrams in bilayers and in 1D electron liquids is quite similar, although the diagrams compensate each other in a rather different way. The dimensionless coupling which determines the strength of the interactions is Ua^2m, where U is the strength of the local interactions and a is the lattice constant. Perturbative renormalization group calculations in the bilayer have identified distinct leading instabilities of the electron gas. For different choices of possible interactions, two different low-temperature broken symmetry phases have been found: in one case, a ferroelectric gapped phase (Zhang *et al.*, 2010) induced by the coupling between the different layers; in the other, a nematic phase (Vafek, 2010; Vafek and Yang, 2010), where each Fermi point splits into two Dirac points.

The possibility of an excitonic instability has been also predicted by Nandkishore and Levitov (2010a), who found that the dynamically screened Coulomb interaction gives rise to a ferroelectric state that polarizes the two layers. In the ferroelectric state, the kinetic energy inflicts an energy cost $\delta E_{\mathrm{Kinetic}} \propto \Delta^2 \ln(\Lambda_E/\Delta)$, where Δ is the energy gap. Finite separation between the layers generates an additional electrostatic energy cost to polarize the charge between the layers, which dominates the kinetic energy at the Hartree level $\delta E_{\mathrm{Hartree}} \propto \Delta^2 \ln^2(\Lambda_E/\Delta)$ (McCann, Abergel, and Falko, 2007). The excitonic instability is induced by the exchange term, which is parametrically larger than the Hartree term by the factor a_0/d, where d is the interlayer distance (Nandkishore and Levitov, 2010a). The existence of a ferroelectric state has nevertheless been disputed by independent RG calculations that also accounted for the dynamically screened Coulomb interactions and infrared trigonal warping effects (Lemonik *et al.*, 2010). The spontaneous symmetry breaking found in this work leads to a Lifshitz transition consistent with the nematic state found by Vafek and Yang (2010), rather than the opening of a gap.

In the quantum Hall (QH) state, two terminal measurements of the conductivity in clean suspended samples found an insulating state at the $\nu = 0$ filling factor (Feldman, Martin, and Yacoby, 2009), rather than the metallic QH state previously found in supported samples (Novoselov *et al.*, 2006). Further theoretical works predicted the possibility of a zero field excitonic QH state, which spontaneously breaks time-reversal symmetry, and can evolve into a ferromagnetic QH state at finite magnetic field (Nandkishore and Levitov, 2010b). In biased bilayers, a chiral anomaly has been predicted in the quantized Hall effect, splitting the degeneracy of valley quantum numbers (Nakamura, Castro, and Dora, 2009). Another predicted effect resulting from interactions in the QH state is the formation of charge $2e$ skyrmions at even filling factors (Abanin, Parameswaran, and Sondhi, 2009).

X. CONCLUSIONS

As we have seen, the understanding of the many-body problem in graphene has evolved quite rapidly in only a few years. The case of monolayer graphene in the weak-coupling regime (which means graphene embedded in an environment with large dielectric constant) is quite clear, namely, although Lorentz invariance is explicitly broken because of the Coulomb interactions, the effective low-energy theory is still Lorentz invariant with well-defined quasiparticles. Nevertheless, these quasiparticles have a renormalized *speed of light* that grows logarithmically in the infrared, while their spectral weight decreases slowly in the same limit. This situation can be contrasted with the conventional Fermi-liquid picture where all physical constants (the so-called Landau parameters) and spectral weight are finite in the infrared (that is, at the Fermi surface). Hence, these logarithmic renormalizations are weak enough, even in the presence of strong Coulomb interactions, and a *Dirac liquid* picture is preserved.

In the strong-coupling regime (that is, graphene in vacuum), many-body instabilities are possible albeit depending on a delicate balance of energy scales. This occurs because the renormalizations of quasiparticle properties also depend on details of the cutoff procedure in the ultraviolet (as shown by the f-sum rule). While mean-field theories predicted instabilities towards phases with broken chiral symmetry and superconducting quasi-long-range order (because of the 2D nature of the material), and earlier Monte Carlo studies on a hypercubic lattice suggest the presence of instabilities (Drut and Lähde, 2009a, 2009b, 2009c), simulations of interacting electrons on the honeycomb lattice have still to be performed in order to address these issues, since the strong-coupling

regime cannot be reached by perturbative methods. This remains, currently, as an important open problem in many-body graphene physics.

The Coulomb impurity problem in graphene shares many of the issues of the many-body problem but can be studied in much more detail because the 2D hydrogen problem in graphene was solved exactly. In the weak-coupling regime (the so-called undercritical regime), the Coulomb interaction between a localized charge and the electrons leads to only mild changes in the physical properties due to the explicitly broken particle-hole symmetry. In the strong-coupling (or supercritical) regime, the situation is rather different because of the phenomenon of *fall to the center*, that is, the electron states become unstable, with the generation of resonances near the Dirac point. Just as the many-body problem, the critical local charge depends on the dielectric environment, and in vacuum this effect should be observed by local probes even for a single proton sitting on the graphene surface. So far, there is no experimental evidence of such effect, given that it is difficult to study adatoms in suspended samples with local probes, such as scanning tunneling microscopes. In supported samples, because of dielectric screening that brings the system to weak coupling, and of the disorder in the substrate, the study of this problem can be much more elusive.

In analogy to the 2DEG problem, the effect of disorder is rather strong in graphene which again is the effect of dimensionality. The low dimensionality implies strong quantum fluctuations that can easily couple to spatial variations of random scalar (chemical potential) and gauge (hopping) fields. Strong localization is the ultimate fate of any disordered two-dimensional system but because the localization length grows very slowly in the infrared limit, the finite size of the samples, or the finite temperature of the system, ends up cutting off the tendency towards Anderson localization and, in practical terms, graphene behaves in a metallic way.

The problem of magnetism of adatoms in graphene is rather different from the one found in metallic hosts. Because of the strong energy dependence of the density of states (that vanishes at the Dirac point), the Anderson impurity problem has features that are unique. In analogy with the strong-coupling regime in the many-body and Coulomb impurity problems, the results are sensitive to the ultraviolet regularization. In fact, this is a generic feature of the Dirac spectrum, namely, strong coupling leads to spectral weight transfer from high energies to low energies, that is, to the Dirac point (as discussed in the context of the f-sum rule). Moreover, the damping by Dirac electrons leads to an anomalously large (and strongly energy dependent) broadening of the adatom energy level. This leads to an unusual situation as compared to the Anderson impurity problem in a metal, namely, that even when the chemical potential is above (below) the energy of the doubly (singly) occupied state, a magnetic moment can emerge. Hence, adatoms that may not be magnetic in a metal (hydrogen or fluorine, for instance) might become magnetic in graphene.

On the other hand, the Kondo effect that usually suppresses the appearance of magnetic moments in metals because of magnetic ''screening'' (the ultimate consequence of the so-called ''Kondo cloud'') is strongly suppressed in graphene. This suppression has its roots in the low density of states and the sublattice structure. In fact, there is a strong dependence of the hybridization with the position on the lattice (whether it breaks or not the sublattice symmetry). Furthermore, the Kondo effect is very dependent on the chemical potential (that can be easily tuned in graphene by gating). This state of affairs reinforces the conclusion that magnetic states of adatoms could be more the norm than the exception in graphene, in much contrast with the situation in ordinary metals. Experimentally, there are few studies of the magnetism of adatoms in graphene. The main problem here is that most of the experiments done so far are in electronic transport. Just as the Kondo problem in metals and semiconductors, the observation of magnetic effects in transport is rather subtle, and requires careful analysis. Currently, this is a rather open field in graphene physics.

A superconducting state in graphene would have dramatic consequences given its low dimensionality and unusual electronic spectrum. While true long-range order would not be possible because of its 2D nature, quasi-long-range order would have unusual consequences. For one, because of the sublattice structure, there is room for exotic pairing states with even more exotic vortex excitations. The phase space for pairing is rather large due to the spin, sublattice, and valley degeneracies. However, the low density of states plays a deleterious role here. One way out of this conundrum would be the enhancement of the density of states by either gating or doping with adatoms. These two techniques have their own limitations. Gating is limited by the distance from the gate to the graphene sample, and by the dielectric breakdown of the spacer that separates the two. Doping inevitably introduces disorder, or can modify the electronic structure of the π band too much leading to extrinsic effects. There are, however, serious hopes that come from the fact that intercalated graphite can be made to superconduct. An obvious idea would be intercalation of Ca or Yb in the graphene bilayer. So far, intercalation experiments in bilayers have not been performed, and little is known about how to intercalate atoms or molecules in such systems. Again, this is very much an open field of research.

In addition to the dielectric environment, which has a strong influence on many-body effects in bulk graphene, finite-size effects are also of great importance. It has been understood early on that zigzag edges are strongly interacting because of the high density of states they create at the Dirac point. Systems with high density of states are prone to many-body states due to Stoner-like instabilities. However, the many-body physics of finite 2D systems is even more sensitive to disorder (either in the bulk or in the edge) because of the strong boundary condition dependence. In graphene, this problem is magnified because the electronic wave functions associated with impurity states do not decay exponentially, as they would in a semiconductor with a finite gap, or would be extended, as in a normal metal, but they are quasilocalized (that is, decay as a power law). This implies that evanescent waves play an important role in determining the physical properties. Experiments in mesoscopic graphene samples show very clearly these effects through strong oscillations of the electronic conductance and the presence of Coulomb blockade peaks. From a theoretical perspective, such

problems are probably the hardest to solve because they involve the direct interplay between Anderson localization and interactions. Thus, a deeper understanding of mesoscopic graphene systems is still necessary, and this topic would merit a review of its own.

Magnetic fields also lead to spatial localization due to the presence of Landau levels with a length scale given by the cyclotron length. Hence, this problem shares many of the difficulties of the previous problems with the added complication that the 2D nature of graphene brings a large degeneracy into play. Once again, the detailed balance between kinetic and Coulomb energies, and the details in the ultraviolet, determine the fate of the many-body ground state. The fractional quantum Hall effect was only observed recently in suspended two-probe experiments (Du *et al.*, 2009), and very little is known about the sequence of FQHE fractions and their nature. It is believed that magnetic fields can generate a plethora of new many-body states, with symmetries that are rather different from the ones found in the 2DEG. But, compared to the 2DEG problem, this field is still in its infancy.

While we demonstrated the complexity of the many-body problem in monolayer graphene, we have not even touched beyond the surface of the many-body problem in bilayer graphene. There is no doubt, at least from a theoretical perspective, that the many-body problem in the bilayer is much richer than in the monolayer. The bilayer has a finite density of states at neutrality, making it similar to the 2DEG problem. However, unlike the 2DEG, the graphene bilayer is a Lorentz invariant system with a finite ''rest mass'' (that is, it has a hyperbolic dispersion relation) albeit with an accidental degeneracy that makes it a semimetal (two of the four bands touch at the Dirac point). This accidental degeneracy can be lifted easily by hopping or interactions, leading to a large number of possible many-body states with different quantum numbers. Given this richness, one can say that bilayer graphene is the ultimate target of many-body theorists in this field. However, it is technically a major challenge given the high dimensionality of the problem, with its 2^4-dimensional spinorial structure (spin, valley, sublattice, and plane). Moreover, from an experimental perspective many details and conditions are still quite uncontrolled, which has led to a few contradictory results, and has so far yielded more questions than answers. In fact, both theoretically and experimentally, the graphene bilayer remains very much an open problem. If we now extrapolate from the monolayer to the bilayer, we see that there are problems that have not even been addressed theoretically and experimentally, such as the Anderson impurity problem, or the Kondo effect in bilayers, the problem of magnetism, and superconductivity, just to mention some. These are topics for the future, for future generations of physicists to address and marvel.

ACKNOWLEDGMENTS

We are indebted to our collaborators, friends, and colleagues for their many invaluable contributions, discussions, comments, and suggestions. In particular, we want to explicitly thank E. Andrei, Y. Barlas, S. Das Sarma, V. Fal'ko, M. M. Fogler, E. Fradkin, A. Geim, M. Goerbig, J. Gonzalez, I. Herbut, M. I. Katsnelson, P. Kim, A. Lanzara, J. Lopes dos Santos, A. MacDonald, E. Mucciolo, J. Nilsson, K. Novoselov, N. Peres, S. Sachdev, O. Sushkov, O. Vafek, S. Viola, M. A. H. Vozmediano, and A. Yacoby. A. H. C. N. acknowledges DOE Grant No. DE-FG02-08ER46512 and ONR Grant No. MURI N00014-09-1-1063. B. U. acknowledges partial support from DOE Grant No. DE-FG02-91ER45439 at the University of Illinois. F. G. acknowledges financial support by MICINN (Spain) through Grants No. FIS2008-00124 and CONSOLIDER CSD2007-00010, and by the Comunidad de Madrid, through NANOBIOMAG. V. N. K. acknowledges the financial support of the University of Vermont.

REFERENCES

Abanin, D. A., P. A. Lee, and L. S. Levitov, 2006, Phys. Rev. Lett. **96**, 176803.
Abanin, D. A., K. S. Novoselov, U. Zeitler, P. A. Lee, A. K. Geim, and L. S. Levitov, 2007, Phys. Rev. Lett. **98**, 196806.
Abanin, D. A., S. A. Parameswaran, and S. L. Sondhi, 2009, Phys. Rev. Lett. **103**, 076802.
Abergel, D. S. L., P. Pietiläinen, and T. Chakraborty, 2009, Phys. Rev. B **80**, 081408.
Abramowitz, M., and I. A. Stegun, 1964, *Handbook of Mathematical Functions* (Dover, New York).
Abrikosov, A. A., and S. D. Beneslavskii, 1971, Sov. Phys. JETP **32**, 699.
Adam, S., E. H. Hwang, V. M. Galitski, and S. Das Sarma, 2007, Proc. Natl. Acad. Sci. U.S.A. **104**, 18392.
Akhmerov, A. R., and C. W. J. Beenakker, 2007, Phys. Rev. Lett. **98**, 157003.
Akhmerov, A. R., and C. W. J. Beenakker, 2008, Phys. Rev. B **77**, 085423.
Aleiner, I. L., and K. B. Efetov, 2006, Phys. Rev. Lett. **97**, 236801.
Aleiner, I. L., D. E. Kharzeev, and A. M. Tsvelik, 2007, Phys. Rev. B **76**, 195415.
Alicea, J., and M. P. Fisher, 2006, Phys. Rev. B **74**, 075422.
Amado, M., E. Diez, D. López-Romero, F. Rossella, J. M. Caridad, V. Bellani, and D. K. Maude, 2010, New J. Phys. **12**, 053004.
Anderson, P. W., 1961, Phys. Rev. **124**, 41.
Anderson, P. W., 1967, Phys. Rev. Lett. **18**, 1049.
Ando, T., 2006, J. Phys. Soc. Jpn. **75**, 074716.
Ando, T., 2007, J. Phys. Soc. Jpn. **76**, 104711.
Ando, T., A. B. Fowler, and F. Stern, 1982, Rev. Mod. Phys. **54**, 437.
Apalkov, V. M., and T. Chakraborty, 2006, Phys. Rev. Lett. **97**, 126801.
Appelquist, T. W., M. Bostwick, D. Karabali, and L. C. R. Wijewardhana, 1986, Phys. Rev. D **33**, 3704.
Avouris, P., Z. Chen, and V. Perebeinos, 2007, Nature Nanotech. **2**, 605.
Balatsky, A. V., I. Vekhter, and J. X. Zhu, 2006, Rev. Mod. Phys. **78**, 373.
Barlas, Y., T. Pereg-Barnea, M. Polini, R. Asgari, and A. H. MacDonald, 2007, Phys. Rev. Lett. **98**, 236601.
Barlas, Y., and K. Yang, 2009, Phys. Rev. B **80**, 161408.
Barraza-Lopez, S., M. Vanević, M. Kindermann, and M. Y. Chou, 2010, Phys. Rev. Lett. **104**, 076807.
Barzola-Quiquia, J., P. Esquinazi, M. Rothermel, D. Spemann, T. Butz, and N. García, 2007, Phys. Rev. B **76**, 161403.
Baym, G., 1969, *Lectures on Quantum Mechanics* (Addison-Wesley, Reading, Massachusetts).

Baym, G., and C. Pethick, 1991, *Landau Fermi-Liquid Theory* (John Wiley, New York).

Beenakker, C. W. J., 2006, Phys. Rev. Lett. **97**, 067007.

Beenakker, C. W. J., 2008, Rev. Mod. Phys. **80**, 1337.

Bena, C., 2008, Phys. Rev. Lett. **100**, 076601.

Bena, C., and S. Kivelson, 2005, Phys. Rev. B **72**, 125432.

Bercx, M., T. C. Lang, and F. F. Assaad, 2009, Phys. Rev. B **80**, 045412.

Bergman, D., and K. L. Hur, 2009, Phys. Rev. B **79**, 185420.

Bhattacharjee, S., and K. Sengupta, 2006, Phys. Rev. Lett. **97**, 217001.

Biswas, R. R., S. Sachdev, and D. T. Son, 2007, Phys. Rev. B **76**, 205122.

Black-Schaffer, A. M., and S. Doniach, 2007, Phys. Rev. B **75**, 134512.

Black-Schaffer, A. M., and S. Doniach, 2008, Phys. Rev. B **78**, 024504.

Bloch, F., 1929, Z. Phys. **52**, 555.

Bolotin, K. I., F. Ghahari, M. D. Shulman, H. L. Stormer, and P. Kim, 2009, Nature (London) **462**, 196.

Borghi, G., M. Polini, R. Asgari, and A. MacDonald, 2010, Phys. Rev. B **82**, 155403.

Borghi, G., M. Polini, R. Asgari, and A. H. MacDonald, 2009a, Solid State Commun. **149**, 1117.

Borghi, G., M. Polini, R. Asgari, and A. H. MacDonald, 2009b, Phys. Rev. B **80**, 241402.

Borkowski, L. S., and P. J. Hirschfeld, 1992, Phys. Rev. B **46**, 9274.

Bostwick, A., T. Ohta, T. Seyller, K. Horn, and E. Rotenberg, 2006, Nature Phys. **3**, 36.

Bostwick, A., F. Speck, T. Seyller, K. Horn, M. Polini, R. Asgari, A. H. MacDonald, and E. Rotenberg, 2010, Science **328**, 999.

Boukhvalov, D. W., and M. I. Katsnelson, 2009, J. Phys. Chem. C **113**, 14176.

Boukhvalov, D. W., M. I. Katsnelson, and A. I. Lichtenstein, 2008, Phys. Rev. B **77**, 035427.

Brar, V. W., *et al.*, 2010, Phys. Rev. Lett. **104**, 036805.

Brey, L., H. A. Fertig, and S. Das Sarma, 2007, Phys. Rev. Lett. **99**, 116802.

Brown, L. S., R. N. Cahn, and L. D. McLerran, 1975, Phys. Rev. D **12**, 581.

Bunch, J. S., Y. Yaish, M. Brink, K. Bolotin, and P. L. McEuen, 2005, Nano Lett. **5**, 287.

Burset, P., A. L. Yeyati, and A. Martín-Rodero, 2008, Phys. Rev. B **77**, 205425.

Calandra, M., and F. Mauri, 2007, Phys. Rev. B **76**, 205111.

Case, K. M., 1950, Phys. Rev. **80**, 797.

Cassanello, C. R., and E. Fradkin, 1996, Phys. Rev. B **53**, 15079.

Cassanello, C. R., and E. Fradkin, 1997, Phys. Rev. B **56**, 11246.

Castro, E. V., M. P. López-Sancho, and M. A. H. Vozmediano, 2010, Phys. Rev. Lett. **104**, 036802.

Castro, E. V., K. S. Novoselov, S. V. Morozov, N. R. Peres, J. M. B. Lopes dos Santos, J. Nilsson, F. Guinea, A. K. Geim, and A. H. Castro Neto, 2007, Phys. Rev. Lett. **99**, 216802.

Castro, E. V., N. M. R. Peres, J. M. B. Lopes dos Santos, A. H. Castro Neto, and F. Guinea, 2008a, Phys. Rev. Lett. **100**, 026802.

Castro, E. V., N. M. R. Peres, T. Stauber, and N. P. Silva, 2008b, Phys. Rev. Lett. **100**, 186803.

Castro Neto, A. H., 2001, Phys. Rev. Lett. **86**, 4382.

Castro Neto, A. H., and F. Guinea, 2009, Phys. Rev. Lett. **103**, 026804.

Castro Neto, A. H., F. Guinea, and N. M. Peres, 2006, Phys. Rev. B **73**, 205408.

Castro Neto, A. H., F. Guinea, N. M. R. Peres, K. S. Novoselov, and A. K. Geim, 2009a, Rev. Mod. Phys. **81**, 109.

Castro Neto, A. H., V. N. Kotov, J. Nilsson, V. M. Pereira, N. M. R. Peres, and B. Uchoa, 2009b, Solid State Commun. **149**, 1094.

Castro Neto, A. H., J. Nilsson, F. Guinea, and N. M. R. Peres, 2007, Phys. Rev. B **76**, 165416.

Ceni, R., 2001, Nucl. Phys. **A696**, 605.

Ceperley, D., 1978, Phys. Rev. B **18**, 3126.

Chamon, C., C.-Y. Hou, R. Jackiw, C. Mudry, S.-Y. Pi, and A. P. Schnyder, 2008b, Phys. Rev. Lett. **100**, 110405.

Chamon, C., C.-Y. Hou, R. Jackiw, C. Mudry, S.-Y. Pi, and G. Semenoff, 2008a, Phys. Rev. B **77**, 235431.

Chan, K. T., J. B. Neaton, and M. L. Cohen, 2008, Phys. Rev. B **77**, 235430.

Checkelsky, J. G., L. Li, and N. P. Ong, 2008, Phys. Rev. Lett. **100**, 206801.

Checkelsky, J. G., L. Li, and N. P. Ong, 2009, Phys. Rev. B **79**, 115434.

Cheianov, V. V., and V. I. Fal'ko, 2006, Phys. Rev. Lett. **97**, 226801.

Chen, F., J. Xia, D. K. Ferry, and N. Tao, 2009, Nano Lett. **9**, 2571.

Chen, F., J. Xia, and N. Tao, 2009, Nano Lett. **9**, 1621.

Chen, J. H., C. Jang, S. Adam, M. S. Fuhrer, E. D. Williams, and M. Ishigami, 2008, Nature Phys. **4**, 377.

Chen, J.-H., W. G. Cullen, E. D. Williams, and M. S. Fuhrer, 2011, Nature Phys. **7**, 535.

Chen, K., and C. Jayaprakash, 1995, J. Phys. Condens. Matter **7**, L491.

Chen, Y.-F., M.-H. Bae, C. Chialvo, T. Dirks, A. Bezryadin, and N. Mason, 2010, J. Phys. Condens. Matter **22**, 205301.

Coleman, P., 1983, Phys. Rev. B **28**, 5255.

Cooper, L. N., 1956, Phys. Rev. **104**, 1189.

Coqblin, B., and J. R. Schrieffer, 1969, Phys. Rev. **185**, 847.

Cornaglia, P. S., G. Usaj, and C. A. Balseiro, 2009, Phys. Rev. Lett. **102**, 046801.

Csanyi, G., P. B. Littlewood, A. H. Nevidomskyy, and C. P. B. D. Simons, 2005, Nature Phys. **1**, 42.

Cserti, J., A. Csordás, and G. Dávid, 2007, Phys. Rev. Lett. **99**, 066802.

Dahal, H. P., Y. N. Joglekar, K. S. Bedell, and A. V. Balatsky, 2006, Phys. Rev. B **74**, 233405.

Dahal, H. P., T. O. Wehling, K. S. Bedell, J.-X. Zhu, and A. Balatsky, 2010, Physica B (Amsterdam) **405**, 2241.

Das Sarma, S., S. Adam, E. H. Hwang, and E. Rossi, 2011, Rev. Mod. Phys. **83**, 407.

Das Sarma, S., E. H. Hwang, and W.-K. Tse, 2007, Phys. Rev. B **75**, 121406(R).

Dean, C. R., A. F. Young, P. Cadden-Zimansky, L. Wang, H. Ren, K. Watanabe, T. Taniguchi, P. Kim, J. Hone, and K. L. Shepard, 2011, Nature Phys. **7**, 693.

Dean, C. R., A. F. Young, I. Meric, L. W. C. Lee, S. Sorgenfrei, K. Watanabe, T. Taniguchi, P. Kim, K. L. Shepard, and J. Hone, 2010, Nature Nanotech. **5**, 722.

de Juan, F., A. G. Grushin, and M. A. H. Vozmediano, 2010, Phys. Rev. B **82**, 125409.

Dell'Anna, L., 2010 J. Stat. Mech. P01007.

Dillenschneider, R., and J. H. Han, 2008, Phys. Rev. B **78**, 045401.

DiVincenzo, D., and E. Mele, 1984, Phys. Rev. B **29**, 1685.

Dora, B., and P. Thalmeier, 2007, Phys. Rev. B **76**, 115407.

Dresselhaus, M. S., and G. Dresselhaus, 1981, Adv. Phys. **30**, 139.

Drude, P., 1900a, Ann. Phys. (Leipzig) **306**, 566.

Drude, P., 1900b, Ann. Phys. (Leipzig) **308**, 369.

Drut, J. E., and T. A. Lähde, 2009a, Phys. Rev. B **79**, 241405.

Drut, J. E., and T. A. Lähde, 2009b, Phys. Rev. Lett. **102**, 026802.

Drut, J. E., and T. A. Lähde, 2009c, Phys. Rev. B **79**, 165425.

Du, X., I. Skachko, and E. Y. Andrei, 2008, Phys. Rev. B **77**, 184507.

Du, X., I. Skachko, F. Duerr, A. Luican, and E. Y. Andrei, 2009, Nature (London) **462**, 192.
Eberlein, T., U. Bangert, R. R. Nair, R. Jones, M. Grass, A. L. Bleloch, K. S. Novoselov, A. Geim, and P. R. Briddon, 2008, Phys. Rev. B **77**, 233406.
Elias, D. C., *et al.*, 2011, Nature Phys. **7**, 701.
Elias, D. C., *et al.*, 2009, Science **323**, 610.
Enoki, T., and K. Takai, 2009, Solid State Commun. **149**, 1144.
Esquinazi, P., D. Spemann, R. Höhne, A. Setzer, K.-H. Han, and T. Butz, 2003, Phys. Rev. Lett. **91**, 227201.
Feigel'man, M. V., M. A. Skvortov, and K. S. Tikhonov, 2009, JETP Lett. **88**, 747.
Feldman, B. E., J. Martin, and A. Yacoby, 2009, Nature Phys. **5**, 889.
Fermi, E., 1927, Rend. Accad. Naz. Lincei **6**, 602.
Fernández-Rossier, J., 2008, Phys. Rev. B **77**, 075430.
Fernández-Rossier, J., and J. J. Palacios, 2007, Phys. Rev. Lett. **99**, 177204.
Fertig, H. A., and L. Brey, 2006, Phys. Rev. Lett. **97**, 116805.
Fetter, A., 1974, Ann. Phys. (N.Y.) **88**, 1.
Fetter, A. L., and J. D. Walecka, 1971, *Quantum Theory of Many-Particle Systems*, International Series in Pure and Applied Physics (McGraw-Hill, New York).
Fogler, M., D. Novikov, and B. Shklovskii, 2007, Phys. Rev. B **76**, 233402.
Foster, M. S., and I. L. Aleiner, 2008, Phys. Rev. B **77**, 195413.
Foster, M. S., and A. W. W. Ludwig, 2006a, Phys. Rev. B **73**, 155104.
Foster, M. S., and A. W. W. Ludwig, 2006b, Phys. Rev. B **74**, 241102(R).
Fradkin, E., 1986, Phys. Rev. B **33**, 3263.
Fritz, L., J. Schmalian, M. Müller, and S. Sachdev, 2008, Phys. Rev. B **78**, 085416.
Fritz, L., and M. Vojta, 2004, Phys. Rev. B **70**, 214427.
Fuchs, J., and P. Lederer, 2007, Phys. Rev. Lett. **98**, 016803.
Fujita, M., K. Wakabayashi, K. Nakada, and K. Kusakabe, 1996, J. Phys. Soc. Jpn. **65**, 1920.
Furukawa, N., 2001, J. Phys. Soc. Jpn. **70**, 1483.
Gamayun, O. V., E. V. Gorbar, and V. P. Gusynin, 2009, Phys. Rev. B **80**, 165429.
Gamayun, O. V., E. V. Gorbar, and V. P. Gusynin, 2010, Phys. Rev. B **81**, 075429.
Gangadharaiah, S., A. M. Farid, and E. G. Mishchenko, 2008, Phys. Rev. Lett. **100**, 166802.
Geim, A. K., and K. S. Novoselov, 2007, Nature Mater. **6**, 183.
Ghaemi, P., and F. Wilczek, 2012, Phys. Scr. **T146**, 014019.
Ghahari, F., Y. Zhao, P. Cadden-Zimansky, K. Bolotin, and P. Kim, 2011, Phys. Rev. Lett. **106**, 046801.
Ghosal, A., P. Goswami, and S. Chakravarty, 2007, Phys. Rev. B **75**, 115123.
Giesbers, A. J., U. Zeitler, M. I. Katsnelson, L. A. Ponomarenko, T. M. Mohiuddin, and J. C. Maan, 2007, Phys. Rev. Lett. **99**, 206803.
Giesbers, A. J. M., U. Zeitler, L. A. Ponomarenko, R. Yang, K. S. Novoselov, A. K. Geim, and J. C. Maan, 2009, Phys. Rev. B **80**, 241411.
Giovannetti, G., P. A. Khomyakov, G. Brocks, V. M. Karpan, J. van den Brink, and P. J. Kelly, 2008, Phys. Rev. Lett. **101**, 026803.
Girit, C. Ö., J. C. Meyer, R. Erni, M. D. Rossell, C. Kisielowski, L. Yang, C.-H. Park, M. F. Crommie, M. L. Cohen, S. G. Louie, and A. Zettl, 2009, Science **323**, 1705.
Goerbig, M. O., 2011, Rev. Mod. Phys. **83**, 1193.
Goerbig, M. O., R. Moessner, and B. Doucot, 2006, Phys. Rev. B **74**, 161407.
Goerbig, M. O., and N. Regnault, 2007, Phys. Rev. B **75**, 241405.
Goldman, S., and G. Drake, 1982, Phys. Rev. A **25**, 2877.
González, J., 2008, Phys. Rev. B **78**, 205431.
González, J., 2010, Phys. Rev. B **82**, 155404.
González, J., F. Guinea, and M. A. H. Vozmediano, 1994, Nucl. Phys. **B424**, 595.
González, J., F. Guinea, and M. A. H. Vozmediano, 1996, Phys. Rev. Lett. **77**, 3589.
González, J., F. Guinea, and M. A. H. Vozmediano, 1999, Phys. Rev. B **59**, R2474.
González, J., F. Guinea, and M. A. H. Vozmediano, 2001, Phys. Rev. B **63**, 134421.
González-Buxton, C., and K. Ingersent, 1998, Phys. Rev. B **57**, 14254.
Gorbar, E. V., V. P. Gusynin, V. A. Miransky, and I. A. Shovkovy, 2002, Phys. Rev. B **66**, 045108.
Greenbaum, D., S. Das, G. Schwiete, and P. G. Silvestrov, 2007, Phys. Rev. B **75**, 195437.
Greiner, W., B. Müller, J. Rafelski, W. Greiner, B. Muller, and J. Rafelski, 1985, *Quantum Electrodynamics of Strong Fields* (Springer, New York).
Gross, D. J., and A. Neveu, 1974, Phys. Rev. D **10**, 3235.
Grüneis, A., C. Attaccalite, A. Rubio, D. V. Vyalikh, S. L. Molodtsov, J. Fink, R. Follath, W. Eberhardt, B. Büchner, and T. Pichler, 2009, Phys. Rev. B **80**, 075431.
Grüneis, A., and D. V. Vyalikh, 2008, Phys. Rev. B **77**, 193401.
Gruner, G., 1994, *Density Waves in Solids* (Perseus, Cambridge, Massachusetts).
Grushin, A. G., B. Valenzuela, and M. A. H. Vozmediano, 2009, Phys. Rev. B **80**, 155417.
Guettinger, J., C. Stampfer, S. Hellmueller, F. Molitor, T. Ihn, and K. Ensslin, 2008, Appl. Phys. Lett. **93**, 212102.
Guinea, F., 2007, Phys. Rev. B **75**, 235433.
Guinea, F., B. Horowitz, and P. L. Doussal, 2008, Phys. Rev. B **77**, 205421.
Guinea, F., M. I. Katsnelson, and A. K. Geim, 2009, Nature Phys. **6**, 30.
Guinea, F., M. I. Katsnelson, and M. A. H. Vozmediano, 2008, Phys. Rev. B **77**, 075422.
Gupta, K., and S. Sen, 2008, Phys. Rev. B **78**, 205429.
Gupta, K. S., A. Samsarov, and S. Sen, 2010, Eur. Phys. J. B **73**, 389.
Gupta, K. S., and S. Sen, 2009, Mod. Phys. Lett. A **24**, 99.
Gusynin, V. P., V. A. Miransky, S. G. Sharapov, and I. A. Shovkovy, 2006, Phys. Rev. B **74**, 195429.
Gusynin, V. P., V. A. Miransky, S. G. Sharapov, I. A. Shovkovy, and C. M. Wyenberg, 2009, Phys. Rev. B **79**, 115431.
Gusynin, V. P., S. G. Sharapov, and J. P. Carbotte, 2007, Int. J. Mod. Phys. B **21**, 4611.
Güttinger, J., C. Stampfer, F. Libisch, T. Frey, J. Burgdorfer, T. Ihn, and K. Ensslin, 2009, Phys. Rev. Lett. **103**, 046810.
Haldane, F. D. M., 1988, Phys. Rev. Lett. **61**, 2015.
Han, M. Y., J. C. Brant, and P. Kim, 2010, Phys. Rev. Lett. **104**, 056801.
Han, M. Y., B. Özyilmaz, Y. Zhang, and P. Kim, 2007, Phys. Rev. Lett. **98**, 206805.
Hands, S., and C. Strouthos, 2008, Phys. Rev. B **78**, 165423.
Hanisch, T., B. Kleine, A. Ritzl, and E. Müller-Hartmann, 1995, Ann. Phys. (Leipzig) **507**, 303.
Hannay, N. B., T. H. Gaballe, B. T. Matthias, K. Andres, P. Schimidt, and D. MacNair, 1965, Phys. Rev. Lett. **14**, 225.
Harigaya, K., 2001, J. Phys. Condens. Matter Lett. **13**, 1295.
Harigaya, K., and T. Enoki, 2002, Chem. Phys. Lett. **351**, 128.
Hasan, M. Z., and C. L. Kane, 2010, Rev. Mod. Phys. **82**, 3045.
Hawrylak, P., 1987, Phys. Rev. Lett. **59**, 485.

Heersche, H. B., P. J. Herrero, J. B. Oostinga, L. K. Versypen, and A. Morpurgo, 2007, Nature (London) **446**, 56.
Hentschel, M., and F. Guinea, 2007, Phys. Rev. B **76**, 115407.
Herbut, I. F., 2006, Phys. Rev. Lett. **97**, 146401.
Herbut, I. F., 2008, Phys. Rev. B **78**, 205433.
Herbut, I. F., 2010, Phys. Rev. Lett. **104**, 066404.
Herbut, I. F., V. Juricic, and B. Roy, 2009, Phys. Rev. B **79**, 085116.
Herbut, I. F., V. Juricic, and O. Vafek, 2008, Phys. Rev. Lett. **100**, 046403.
Hoddeson, L., G. Baym, and M. Eckert, 1987, Rev. Mod. Phys. **59**, 287.
Honerkamp, C., 2008, Phys. Rev. Lett. **100**, 146404.
Horowitz, B., and P. L. Doussal, 2002, Phys. Rev. B **65**, 125323.
Hou, C.-Y., C. Chamon, and C. Mudry, 2007, Phys. Rev. Lett. **98**, 186809.
Huard, B., N. Stander, J. A. Sulpizio, and D. Goldhaber-Gordon, 2008, Phys. Rev. B **78**, 121402.
Huard, B., J. A. Sulpizio, N. Stander, K. Todd, B. Yang, and D. Goldhaber-Gordon, 2007, Phys. Rev. Lett. **98**, 236803.
Huertas-Herno, D., F. Guinea, and A. Brataas, 2006, Phys. Rev. B **74**, 155426.
Hwang, E. H., and S. Das Sarma, 2007, Phys. Rev. B **75**, 205418.
Hwang, E. H., and S. Das Sarma, 2008a, Phys. Rev. Lett. **101**, 156802.
Hwang, E. H., and S. Das Sarma, 2008b, Phys. Rev. B **77**, 081412.
Hwang, E. H., B. Y.-K. Hu, and S. Das Sarma, 2007, Phys. Rev. Lett. **99**, 226801.
Ingersent, K., and Q. Si, 2002, Phys. Rev. Lett. **89**, 076403.
Jackiw, R., 1984, Phys. Rev. D **29**, 2375.
Jackiw, R., and P. Rossi, 1981, Nucl. Phys. **B190**, 681.
Jacob, D., and G. Kotliar, 2010, Phys. Rev. B **82**, 085423.
Jang, C., S. Adam, J.-H. Chen, E. D. Williams, S. Das Sarma, and M. S. Fuhrer, 2008, Phys. Rev. Lett. **101**, 146805.
Jia, X., M. Hofmann, V. Meunier, B. G. Sumpter, J. Campos-Delgado, J.-M. Romo-Herrera, H. Son, Y.-P. Hsieh, A. Reina, J. Kong, M. Terrones, and M. S. Dresselhaus, 2009, Science **323**, 1701.
Jiang, Y., D.-X. Yao, E. W. Carlson, H.-D. Chen, and J.-P. Hu, 2008, Phys. Rev. B **77**, 235420.
Jiang, Z., Y. Zhang, H. L. Stormer, and P. Kim, 2007, Phys. Rev. Lett. **99**, 106802.
Joly, V. L. J., M. Kiguchi, S.-J. Hao, K. Takai, T. Enoki, R. Sumii, K. Amemiya, H. Muramatsu, T. Hayashi, Y. A. Kim, M. Endo, J. Campos-Delgado, F. López-Urías, A. Botello-Méndez, H. Terrones, M. Terrones, and M. S. Dresselhaus, 2010, Phys. Rev. B **81**, 245428.
Jung, J., and A. H. MacDonald, 2010, Phys. Rev. B **81**, 195408.
Juricic, V., O. Vafek, and I. F. Herbut, 2010, Phys. Rev. B **82**, 235402.
Kane, C., and E. J. Mele, 2005, Phys. Rev. Lett. **95**, 226801.
Kane, C. L., and M. P. A. Fisher, 1992, Phys. Rev. Lett. **68**, 1220.
Kashuba, A. B., 2008, Phys. Rev. B **78**, 085415.
Katsnelson, M., 2006, Phys. Rev. B **74**, 201401(R).
Katsnelson, M. I., and M. F. Prokhorova, 2008, Phys. Rev. B **77**, 205424.
Khalilov, V. R., and C.-L. Ho, 1998, Mod. Phys. Lett. A **13**, 615.
Kharitonov, M. Y., and K. B. Efetov, 2008, Phys. Rev. B **78**, 241401 (R).
Khaymovich, M., N. B. Kopnin, A. S. Melnikov, and I. A. Shereshevskii, 2009, Phys. Rev. B **79**, 224506.
Khveshchenko, D. V., 2001a, Phys. Rev. Lett. **87**, 206401.
Khveshchenko, D. V., 2001b, Phys. Rev. Lett. **87**, 246802.
Khveshchenko, D. V., 2006, Phys. Rev. B **74**, 161402(R).
Khveshchenko, D. V., 2009, J. Phys. Condens. Matter **21**, 075303.
Khveshchenko, D. V., and H. Leal, 2004, Nucl. Phys. **B687**, 323.
Killi, M., T. Wei, I. Affleck, and A. Paramekanti, 2010, Phys. Rev. Lett. **104**, 216406.
Kirwan, D. F., C. G. Rocha, A. T. Costa, and M. S. Ferreira, 2008, Phys. Rev. B **77**, 085432.
Kohn, W., and J. M. Luttinger, 1965, Phys. Rev. Lett. **15**, 524.
Kolezhuk, A., S. Sachdev, R. R. Biswas, and P. Chen, 2006, Phys. Rev. B **74**, 165114.
Kopnin, N. P., and E. B. Sonin, 2008, Phys. Rev. Lett. **100**, 246808.
Kotov, V. N., V. M. Pereira, and B. Uchoa, 2008, Phys. Rev. B **78**, 075433.
Kotov, V. N., B. Uchoa, and A. H. Castro Neto, 2008, Phys. Rev. B **78**, 035119.
Kotov, V. N., B. Uchoa, and A. H. Castro Neto, 2009, Phys. Rev. B **80**, 165424.
Kovtun, P. K., D. T. Son, and A. O. Starinets, 2005, Phys. Rev. Lett. **94**, 111601.
Kramberger, C., R. Hambach, C. Giorgetti, M. H. Rummeli, M. Knupfer, J. Fink, B. Buchner, L. Reining, E. Einarsson, S. Maruyama, F. Sottile, K. Hannewald, V. Olevano, A. G. Marinopoulos, and T. Pichler, 2008, Phys. Rev. Lett. **100**, 196803.
Krasheninnikov, A. V., P. O. Lehtinen, A. S. Foster, P. Pyykko, and R. M. Nieminen, 2009, Phys. Rev. Lett. **102**, 126807.
Kusminskiy, S. V., J. Nilsson, D. K. Campbell, and A. H. Castro Neto, 2008, Phys. Rev. Lett. **100**, 106805.
Kusminskiy, S. V., J. Nilsson, D. K. Campbell, and A. H. Castro Neto, 2009, Europhys. Lett. **85**, 58005.
Laitenberger, P., and R. E. Palmer, 1996, Phys. Rev. Lett. **76**, 1952.
Landau, L. D., and E. M. Lifshitz, 1981, *Quantum Mechanics: Non-Relativistic Theory* (Pergamon Press, New York).
Laughlin, R. B., 1983, Phys. Rev. Lett. **50**, 1395.
Lee, P. A., 1993, Phys. Rev. Lett. **71**, 1887.
Lehtinen, P. O., A. S. Foster, A. Ayuela, A. Krasheninnikov, K. Nordlund, and R. M. Nieminen, 2003, Phys. Rev. Lett. **91**, 017202.
Lemonik, Y., I. L. Aleiner, C. Toke, and V. I. Fal'ko, 2010, Phys. Rev. B **82**, 201408.
Levy, N., S. A. Burke, K. L. Meaker, M. Panlasigui, A. Zettl, F. Guinea, A. H. Castro Neto, and M. F. Crommie, 2010, Science **329**, 544.
Li, G., A. Luican, and E. Y. Andrei, 2009, Phys. Rev. Lett. **102**, 176804.
Li, G., A. Luican, J. M. B. Lopes dos Santos, A. H. Castro Neto, A. Reina, J. Kong, and E. Y. Andrei, 2009, Nature Phys. **6**, 109.
Li, Z. Q., E. A. Henriksen, Z. Jiang, Z. Hao, M. C. Martin, P. Kim, H. L. Stormer, and D. N. Basov, 2008, Nature Phys. **4**, 532.
Li, Z. Q., E. A. Henriksen, Z. Jiang, Z. Hao, M. C. Martin, P. Kim, H. L. Stormer, and D. N. Basov, 2009, Phys. Rev. Lett. **102**, 037403.
Lieb, E. H., 1981, Rev. Mod. Phys. **53**, 603.
Lin, D.-H., 2006, Phys. Rev. A **73**, 044701.
Lin, M. F., and K. W. K. Shung, 1996, Phys. Rev. B **53**, 1109.
Linder, J., A. M. Black-Schaffer, T. Yokoyama, S. Doniach, and A. Sudbø, 2009, Phys. Rev. B **80**, 094522.
Linder, J., T. Yokoyama, D. Huertas-Herno, and A. Sudbø, 2008, Phys. Rev. Lett. **100**, 187004.
Lindhard, J., 1954, Det Kgl Danske Vid. Selskab, Matematisk-fysiske Meddelelser **28**.
Liu, G.-Z., W. Li, and G. Cheng, 2009, Phys. Rev. B **79**, 205429(R).
Liu, Y., R. F. Willis, K. V. Emtsev, and T. Seyller, 2008, Phys. Rev. B **78**, 201403(R).
Loktev, V. M., and V. Turkowski, 2009, Phys. Rev. B **79**, 233402.
Lopes dos Santos, J. M. B., N. M. R. Peres, and A. H. Castro Neto, 2007, Phys. Rev. Lett. **99**, 256802.

Lozovik, Y. E., and A. A. Sokolik, 2010, Phys. Lett. A **374**, 2785.
Ludwig, A. W., M. P. A. Fisher, R. Shankar, and G. Grinstein, 1994, Phys. Rev. B **50**, 7526.
Lundqvist, B., 1967, Zeitschrift fur Physik B Condensed Matter **6**, 193.
Lutchyn, R. M., V. Galitski, G. Refael, and S. Das Sarma, 2008, Phys. Rev. Lett. **101**, 106402.
Lv, M., and S. Wan, 2010, Phys. Rev. B **81**, 195409.
Mahan, G. D., 2000, *Many-Particle Physics* (Plenum, New York).
Maiti, M., and K. Sengupta, 2007, Phys. Rev. B **76**, 054513.
Marino, E. C., and L. H. C. M. Nunes, 2006, Nucl. Phys. **B741**, 404.
Marinopoulus, A. G., L. Reining, A. Rubio, and V. Olevano, 2004, Phys. Rev. B **69**, 245419.
Martelo, L. M., M. Dzierzawa, L. Siffert, and D. Baeriswyl, 1997, Z. Phys. B **103**, 335.
Martin, J., N. Akerman, G. Ulbricht, T. Lohmann, J. H. Smet, K. von Klitzing, and A. Yacoby, 2007, Nature Phys. **4**, 144.
Martinazzo, R., S. Casolo, and G. F. Tantardini, 2010, Phys. Rev. B **81**, 245420.
McCann, E., 2006, Phys. Rev. B **74**, 161403(R).
McCann, E., D. S. L. Abergel, and V. I. Falko, 2007, Solid State Commun. **143**, 110.
McCann, E., and V. I. Fal'ko, 2006, Phys. Rev. Lett. **96**, 086805.
McChesney, J. L., A. Bostwick, T. Ohta, T. Seyller, K. Horn, J. Gonzalez, and E. Rotenberg, 2010, Phys. Rev. Lett. **104**, 136803.
Mele, E. J., 2010, Phys. Rev. B **81**, 161405(R).
Meng, Z. Y., T. C. Lang, S. Wessel, F. F. Assaad, and A. Muramatsu, 2010, Nature (London) **464**, 847.
Miao, F., S. Wijeratne, Y. Zhang, U. C. Coskun, W. Bao, and C. N. Lau, 2007, Science **317**, 1530.
Mil'shtein, A. I., and V. M. Strakhovenko, 1982, Phys. Lett. A **90**, 447.
Min, H., R. Bistritzer, J.-J. Su, and A. H. MacDonald, 2008, Phys. Rev. B **78**, 121401.
Min, H., J. E. Hill, N. A. Sinitsyn, B. R. Sahu, L. Kleinman, and A. H. MacDonald, 2006, Phys. Rev. B **74**, 165310.
Min, H., B. Sahu, S. K. Banerjee, and A. H. MacDonald, 2007, Phys. Rev. B **75**, 155115.
Mishchenko, E. G., 2007, Phys. Rev. Lett. **98**, 216801.
Mishchenko, E. G., 2008, Europhys. Lett. **83**, 17005.
Moghaddam, A. G., and M. Zareyan, 2006, Phys. Rev. B **74**, 241403(R).
Molitor, F., S. Droscher, J. Güttinger, A. Jacobsen, C. Stampfer, T. Ihn, and K. Ensslin, 2009, Appl. Phys. Lett. **94**, 222107.
Molitor, F., A. Jacobsen, C. Stampfer, J. Güttinger, T. Ihn, and K. Ensslin, 2009, Phys. Rev. B **79**, 075426.
Monteverde, M., C. Ojeda-Aristizabal, R. Weil, K. Bennaceur, M. Ferrier, S. Guéron, C. Glattli, H. Bouchiat, J. N. Fuchs, and D. L. Maslov, 2010, Phys. Rev. Lett. **104**, 126801.
Moriyama, S., D. Tsuya, E. Watanabe, S. Uji, M. Shimizu, T. Mori, T. Yamaguchi, and K. Ishibashi, 2009, Nano Lett. **9**, 2891.
Moser, J., and A. Bachtold, 2009, Appl. Phys. Lett. **95**, 173506.
Moser, J., H. Tao, S. Roche, F. Alzina, C. M. Sotomayor Torres, and A. Bachtold, 2010, Phys. Rev. B **81**, 205445.
Mott, N. F., 1949, Proc. Phys. Soc. London Sect. A **62**, 416.
Müller, B., and J. Rafelski, 1975, Phys. Rev. Lett. **34**, 349.
Müller, M., L. Fritz, and S. Sachdev, 2008, Phys. Rev. B **78**, 115406.
Müller, M., J. Schmalian, and L. Fritz, 2009, Phys. Rev. Lett. **103**, 025301.
Nair, R. R., P. Blake, A. N. Grigorenko, K. S. Novoselov, T. J. Booth, T. Stauber, N. M. R. Peres, and A. K. Geim, 2008, Science **320**, 1308.
Nakada, K., M. Fujita, G. Dresselhaus, and M. S. Dresselhaus, 1996, Phys. Rev. B **54**, 17954.
Nakamura, M., E. V. Castro, and B. Dora, 2009, Phys. Rev. Lett. **103**, 266804.
Nandkishore, R., and L. S. Levitov, 2010a, Phys. Rev. Lett. **104**, 156803.
Nandkishore, R., and L. S. Levitov, 2010b, arXiv:1002.1966.
Nandkishore, R., and L. S. Levitov, 2010c, Phys. Rev. B **82**, 115431.
Newns, D. M., and N. Read, 1987, Adv. Phys. **36**, 799.
Ni, Z. H., L. A. Ponomarenko, R. R. Nair, R. Yang, S. Anissimova, I. V. Grigorieva, F. Schedin, P. Blake, Z. X. Shen, E. H. Hill, K. S. Novoselov, and A. K. Geim, 2010, Nano Lett. **10**, 3868.
Niimi, Y., T. Matsui, H. Kambara, K. Tagami, M. Tsukada, and H. Fukuyama, 2005, Appl. Surf. Sci. **241**, 43.
Nilsson, J., A. H. Castro Neto, F. Guinea, and N. M. R. Peres, 2008, Phys. Rev. B **78**, 045405.
Nilsson, J., A. H. Castro Neto, N. M. R. Peres, and F. Guinea, 2006, Phys. Rev. B **73**, 214418.
Nomura, K., and A. MacDonald, 2007, Phys. Rev. Lett. **98**, 076602.
Nomura, K., and A. H. MacDonald, 2006, Phys. Rev. Lett. **96**, 256602.
Nouchi, R., and K. Tanigaki, 2010, Appl. Phys. Lett. **96**, 253503.
Novikov, D., 2007, Phys. Rev. B **76**, 245435.
Novikov, D. S., 2007, Appl. Phys. Lett. **91**, 102102.
Novoselov, K. S., A. K. Geim, S. V. Morozov, D. Jiang, M. I. Katsnelson, I. V. Grigorieva, S. V. Dubonos, and A. A. Firsov, 2005, Nature (London) **438**, 197.
Novoselov, K. S., A. K. Geim, S. V. Morozov, D. Jiang, Y. Zhang, S. V. Dubonos, I. V. Grigorieva, and A. A. Firsov, 2004, Science **306**, 666.
Novoselov, K. S., D. Jiang, F. Schedin, T. J. Booth, V. V. Khotkevich, S. V. Morozov, and A. K. Geim, 2005, Proc. Natl. Acad. Sci. U.S.A. **102**, 10451.
Novoselov, K. S., E. McCann, S. V. Morozov, V. I. Fal'ko, M. I. Katsnelson, U. Zeitler, D. Jiang, F. Schedin, and A. K. Geim, 2006, Nature Phys. **2**, 177.
Nozières, P., 1964, *The Theory of Interacting Fermi Systems* (Benjamin, NewYork).
Ohldag, H., T. Tyliszczak, R. Höhne, D. Spemann, P. Esquinazi, M. Ungureanu, and T. Butz, 2007, Phys. Rev. Lett. **98**, 187204.
Ohta, T., A. Bostwick, T. Seyller, K. Horn, and E. Rotenberg, 2006, Science **313**, 951.
Ojeda-Aristizabal, C., M. Ferrier, S. Guéron, and H. Bouchiat, 2009, Phys. Rev. B **79**, 165436.
Ouyang, M., J.-L. Huang, and C. M. Lieber, 2002, Phys. Rev. Lett. **88**, 066804.
Özyilmaz, B., P. Jarillo-Herrero, D. Efetov, D. A. Abanin, L. S. Levitov, and P. Kim, 2007, Phys. Rev. Lett. **99**, 166804.
Paiva, M., R. T. Scalettar, W. Zheng, R. R. P. Singh, and J. Oitmaa, 2005, Phys. Rev. B **72**, 085123.
Palacios, J. J., J. Fernández-Rossier, and L. Brey, 2008, Phys. Rev. B **77**, 195428.
Park, C.-H., F. Giustino, C. D. Spataru, M. L. Cohen, and S. G. Louie, 2009, Phys. Rev. Lett. **102**, 076803.
Pathak, S., V. B. Shenoy, and G. Baskaran, 2010, Phys. Rev. B **81**, 085431.
Pereira, V. M., A. H. Castro Neto, H. Y. Liang, and L. Mahadevan, 2010, Phys. Rev. Lett. **105**, 156603.
Pereira, V. M., F. Guinea, J. M. B. Lopes dos Santos, N. M. R. Peres, and A. H. Castro Neto, 2006, Phys. Rev. Lett. **96**, 036801.
Pereira, V. M., V. N. Kotov, and A. H. Castro Neto, 2008, Phys. Rev. B **78**, 085101.
Pereira, V. M., J. M. B. Lopes dos Santos, and A. H. Castro Neto, 2008, Phys. Rev. B **77**, 115109.
Pereira, V. M., J. Nilsson, and A. H. Castro Neto, 2007, Phys. Rev. Lett. **99**, 166802.

Perelomov, A. M., and V. S. Popov, 1970, Theor. Math. Phys. **4**, 664.
Peres, N. M. R., 2010, Rev. Mod. Phys. **82**, 2673.
Peres, N. M. R., M. A. N. Araújo, and D. Bozi, 2004, Phys. Rev. B **70**, 195122.
Peres, N. M. R., F. Guinea, and A. H. Castro Neto, 2005, Phys. Rev. B **72**, 174406.
Pisani, L., J. A. Chan, B. Montanari, and N. M. Harrison, 2007, Phys. Rev. B **75**, 064418.
Pisarski, R. D., 1984, Phys. Rev. D **29**, 2423.
Polini, M., R. Asgari, Y. Barlas, T. Pereg-Barnea, and A. H. MacDonald, 2007, Solid State Commun. **143**, 58.
Polini, M., R. Asgari, G. Borghi, Y. Barlas, T. Pereg-Barnea, and A. H. MacDonald, 2008a, Phys. Rev. B **77**, 081411(R).
Polini, M., A. Tomadin, R. Asgari, and A. H. MacDonald, 2008b, Phys. Rev. B **78**, 115426.
Polkovnikov, A., 2002, Phys. Rev. B **65**, 064503.
Polkovnikov, A., M. Vojta, and S. Sachdev, 2001, Phys. Rev. Lett. **86**, 296.
Ponomarenko, L. A., F. Schedin, M. I. Katsnelson, R. Yang, E. W. Hill, K. S. Novoselov, and A. K. Geim, 2008, Science **320**, 356.
Ponomarenko, L. A., R. Yang, T. M. Mohiuddin, S. M. Morozov, A. A. Zhukov, F. Schedin, E. W. Hill, K. S. Novoselov, M. I. Katsnelson, and A. K. Geim, 2009, Phys. Rev. Lett. **102**, 206603.
Popov, V. S., 1971a, Sov. J. Nucl. Phys. **12**, 235.
Popov, V. S., 1971b, Sov. Phys. JETP **32**, 526.
Principi, A., M. Polini, G. Vignale, and M. I. Katsnelson, 2010, Phys. Rev. Lett. **104**, 225503.
Pustilnik, M., and L. I. Glazman, 2001, Phys. Rev. Lett. **87**, 216601.
Qi, X.-L., and S.-C. Zhang, 2011, Rev. Mod. Phys. **83**, 1057.
Raghu, S., X.-L. Qi, C. Honerkamp, and S.-C. Zhang, 2008, Phys. Rev. Lett. **100**, 156401.
Rainis, D., F. Taddei, F. Dolcini, M. Polini, and R. Fazio, 2009, Phys. Rev. B **79**, 115131.
Ramos, M. A., J. Barzola-Quiquia, P. Esquinazi, A. Muñoz-Martin, A. Climent-Font, and M. García-Hernández, 2010, Phys. Rev. B **81**, 214404.
Rappoport, T. G., B. Uchoa, and A. H. Castro Neto, 2009, Phys. Rev. B **80**, 245408.
Read, N., and D. M. Newns, 1983, J. Phys. C **16**, 3273.
Reed, J. P., B. Uchoa, Y. I. Joe, Y. Gan, D. Casa, E. Fradkin, and P. Abbamonte, 2010, Science **330**, 805.
Ritter, K. A., and J. W. Lyding, 2009, Nature Mater. **8**, 235.
Riu, S., and Y. Hatsugai, 2001, Phys. Rev. B **65**, 033301.
Roldán, R., M. P. López-Sancho, and F. Guinea, 2008, Phys. Rev. B **77**, 115410.
Romanovsky, I., C. Yannouleas, and U. Landman, 2009, Phys. Rev. B **79**, 075311.
Roy, B., and I. F. Herbut, 2010, Phys. Rev. B **82**, 035429.
Ryu, S., C. Mudry, C.-Y. Hou, and C. Chamon, 2009, Phys. Rev. B **80**, 205319.
Sabio, J., J. Nilsson, and A. H. Castro Neto, 2008, Phys. Rev. B **78**, 075410.
Sabio, J., F. Sols, and F. Guinea, 2010a, Phys. Rev. B **82**, 121413.
Sabio, J., F. Sols, and F. Guinea, 2010b, Phys. Rev. B **81**, 045428.
Sachdev, S., 1999, *Quantum Phase Transitions* (Cambridge University Press, Cambridge, United Kingdom).
Saha, K., I. Paul, and K. Sengupta, 2010, Phys. Rev. B **81**, 165446.
Sahebsara, P., and D. Sénéchal, 2009, arXiv:0908.0474.
Sahu, B., H. Min, A. H. MacDonald, and S. K. Banerjee, 2008, Phys. Rev. B **78**, 075404.
Saremi, S., 2007, Phys. Rev. B **76**, 184430.
Sasakia, K., J. Jiang, R. Saito, S. Onari, and Y. Tanaka, 2007, J. Phys. Soc. Jpn. **76**, 033702.
Schnez, S., F. Molitor, C. Stampfer, J. Guettinger, I. Shorubalko, T. Ihn, and K. Ensslin, 2009, Appl. Phys. Lett. **94**, 012107.
Schrieffer, J. R., and P. A. Wolff, 1966, Phys. Rev. **149**, 491.
Schwinger, J., 1951, Phys. Rev. **82**, 664.
Semenoff, G. W., 1984, Phys. Rev. Lett. **53**, 2449.
Sengupta, K., and G. Baskaran, 2008, Phys. Rev. B **77**, 045417.
Sensarma, R., E. H. Hwang, and S. D. Sarma, 2010, Phys. Rev. B **82**, 195428.
Sepioni, M., R. R. Nair, S. Rablen, J. Narayanan, F. Tuna, R. Winpenny, A. K. Geim, and I. V. Grigorieva, 2010, Phys. Rev. Lett. **105**, 207205.
Seradjeh, B., 2008, Nucl. Phys. **B805**, 182.
Seradjeh, B., and M. Franz, 2008, Phys. Rev. Lett. **101**, 146401.
Seradjeh, B., H. Weber, and M. Franz, 2008, Phys. Rev. Lett. **101**, 246404.
Sheehy, D. E., and J. Schmalian, 2007, Phys. Rev. Lett. **99**, 226803.
Sheehy, D. E., and J. Schmalian, 2009, Phys. Rev. B **80**, 193411.
Shibata, N., and K. Nomura, 2008, Phys. Rev. B **77**, 235426.
Shimshoni, E., H. A. Fertig, and G. V. Pai, 2009, Phys. Rev. Lett. **102**, 206408.
Shulke, W., U. Bonse, H. Nagasawa, A. Kaprolat, and A. Berthold, 1988, Phys. Rev. B **38**, 2112.
Shung, K. W.-K., 1986a, Phys. Rev. B **34**, 979.
Shung, K. W.-K., 1986b, Phys. Rev. B **34**, 1264.
Shytov, A., M. Katsnelson, and L. Levitov, 2007a, Phys. Rev. Lett. **99**, 246802.
Shytov, A., M. Katsnelson, and L. Levitov, 2007b, Phys. Rev. Lett. **99**, 236801.
Siegel, D. A., C.-H. Park, C. Hwang, J. Deslippe, A. V. Fedorov, S. G. Louie, and A. Lanzara, 2011, Proc. Natl. Acad. Sci. U.S.A. **108**, 11365.
Skrypnyk, Y. V., and V. M. Loktev, 2006, Phys. Rev. B **73**, 241402 (R).
Sols, F., F. Guinea, and A. H. Castro Neto, 2007, Phys. Rev. Lett. **99**, 166803.
Son, D. T., 2007, Phys. Rev. B **75**, 235423.
Son, Y.-W., M. L. Cohen, and S. G. Louie, 2006, Nature (London) **444**, 347.
Sorella, S., and E. Tosatti, 1992, Europhys. Lett. **19**, 699.
Soriano, D., and J. Fernández-Rossier, 2010, Phys. Rev. B **82**, 161302.
Sprinkle, M., D. Siegel, Y. Hu, J. Hicks, A. Tejeda, A. Taleb-Ibrahimi, P. Le Fèvre, F. Bertran, S. Vizzini, H. Enriquez, S. Chiang, P. Soukiassian, C. Berger, W. A. de Heer, A. Lanzara, and E. H. Conrad, 2009, Phys. Rev. Lett. **103**, 226803.
Stampfer, C., J. Güttinger, S. Hellmueller, F. Molitor, K. Ensslin, and T. Ihn, 2009, Phys. Rev. Lett. **102**, 056403.
Stampfer, C., E. Schurtenberger, F. Molitor, J. Güttinger, T. Ihn, and K. Ensslin, 2008, Nano Lett. **8**, 2378.
Stauber, T., F. Guinea, and M. A. H. Vozmediano, 2005, Phys. Rev. B **71**, 041406.
Stein, S. E., and R. L. Brown, 1987, J. Am. Chem. Soc. **109**, 3721.
Taft, E. A., and H. R. Philipp, 1965, Phys. Rev. **138**, A197.
Takei, S., and Y. B. Kim, 2008, Phys. Rev. B **78**, 165401.
Tan, Y. W., Y. Zhang, K. Bolotin, Y. Zhao, S. Adam, E. Hwang, S. Das Sarma, H. Stormer, and P. Kim, 2007, Phys. Rev. Lett. **99**, 246803.
Tediosi, R., N. P. Armitage, E. Giannini, and D. van der Marel, 2007, Phys. Rev. Lett. **99**, 016406.
Terekhov, I. S., A. I. Milstein, V. N. Kotov, and O. P. Sushkov, 2008, Phys. Rev. Lett. **100**, 076803.
Thomas, L. H., 1927, Math. Proc. Cambridge Philos. Soc. **23**, 542.
Tikhonenko, F. V., A. A. Kozikov, A. K. Savchenko, and R. V. Gorbachev, 2009, Phys. Rev. Lett. **103**, 226801.

Tinkham, M., 1996, *Introduction to Superconductivity* (McGraw-Hill, New York).
Titov, M., and C. W. J. Beenakker, 2006, Phys. Rev. B **74**, 041401(R).
Titov, M., A. Ossipov, and C. W. J. Beenakker, 2007, Phys. Rev. B **75**, 0415417.
Todd, K., H.-T. Chou, S. Amasha, and D. Goldhaber-Gordon, 2009, Nano Lett. **9**, 416.
Töke, C., and J. K. Jain, 2007, Phys. Rev. B **75**, 245440.
Töke, C., P. E. Lammert, V. H. Crespi, and J. K. Jain, 2006, Phys. Rev. B **74**, 235417.
Trevisanutto, P. E., C. Giorgetti, L. Reining, M. Ladisa, and V. Olevano, 2008, Phys. Rev. Lett. **101**, 226405.
Tyutyulkov, N., G. Madjarova, F. Dietz, and K. Mullen, 1998, J. Phys. Chem. B **102**, 10183.
Uchoa, B., G. G. Cabrera, and A. H. Castro Neto, 2005, Phys. Rev. B **71**, 184509.
Uchoa, B., and A. H. Castro Neto, 2007, Phys. Rev. Lett. **98**, 146801.
Uchoa, B., and A. H. Castro Neto, 2009, Phys. Rev. Lett. **102**, 109701.
Uchoa, B., V. N. Kotov, N. M. R. Peres, and A. H. Castro Neto, 2008a, Phys. Rev. Lett. **101**, 026805.
Uchoa, B., C.-Y. Lin, and A. H. Castro Neto, 2008, Phys. Rev. B **77**, 035420.
Uchoa, B., T. G. Rappoport, and A. H. Castro Neto, 2011, Phys. Rev. Lett. **106**, 016801.
Uchoa, B., L. Yang, S. W. Tsai, N. M. R. Peres, and A. H. Castro Neto, 2009, Phys. Rev. Lett. **103**, 206804.
Ugeda, M. M., I. Brihuega, F. Guinea, and J. M. Gómez-Rodríguez, 2010, Phys. Rev. Lett. **104**, 096804.
Vafek, O., 2007, Phys. Rev. Lett. **98**, 216401.
Vafek, O., 2010, Phys. Rev. B **82**, 205106.
Vafek, O., and M. J. Case, 2008, Phys. Rev. B **77**, 033410.
Vafek, O., and K. Yang, 2010, Phys. Rev. B **81**, 041401(R).
Valenzuela, B., and M. A. H. Vozmediano, 2008, New J. Phys. **10**, 113009.
Venezuela, P., R. B. Muniz, A. T. Costa, D. M. Edwards, S. R. Power, and M. S. Ferreira, 2009, Phys. Rev. B **80**, 241413(R).
Visscher, P. B., and L. M. Falikov, 1971, Phys. Rev. B **3**, 2541.
Vojta, M., 2001, Phys. Rev. Lett. **87**, 097202.
Vojta, M., and R. Bulla, 2001, Phys. Rev. B **65**, 014511.
Vojta, M., and L. Fritz, 2004, Phys. Rev. B **70**, 094502.
Vojta, M., L. Fritz, and R. Bulla, 2010, Europhys. Lett. **90**, 27006.
Vozmediano, M. A. H., M. P. López-Sancho, T. Stauber, and F. Guinea, 2005, Phys. Rev. B **72**, 155121.
Wallace, P. R., 1947, Phys. Rev. **71**, 622.
Wang, J., H. Fertig, and G. Murthy, 2010, Phys. Rev. Lett. **104**, 186401.
Wang, J., A. Iyengar, H. A. Fertig, and L. Brey, 2008, Phys. Rev. B **78**, 165416.
Wehling, T. O., A. V. Balatsky, M. I. Katsnelson, A. I. Lichtenstein, and A. Rosch, 2010, Phys. Rev. B **81**, 115427.
Wehling, T. O., A. V. Balatsky, M. I. Katsnelson, A. I. Lichtenstein, K. Scharnberg, and R. Wiesendanger, 2007, Phys. Rev. B **75**, 125425.
Wehling, T. O., A. V. Balatsky, A. M. Tsvelik, M. I. Katsnelson, and A. I. Lichtenstein, 2008, Europhys. Lett. **84**, 17003.
Wehling, T. O., H. P. Dahal, A. I. Lichtenstein, M. I. Katsnelson, H. Manoharan, and A. V. Balatsky, 2010, Phys. Rev. B **81**, 085413.
Wehling, T. O., K. S. Novoselov, S. V. Morozov, E. E. Vdovin, M. I. Katsnelson, A. K. Geim, and A. I. Lichtenstein, 2008, Nano Lett. **8**, 173.
Wehling, T. O., S. Yuan, A. I. Lichtenstein, A. K. Geim, and M. I. Katsnelson, 2010, Phys. Rev. Lett. **105**, 056802.
Weisskopf, V. F., 1939, Phys. Rev. **56**, 72.
Weller, T. E., M. Ellerby, S. S. Saxena, R. P. Smith, and N. T. Skipper, 2005, Nature Phys. **1**, 39.
Williams, J. R., L. DiCarlo, and C. M. Marcus, 2007, Science **317**, 638.
Wimmer, M., A. Akhmerov, and F. Guinea, 2010, Phys. Rev. B **82**, 045409.
Withoff, D., and E. Fradkin, 1990, Phys. Rev. Lett. **64**, 1835.
Wojs, A., G. Moller, and N. R. Cooper, 2011, Acta Phys. Pol. A **119**, 592.
Wunsch, B., T. Stauber, and F. Guinea, 2008, Phys. Rev. B **77**, 035316.
Wunsch, B., T. Stauber, F. Sols, and F. Guinea, 2006, New J. Phys. **8**, 318.
Wunsch, B., T. Stauber, F. Sols, and F. Guinea, 2008, Phys. Rev. Lett. **101**, 036803.
Yang, K., S. Das Sarma, and A. H. MacDonald, 2006, Phys. Rev. B **74**, 075423.
Yao, Y., F. Ye, X.-L. Qi, S.-C. Zhang, and Z. Fang, 2007, Phys. Rev. B **75**, 041401(R).
Yazyev, O. V., 2008, Phys. Rev. Lett. **101**, 037203.
Yazyev, O. V., and L. Helm, 2007, Phys. Rev. B **75**, 125408.
Ye, J., and S. Sachdev, 1998, Phys. Rev. Lett. **80**, 5409.
Zeldovich, Y. B., and V. S. Popov, 1972, Sov. Phys. Usp. **14**, 673.
Zhang, F., H. Min, M. Polini, and A. H. MacDonald, 2010, Phys. Rev. B **81**, 041402.
Zhang, G.-M., H. Hu, and L. Yu, 2001, Phys. Rev. Lett. **86**, 704.
Zhang, Y., Z. Jiang, J. P. Small, M. S. Purewal, Y.-W. Tan, M. Fazlollahi, J. D. Chudow, H. L. Stormer, J. A. Jaszczak, and P. Kim, 2006, Phys. Rev. Lett. **96**, 136806.
Zhang, Y., Y.-W. Tan, H. L. Stormer, and P. Kim, 2005, Nature (London) **438**, 201.
Zhang, Y., T.-T. Tang, C. Girit, Z. Hao, M. Martin, A. Zettl, M. F. Crommie, Y. R. Shen, and F. Wang, 2009, Nature (London) **459**, 820.
Zhao, E., and A. Paramekanti, 2006, Phys. Rev. Lett. **97**, 230404.
Zhou, J., Q. Wang, Q. Sun, X. S. Chen, Y. Kawazoe, and P. Jena, 2009, Nano Lett. **9**, 3867.
Zhou, S. Y., G. H. Gweon, A. V. Fedorov, P. N. First, W. A. de Heer, D. H. Lee, F. Guinea, A. H. Castro Neto, and A. Lanzara, 2007, Nature Mater. **6**, 770.
Zhou, S. Y., D. A. Siegel, A. V. Fedorov, and A. Lanzara, 2008, Phys. Rev. B **78**, 193404.
Zhu, J.-X., and C. S. Ting, 2000, Phys. Rev. B **63**, 020506.
Zhu, W., Z. Wang, Q. Shi, K. Y. Szeto, J. Chen, and J. G. Hou, 2009, Phys. Rev. B **79**, 155430.
Zhu, Z.-G., K.-H. Ding, and J. Berakdar, 2010, Europhys. Lett. **90**, 67001.
Zhuang, H.-B., Q.-F. Sun, and X. C. Xie, 2009, Europhys. Lett. **86**, 58004.